Olivia Kettner, Dipl.-Ing., BSc

Doped Sol-Gel-Processed SiC for Hybrid Solar Cells

DOCTORAL THESIS

to achieve the university degree of

Doktorin der technischen Wissenschaften

submitted to

Graz University of Technology

Supervisor

Ao. Univ.-Prof. Mag. Dr.rer.nat. Robert Schennach
Institute of Solid State Physics

Co-Supervisor

Prof. (FH) Dr. rer. nat. Dipl.-Phys. Bettina Friedel
FH Vorarlberg, Forschungszentrum Energie

Graz, February 2019

AFFIDAVIT

I declare that I have authored this thesis independently, that I have not used other than the declared sources/resources, and that I have explicitly indicated all material which has been quoted either literally or by content from the sources used. The text document uploaded to TUGRAZonline is identical to the present doctoral thesis.

Date	Signature

ACKNOWLEDGMENTS

I want to thank my supervisors Bettina Friedel and Robert Schennach for giving me the opportunity to work on SiC and the guidance throughout my PhD. It was a pleasure working with you.

I'm also grateful for the support and help of Elisabeth, who always kindly helped navigate the depths bureaucracy.

Also I want to acknowledge the Austrian Science Fund (FWF) for funding (Project No. P 26968).

Furthermore, I would like to thank the OPV group for the nice working environment and especially Florian Pilat for the support in lab work. Among the collaborators, I would like to thank in particular Thomas Grießer for performing XPS measurements, Roland Resel and Birgit Kunert for performing and discussing the XRD measurements and Peter Zach for the photoluminescence measurements.

Moreover, I would like to thank Lissi for a lot of discussions about physics related and non-physics related topics in our coffee breaks.

I want to express my greatest gratitude to my family, especially my parents, and friends who accompanied and supported me all along my whole studies. Last, I would like to thank Tim for motivating me and believing in me.

ABSTRACT

Silicon carbide (SiC) is an inorganic wide band gap semiconductor (2.4 eV) with unique properties like thermal stability and low toxicity, which makes it attractive not only for high power electronics but also for the use in solar cell devices. While SiC would usually not be considered for application in conventional photovoltaics as it merely absorbs in the UV-range, it is an interesting candidate as acceptor in hybrid photovoltaics due to its high electron affinity and electron mobility. The present thesis deals with the fabrication of the cubic polytype of SiC with different dopants via a wet chemical synthesis route as well as its use as co-acceptor in organic-inorganic hybrid solar cells. These hybrid solar cells have been in the focus of extensive research for the last decade as they combine the benefits of both classes of materials. Organic materials offer a solution based and easy fabrication route, are light in weight and comparably cheap in production, where inorganics have higher charge carrier mobilities and can contribute to light harvesting in the visible wavelength range.

Two different p-dopants (Al and Ga) and one n-dopant (N) were incorporated into the crystal lattice during the synthesis of nano or micro crystalline 3C-SiC. For the Ga-doped material, the defect density was evaluated via electron paramagnetic resonance measurements. The fabricated material was characterized morphologically with optical and scanning electron microscopy to investigate shape and size distribution and via X-ray diffraction to investigate the composition of the powder samples. The surface termination was determined via X-ray photoelectron spectroscopy and bulk properties were investigated via reflection absorption infrared spectroscopy. These investigations revealed that not only the polytype composition of the powder samples, but also the composition of the surface depends on the doping species. It is demonstrated that with increasing atomic number of the dopant the hexagonality of the samples increases and also the grain size.

The SiC crystallites were incorporated as co-acceptor material in an organic semiconductor matrix of P3HT and $PC_{60}BM$ as this is one of the most well researched material combinations used for organic bulk-heterojunction solar cells. In this thesis, the use of doped SiC micro- and nano-crystallites as co-acceptor material is demonstrated for the first time. Detailed investigation of the electrical and photophysical properties of hybrid solar cell using SiC doped with nitrogen impurities were performed, revealing SiC is not a proper candidate for replacing the organic $PC_{60}BM$ as acceptor material. It was demonstrated that a suitable ratio between the organic and inorganic co-acceptor material leads to the improvement of the

power conversion efficiency of ternary component hybrid solar cells reaching 2.2% in comparison to binary organic solar cells exhibiting 1.6% efficiency.

A comparative study on hybrid solar cells fabricated with high and low fractions of SiC:Al, SiC:Ga or SiC:N as co-acceptor is presented. The solar cell key parameters as well as the photophysics were investigated to learn how the different impurity atoms and the different co-acceptor weight fractions impact on the device performance. These investigations revealed the best performance for low fractions of SiC:Al as co-acceptor. It is shown that a crucial point for the device performance is the size control of the SiC crystallites as well as the amount incorporated in organic thin films.

Overall the experimental results confirm that doped SiC in the cubic manifestation is highly beneficial for the use as co-acceptor in P3HT:$PC_{60}BM$ solar cells. The incorporation of size-controlled SiC crystallites in a suitable fraction leads to a remarkable increase of the solar cell performance.

KURZFASSUNG

Siliziumkarbid (SiC) ist ein anorganischer Halbleiter mit breiter Bandlücke (2,4 eV), der einzigartige Eigenschaften wie hohe thermische Stabilität und geringe Toxizität aufweist. Dies macht das Material nicht nur für die Hochleistungselektronik, sondern auch für den Einsatz in Solarzellen interessant. Während SiC normalerweise nicht für die Anwendung in konventionellen Solarzellen in Betracht gezogen wird da es hauptsächlich im UV-Bereich absorbiert, ist es aufgrund seiner hohen Elektronenaffinität und Elektronenbeweglichkeit ein interessanter Kandidat als Akzeptor in der Hybrid-Photovoltaik.

Die vorliegende Arbeit beschäftigt sich mit der Herstellung des kubischen Polytyps von SiC mit verschiedenen Dotierstoffen über einen nasschemischen Syntheseweg sowie seiner Verwendung als Co-Akzeptor in organischen anorganischen Hybridsolarzellen.

Hybridsolarzellen sind im letzten Jahrzehnt Gegenstand intensiver Forschung, da sie die Vorteile beider Klassen von Materialien vereinen. Organische Materialien bieten einen lösungsmittelbasierten und einfachen Herstellungsprozess, sind leicht und vergleichsweise billig in der Produktion. Anorganische Materialien weisen eine höhere Ladungsträgerbeweglichkeit auf und können zur Absorption von Licht im sichtbaren Wellenlängenbereich beitragen.

Während der Synthese von nano- oder mikrokristallinem 3C-SiC wurden zwei verschiedene p-Dotierstoffe (Al und Ga) und ein n-Dotierstoff (N) in das Kristallgitter eingebaut. Für das Ga-dotierte SiC wurde die Defektdichte durch elektronen-paramagnetische Resonanz Messungen ermittelt. Das hergestellte Material wurde morphologisch charakterisiert. Mit Hilfe von optischer und Rasterelektronenmikroskopie wurden Form- und Größenverteilung der Partikel untersucht und Röntgenbeugung wurde verwendet, um die Zusammensetzung der Pulverproben zu ermitteln. Die Oberflächenterminierung wurde mittels Röntgen-Photoelektronen Spektroskopie bestimmt, und die Volumeneigenschaften wurden mittels Reflexionsabsorptions-Infrarotspektroskopie untersucht.

Diese Untersuchungen zeigten, dass nicht nur die Polytypzusammensetzung der Pulverproben, sondern auch die Zusammensetzung der Oberfläche von der Dotierungsart abhängt. Es wird gezeigt, dass mit zunehmender Ordnungszahl des Dotierstoffs sowohl die Hexagonalität als auch die Korngröße der Proben zunimmt.

Die SiC-Kristallite wurden als Co-Akzeptor in eine organische Halbleitermatrix aus P3HT und $PC_{60}BM$-Matrix eingebaut, da dies eine der am besten erforschten Materialkombinationen für organische Bulk-Heteroübergangs-Solarzellen ist. Im Rahmen

dieser Arbeit wird erstmals der Einsatz von dotierten SiC Mikro- und Nanokristalliten als Co-Akzeptor Material gezeigt. Detaillierte Untersuchungen der elektrischen und photophysikalischen Eigenschaften von Hybridsolarzellen unter Verwendung von Stickstoff dotiertem SiC wurden durchgeführt, wobei sich herausstellte, dass SiC:N kein geeigneter Kandidat für den Ersatz des organischen $PC_{60}BM$ als Akzeptormaterial ist. Es wurde gezeigt, dass ein geeignetes Verhältnis zwischen dem organischen und dem anorganischen Co-Akzeptor zur Verbesserung der Leistungsumwandlungseffizienz von ternären Hybrid-Solarzellen auf bis zu 2,2% führt, im Vergleich zu binären organischen Solarzellen mit nur 1,6%.

Eine Vergleichsstudie mit Hybridsolarzellen wird vorgestellt. Hier wurden Hybridsolarzellen mit hohen und niedrigen Anteilen an SiC:Al, SiC:Ga oder SiC:N als Co-Akzeptor hergestellt. Die Schlüsselparameter der Solarzelle sowie die Photophysik wurden untersucht, um herauszufinden wie sich die verschiedenen Fremdatome sowie die unterschiedlichen Gewichtsanteile der Co-Akzeptoren auf die Leistung des Bauelements auswirken. Diese Untersuchungen zeigten die beste Leistung für kleine Konzentrationen von SiC:Al als Co-Akzeptor. Dabei ist ein entscheidender Punkt für die Effizienz dieser Solarzellen die verwendete Menge an SiC, die in die organischen Dünnschichten eingebaut wird.

Die experimentellen Ergebnisse bestätigen, dass dotiertes, kubisches SiC für die Verwendung als Co-Akzeptor in $P3HT:PC_{60}BM$-Solarzellen sehr vorteilhaft ist. Das Einbringen einer geeigneten Menge von größenselektierten SiC-Kristalliten führt zu einer bemerkenswerten Steigerung der Effizienz der Solarzellen.

CONTENTS

1 INTRODUCTION 1

1.1 Silicon Carbide 2

1.1.1 A Brief History 2

1.1.2 Crystal Structure 3

1.1.3 Physical and Chemical Properties 5

1.1.4 Fabrication Techniques 6

1.1.5 Doping 8

1.2 Sol-Gel Processing 10

1.2.1 History and Basic Principles 10

1.2.2 Sol-Gel Fabrication of Carbides 15

1.2.3 Sol-Gel Fabrication of SiC 16

1.3 Photovoltaics 16

1.3.1 Solar Energy 16

1.3.2 Organic and Hybrid Solar Cells 18

1.3.2.1 Active Layer Materials 18

1.3.2.2 Device Architecture 22

1.3.2.3 Hybrid Bulk-Heterojunction Devices 24

1.3.2.4 Working Principles 24

1.4 Objectives and Structure of the Thesis 27

2 EXPERIMENTAL AND CHARACTERIZATION 29

2.1 SiC Synthesis and Device Fabrication 30

2.1.1 Sol-Gel Fabrication of SiC Powders 30

2.1.2 Solar Cell Device Fabrication 31

2.2 Analytical Methods 33

2.2.1 Optical Microscopy 33

2.2.2 Scanning Electron Microscopy (SEM) 34

2.2.3 Transmission Electron Microscopy (TEM) and Electron Energy Loss Spectroscopy (EELS) 36

2.2.4 Electron Paramagnetic Resonance (EPR) 38

2.2.5 X-Ray Diffraction (XRD) and Rietveld Refinement 40

2.2.6 X-Ray Photoelectron Spectroscopy (XPS) 42

2.2.7 Reflection Absorption Infrared Spectroscopy (RAIRS) 43
2.2.8 Current-Voltage Characterization 44
2.2.9 Spectral Response 46
2.2.10 Transient Photocurrent Measurements.. 47
2.2.11 Light-Beam induced Current (LBIC) Measurements 48
2.2.12 UV-vis Spectroscopy 49
2.2.13 Photoluminescence (PL) and Quantum Yield (QY) Measurements 51
3 RESULTS AND PUBLICATIONS 53
3.1 Characterization of Surface and Structure of In Situ Doped Sol-Gel-Derived Silicon Carbide 54
3.2 Incorporation of Nitrogen-Doped SiC Nanocrystals in Organic Solar Cells 67
3.2.1 Introduction 67
3.2.2 Incorporation of SiC Nano-Crystals in P3HT:PC_{60}BM Blends 68
3.2.3 Integral Device Behaviour 71
3.2.4 Photophysics and Photoresponse 76
3.2.5 Spatially-Resolved Device Characteristics 81
3.2.6 Transient Photocurrent 83
3.2.7 Conclusions 85
3.3 Gallium Doping of 3C-SiC and Application in Hybrid Solar Cells 87
3.3.1 Introduction 87
3.3.2 Characterisation of Ga-doped 3C-SiC 89
3.3.2.1 EPR Investigation of Gallium Impurities in 3C-SiC 89
3.3.2.2 Analysis of the Structure and Surface Composition of Ga-doped SiC Micro-crystals 91
3.3.2.3 Discussion of Ga-doped SiC Powder Samples 103
3.3.3 Hybrid Solar Cells Fabricated with Al-, Ga- and N-doped SiC as Co-Acceptor 104
3.3.3.1 Characteristics of Solar Cell Devices 104
3.3.3.2 Photophysics and Photoresponse 111
3.3.4 Conclusions 116
4 GENERAL CONCLUSION AND OUTLOOK 119
4.1 General Conclusions 120

4.2 Outlook 123
5 ANNEX 125
5.1 List of Abbreviations and Acronyms 126
5.2 List of Tables 128
5.3 List of Figures 128
6 REFERENCES 133

1 INTRODUCTION

1.1 Silicon Carbide

1.1.1 A Brief History

The first synthesis of silicon carbide (SiC) was carried out by the Swedish chemist J. J. Berzelius, who is mostly known for the discovery of the element Silicon (Si). In 1824 he published a paper where he suspected the formation of bonds between Si and Carbon (C) atoms.[1,2]

In the second half of the 19th century E. G. Acheson was searching for a method to synthesize diamond. Among several different precursor materials, he heated silica and coke in a furnace and successfully fabricated a hard-crystalline material. Much later, the *carborundum*, as he called it, was properly identified as SiC. The fabrication process he commercially established is known today as Acheson process and has been developed further.[3] SiC only rarely appears in nature, with its highest abundance in extra-terrestrial objects, like meteorites. This natural form of SiC, is called moissanite as it was first found by Moissan in 1905.[2] These objects only contain the polytypes 3C and 2H (see subsection 1.1.2.). Certain isotopic compositions in SiC grains found on meteorites suggest that this material can also be formed in supernovae.[4]

H. J. Round was the first to notice the light-emitting properties of this compound in 1907, when applying voltages between 10 V and 110 V to a SiC crystallite and detecting several different emission colours including yellow, orange and blue.[5]

The interest in using it as a semiconducting material started around 1955, when a method for the fabrication of SiC crystals based on sublimation from the vapour phase was invented by Lely. This process allowed, to some extent, the control of properties and purity of the fabricated material.[6]

At this point it was still not possible to grow high purity wafers. In the end of the 1970s, Tairov and Tsvetkov invented a process, which is known as the modified Lely method. It allows to grow wafers under controlled conditions in a reproducible way from seeded sublimation by forcing material transport to a seed crystal via a temperature gradient.[7]

Another important step in the evolution of SiC technology was taken in 1987, when the high-quality growth of epitaxial layers at relatively low temperatures became possible.[8]

Till now this material is topic of various research fields, including the optimization of growth and doping processes, but also more exotic fields like the potential for drug transport in the human body.[9] It is still used as abrasive material as suggested by Acheson, but also became a suitable candidate for high power, high temperature and high frequency applications, due to the achievements in growth and quality control.[10,11]

1.1.2 Crystal Structure

Polytypism means the existence of a compound in more than one stacking sequence of a layer-like arranged atomic configuration. While their unit cells differ in lattice system, dimensions or atom number or both, the chemical composition stays the same. Structurally, polytypism is a special case of polymorphism, but their physical properties differ from one another. A material undergoes a first order phase transition when changing the polymorph, but a second order phase transition when changing the polytype.[11] SiC is a very interesting representative for polytypism, as it exists in a few tens of referenced polytypes even though reports claim the existence of more than 200 different polytypes.[12,13] The lattice parameters and information about crystal structures of three different hexagonal and the only cubic constitution of SiC are summarized in table 1.1.[14,15]

Table 1.1.: Summary of the properties of the SiC polytypes 2H, 4H, 6H and 3C.

	2H	**4H**	**6H**	**3C**
Lattice constants (Å)	a = 3.076 c = 5.048	a = 3.0817 c = 10.0791	a = 3.0817 c = 15.1173	a = 4.3579
Stacking sequence	AB	ABCB	ABCACB	ABC
Point group	C_{6v}^4	C_{6v}^4	C_{6v}^4	T_d^2
Space group	$P6_3mc$	$P6_3mc$	$P6_3mc$	F-43m
Atoms per unit cell	4	8	12	2
Hexagonality (%)	100	50	33.3	0

Si and C atoms are covalently bonded to each other with a bond length of 1.89 Å, where every Si atom has four C neighbours and vice versa. This leads to the formation of tetrahedrons and subsequently to the creation of Si-C double atomic layers, which exist in

three different configurations, namely A, B and C. The different polytypes differ from each other in the stacking sequence of the three configurations. The Ramsdell notation of the polytypes gives information about their constitution. The polytype 2H has a stacking sequence of AB, indicated by the number “2” and the letter H denotes a hexagonal crystal structure. 3C-SiC consists of the three stacking units A, B and C, which are repeated periodically and is the only polytype exhibiting a fully cubic lattice structure. 2H exhibits a wurtzite structure, which generally appears in crystals with a high ionicity like Gallium nitride (GaN). The modification 3C grows in a zincblende structure that appears in most III - V semiconductors. As denoted in table 1.1., 4H and 6H SiC belong to the hexagonal polytypes with a mixture of cubic and hexagonal structure consisting of four and six repetition units, respectively. Also, other types of SiC, like for instance in a rhombohedral configuration (indicated by the letter R in the Ramsdell notation) exist. Rhombohedral and hexagonal polytypes are also referred to as α-SiC. When 6H- and 3C-SiC are the only representatives, they are often called α-SiC and β-SiC, to refer to their high- or low-temperature form, respectively.[15–17] The unit cells and according stacking sequences of the polytypes 2H, 3C, 4H and 6H are shown in figure 1.1., where the red dots indicate Si atoms and the blue dots C atoms, respectively.

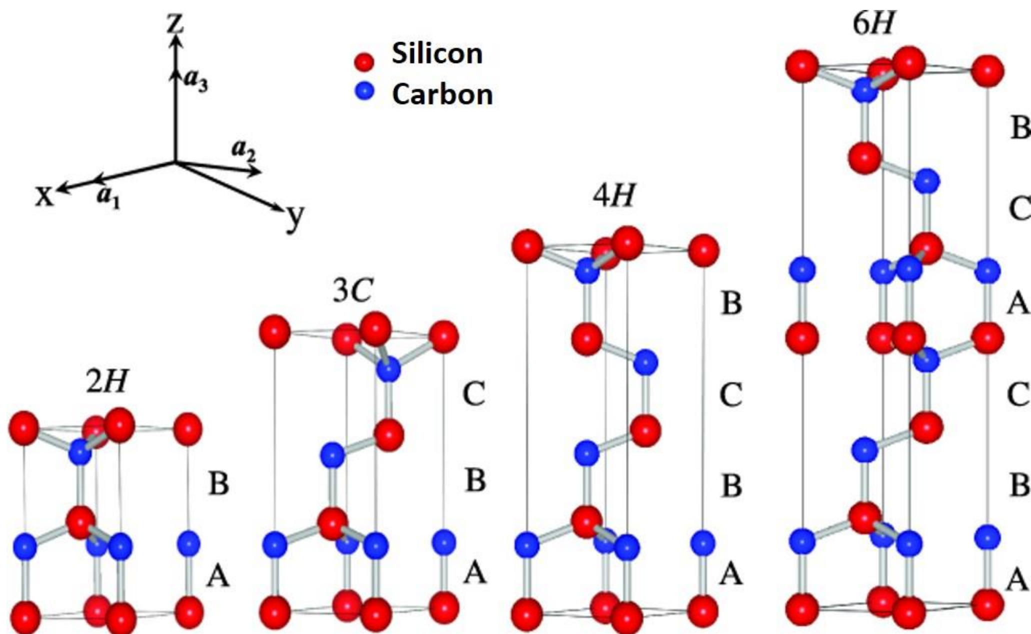

Figure 1.1.: Illustration of the unit cells and stacking sequences of the three most common polytypes of SiC.[18]

The polytypes 4H, 6H and 15 R tend to form hexagonal platelets, so called Lely platelets, which can also consist of mixed polytypes.[19] Unlike the above mentioned polytypes, the cubic configuration exhibits crystallites in the shape of truncated tetrahedrons.[20] Examples for both habits are shown in figure 1.2., where a Lely platelet is illustrated on the left and a truncated tetrahedron on the right. These habits can differ in visual appearance as different crystal faces can be exposed.

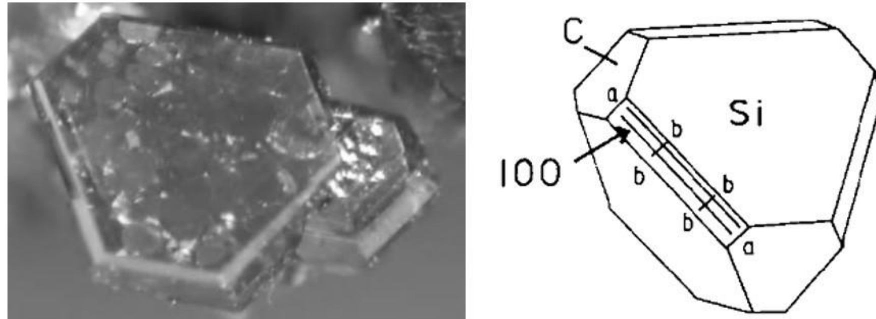

Figure 1.2.: Illustration of a Lely platelet (left) and a schematically depicted truncated tetrahedron (right).[19,20]

1.1.3 Physical and Chemical Properties

The difference in the polytype crystal structure, which results from different stacking, also reflects in their physical and chemical properties. A summary of the major physical and chemical properties of three common polytypes is shown in table 1.2.

SiC single crystals belong to the hardest existing materials, according to the Mohs scale. With a value of 9 – 9.5 they are just below diamond, which makes them not only attractive as abrasive and for cutting and grinding, but also for the use in applications where high mechanical strength is desired.[21,22] The high sublimation temperatures of 2200 – 2830 °C originate from the strong chemical bonds between the Si and C atoms.[16,19]

The high chemical stability and also mechanical integrity allow the use of this material in harsh environments, for examples catalyst support coatings for diesel particulate filters and in sensors, which are exposed to extreme pH values.[23,24]

Each polytype exhibits a different electronic band structure, with increasing complexity for more elaborate crystal structures. This leads to different optical and electronical properties.

SiC is an indirect wide band gap semiconductor. The size of the band gap increases with increasing hexagonality of the crystal structure, as can be seen in table 1.2. The gap energy is temperature-dependent and therefore the literature values slightly vary from each other.[15] The charge mobilities shown are valid for low doping concentrations at room temperature. The mobilities can be changed via p- and n-doping.[16]

Table 1.2.: Summary of the most important physical and chemical properties of the SiC polytypes 4H, 6H and 3C.

	4H	**6H**	**3C**
Mohs hardness	9 – 9.5		
Density (g / cm^3)	3.21		
Sublimation temperature	2200 – 2830 °C		
Bandgap (eV)	3.27	3.02	2.39
Electron mobility perpendicular to the z-axis (cm^2 V^{-1} s^{-1})	1020	450	1000
Electron mobility parallel to the z-axis (cm^2 V^{-1} s^{-1})	1200	100	1000
Hole mobility (cm^2 V^{-1} s^{-1})	120	100	100
Relative dielectric constant perpendicular to the z-axis	9.76	9.66	9.72
Relative dielectric constant parallel to the z-axis	10.32	10.03	9.72

1.1.4 Fabrication Techniques

The choice of a growth process depends highly on the requirements of the final product, like purity and polytype.

For technical SiC, used as abrasive or ceramic material, the fabrication is still based on the Acheson process as purity and polytype are of little importance and millions of tons are needed. This fabrication route uses quartz sand (Si source) and petroleum coke (C source) as raw materials, which are heated up to 1700 - 2500 °C in an electrical resistance furnace, also called Acheson furnace, and undergo a carbothermal reduction reaction. There α-SiC, β-SiC, metallurgic grade and also unreacted materials are the outcome. During growth with the Acheson process it is also likely that stacking faults appear, which make it unfavourable for applications where a distinct order in the crystal structure is needed.[25,26]

For SiC of semiconducting grade, there are various fabrication processes, the most important ones will be discussed briefly.

The nucleation probability and also the stability of the different polytypes is strongly temperature-dependent. The high temperature stable polytypes 4H and 6H are relatively easy to grow in boules. Wafer production of 3C SiC is very difficult as monocrystalline bulk structures can be hardly fabricated at reasonable growth rates, because they transform to the hexagonal polytypes for temperatures above 1900 – 2000 °C. What makes this polytype still popular is the possibility of heteroepitaxial growth on a Si wafer.[16] At the moment, the preferred method for wafer production is growth by seeded sublimation (i.e. physical vapor transport) which is a modification of the Lely method. Advantages of this growth technique are the high growth rate, process stability and reasonable cost. For this growth process, carried out in inert Ar or He atmosphere, a temperature gradient between a SiC seed and a SiC source is applied, where the seed is located at the cooler end of the graphite crucible which helps to avoid nucleation on the inner walls of the crucible. The temperature gradient (typically few tens of °C/cm) can be controlled, allowing to control sublimation and condensation. This process includes 3 basic steps: the sublimation of the SiC source, the mass transport of the sublimed species to the seed and finally the surface reaction and crystallization. The polytypes grown by this method are 4H and 6H, as temperatures are too high for the stable formation of 3C. The purity of the material is strongly dependent on the SiC source and the graphite parts.[16,27,28]

Chemical vapor deposition (CVD) is another growth technique for the growth of long ingots as well as epitaxial layers. This method utilizes reactive precursor gases, which are for example SiH_4 as Si source and hydrocarbons diluted in a carrier gas (e.g. H_2) as C source for boule growth. The process is carried out in a vertical graphite crucible at temperatures between 2100 and 2300 °C. The advantage of this growth technique is the easy control of

the C/Si ratio and doping. What makes the CVD technique especially interesting, is the possibility to grow 3C-SiC wafers on Si templates at 1350 °C by using dichlorosilane (SiH_2Cl_2) and acetylene (C_2H_2) as precursor gases. Unfortunately, this heteroepitaxial growth technique still needs to be improved, as the defect density needs to be reduced for use in high performance devices.[16,29,30]

The top seeded solution growth method facilitates the growth of SiC from an incongruent melt of Si and C. Solution-based growth at high temperatures has, compared to other methods, the advantage that the grown material generally has a lower dislocation density. The process is carried out in a high density graphite crucible, which at the same time acts as container for the Si-melt and provides the C which gets dissolved. The solute which is formed in the crucible is transferred to the growth area and crystalizes at a seed crystal. A disadvantage of this technique is the fairly low solubility of C in pure Si at reasonable temperatures (~0.1% at 1727 °C), leading to low growth rates. The improvement of the solubility of C can be achieved by adding metals like Cr to the Si-melt.[31–33]

Another fabrication route, which is especially interesting for high quality nano-/microcrystalline or porous SiC, is carbothermal reduction of carbon-rich silica glass. The source material, which is also called silicon oxycarbide (SiOC)[34], is often derived by sol-gel processing, a method described in general terms in section 1.2. and in more detail, as used in the scope of this thesis, in section 2.1.1.

1.1.5 Doping

The incorporation of dopants in semiconductors is used to adjust their semiconducting properties by generating energy levels close to the valence and conduction band edge. SiC is a compound semiconductor, containing two group-IV elements. For n-type doping group-V elements, like nitrogen (N) or phosphorus (P) are incorporated into the crystal lattice, generating energy states close to the conduction band. p-doping is achieved by incorporation of group-III elements like boron (B), aluminium (Al) or gallium (Ga), where energy levels close to the valence band are generated. The impurity atoms can reside either on the Si or the C sublattice. Which site gets substituted does not depend on the polytype, but on which configuration leads to the lowest free energy of the system. N and P get substituted on the C site, Al and Ga on the Si site and B on either of them. Nitrogen is regarded as inevitable natural dopant even for material grown under high purity conditions.[35] A schematic

illustration of the energy levels resulting from commonly used dopants for the polytypes 3C, 4H and 6H is depicted in figure 1.3.[36–40]

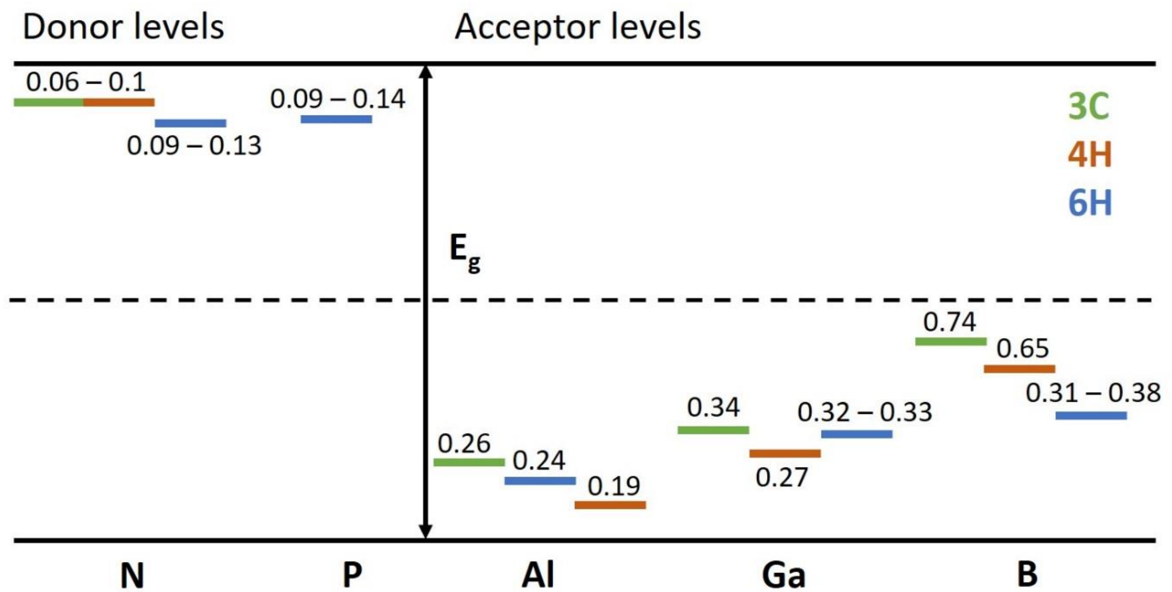

Figure 1.3.: Energy level diagram of commonly used dopants in SiC-polytypes 3C (green), 4H (red) and 6H (blue).

One method to achieve doping in SiC, is to perform it while crystal growth by adding the doping species to the precursor materials. This is possible for n- and p-type dopants and can be performed during growth by sublimation, epitaxy and even carbothermal reduction, but is not suitable for selected area doping. Doping by molecular diffusion is commonly used for semiconducting materials like Si, but is almost impossible in SiC because of the extremely low diffusion in this material. For achieving reasonable diffusion coefficients, temperatures above 2000 °C would be necessary. This problem can be overcome by ion implantation, where the target crystal is bombarded with high energy ions of the desired dopant. This method allows reproducible doping concentrations and profiles and makes it attractive for electronic devices. A disadvantage of this process is that it causes lattice damage. Therefore, a subsequent annealing step at high temperatures (1500 – 1600 °C) is necessary to reduce the damage and also electrically activate the implanted species. The method is suitable for n-type doping with N and P and p-doping with Al. B is rarely implanted, as it causes several undesired phenomena like out-diffusion during annealing.[16,41]

1.2 Sol-Gel Processing

Sol-gel processing is a unique wet-chemical method to prepare oxides, glasses and high temperature ceramics from a liquid at fairly low temperatures. What makes it often the method of choice, is the fact that different physical forms, like nanostructures, fibres and thin films can be prepared by using the same precursor materials and simply changing some experimental conditions.

1.2.1 History and Basic Principles

First reports utilizing this process for the fabrication of silica sol and subsequent formation of a glass like material in the mid-1800s were made by Ebelmen[42] and Graham[43]. This attracted only little technological interest, as drying times of one year or longer were required. In the 1930s sol-gel processes gained interest again when Geffcken and Berger started using metal alkoxide precursors for the deposition of oxide layers on glasses.[44] Around the same time mineralogists became interested in the fabrication of homogenous powders and later Roy developed a method for the preparation of more homogenous melts and glasses based on a sol-gel process for different novel ceramic oxide compositions.[45] In the 1960s, optics became an application, when H. Schroeder investigated the change of the refractive index by the deposition of transparent layers on glasses.[46] With the development of new precursor materials and practical achievements, like the fabrication of fibres, coatings and monolithic products, this technique moved further in to the centre of scientific interest.[47,48] Around the early 1970s the interest also increased for industrial applications, as the fabrication of multicomponent glasses via controlled hydrolysis and condensation became possible.[49] The topic remains a popular research field with the steady development of new materials used for precursors, enabling the use in a wide range of applications, like space science or drug transport in the human body.

Compared to other methods used for this purpose, this technique offers numerous advantages, like the flexibility according to stoichiometry and doping, but also the yielding of high surface area materials required for certain applications like photoelectrochemical processes (e.g. dye-sensitized solar cells or solar fuel). Sol-gel processing is also economic, as no expensive equipment is required, and the starting materials are easy and cheap to obtain in high purity.

In brief, the process typically starts with a solution of a metal-organic precursor. By reaction of the monomer with water, fully or partially hydrolysed intermediate species form. These molecules then polymerize by forming bridging M-O-M bonds to each other, leading to the formation of a network and finally a stable gel.

To have a closer look at the process, it is necessary to consider the reactants and the basic steps:

- Hydrolysis and condensation
- Gelation
- Aging
- Drying
- Sintering

As metal-organic precursors, metal alkoxides are commonly the material of choice. They consist of one or more metal or half-metal atoms in the centre, which is/are surrounded by non-metallic, organic ligands. In metal alkoxides, the ligands are alkoxy groups (OR). Metal alkoxides are generally very reactive because of the electronegative OR-groups, which help to make the metal highly susceptible to nucleophilic attack.

In the first step, the metal alkoxides are dissolved in an organic solvent (usually alcohol), which is miscible with water. The details about the single process steps and the corresponding chemical reactions will be shown below on the example of silicon alkoxides.

Hydrolysis and condensation: The initiation of polymerisation by water is called hydrolysis. At this step a sol of dispersed metal hydroxide is formed due to the replacement of the alkoxide groups by hydroxyl groups (OH). The alkoxide group forms an alcohol ROH going in solution and leaves a hydroxyl ion on the monomer molecule. Hydrolysis can be described by the following reaction equation:

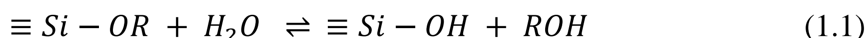

$$\equiv Si-OR + H_2O \rightleftharpoons \equiv Si-OH + ROH \quad (1.1)$$

Full hydroxylation of the monomer is only possible with excess water under catalysed conditions. Usually, mostly partially hydrolysed intermediates are present.

Polymerization by formation of a siloxane (Si-O-Si) bond and thus formation of a network takes place due to condensation of those metal hydroxide species, which (depending on the grade of hydroxylation) can be either an alcohol producing or a water producing reaction:

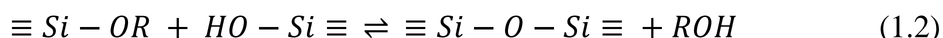

$$\equiv Si-OR + HO-Si\equiv \rightleftharpoons \equiv Si-O-Si\equiv + ROH \quad (1.2)$$

For the alcohol producing reaction an alkoxide (OR) and a hydroxyl group (OH) form alcohol ROH, leading to the formation of the siloxane bond.

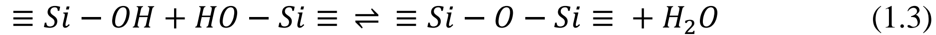

$$\equiv Si - OH + HO - Si \equiv \;\rightleftharpoons\; \equiv Si - O - Si \equiv \; + H_2O \qquad (1.3)$$

For the water producing reaction, two hydroxyl-groups react and a Si-O-Si bond is formed. The continuous formation of siloxane bonds by these reactions leads to a 3-dimensional, interconnected porous network of inorganic material, which is completely saturated by liquid (solvent). Each of these reactions can take place at each ligand of the silicon alkoxide. The number of chemically reactive ligands is called functionality.

To accelerate the chemical reactions, acidic or alkaline catalysts can be employed.

Gelation: For a solution, undergoing hydrolysis and condensation, the viscosity is related to the particle size and is time dependent. At the gel point the viscosity changes dramatically, the solution loses its fluidity and the appearance changes to that of an elastic solid. This transformation, from a state where individual particles are only weakly interacting with each other to a continuous molecular network occupying the entire volume, is called sol-gel transition and the product is called lyogel. As a result of the condensation reaction, the polymeric clusters grow. During this growth they decrease in density so that the effective volume fraction of the polymer increases. The time needed for gelation depends on the employed catalyst and the temperature.

Aging: During aging (or syneresis) the gel starts to shrink and increases in stiffness by reduction of the porosity. This process of spontaneous contraction of the gel network is affected by time, temperature and the pH value. Aging takes place due to the chemical reactions causing gelation, which continue long after the gel point because of the large concentration of remaining hydroxyl groups. Liquid is expelled from the gel network as the gel contracts when forming bridging bonds between two silicon atoms, which is illustrated in figure 1.4. This process continues to contract the network as long as the solid phase remains flexible.

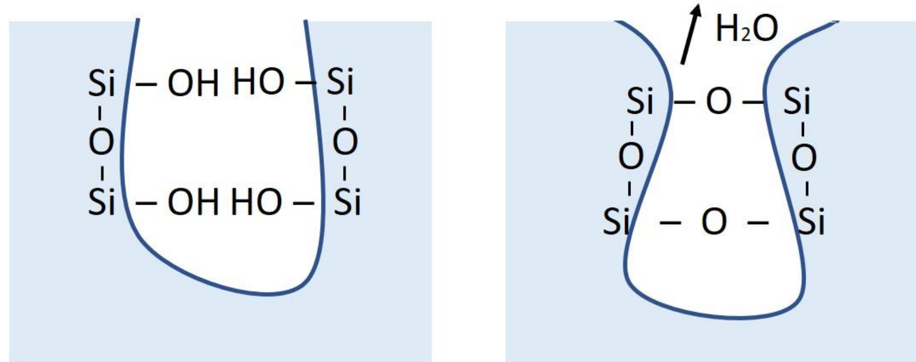

Figure 1.4.: Illustration of the process of pore contraction by the formation of bridging bonds.

Drying: This step is necessary to remove the liquid left in the pores of the interconnected network. For materials, which have pore sizes smaller than 20 nm, large capillary stress appears, causing massive cracks in the gel. Drying can be described in four sub-steps and leads to the formation of a xerogel:

- Constant rate period: This process takes place at the liquid-vapor interface of the material and can be regarded like drying of a liquid in an open container. The evaporation rate is time-independent and can only slightly differ depending on the surface texture. The gel shrinks by the same volume as the liquid which evaporates. Adsorption and capillary forces induce flow of the liquid from inner pores in order to replace the liquid evaporating from the surface. This leads to an increased stiffness and decreased porosity of the gel.
- Critical point: At this point the network can withstand the capillary forces. The shrinkage stops due to the increased stiffness of the network, but cracks start to appear. The formed gel particles start to rearrange into a closer packing, which is easy at the beginning because of the gel like structure, but eventually becomes harder as they become too crowded to rearrange as shrinkage proceeds. The release of compressive forces excreted on the network leads to a slight expansion as drying continues beyond the critical point.
- First falling rate period: The evaporation rate decreases, leading to an increase of the surface temperature. The outer parts shrink faster than the inner ones, leading to a fracturing of the network. Liquid from the pores inside the network flows to the pores located at the surface, where most of the evaporation takes place.

- Second falling rate period: The flow of the remaining liquid from the inside to the surface stops, because the outer areas become too dense, with the remaining liquid being trapped in pockets. The drying only continues by vapour diffusion, leading to a further deceleration of the drying process.

For some applications, no volume loss is desired. In these cases, a special drying method, called supercritical drying, is used. There, the liquid from the pores is removed at temperatures and pressures higher than the critical temperature and critical pressure of the respective material to avoid shrinkage and fracture by capillary forces. Drying under these conditions leads to the formation of an aerogel.

Sintering: Densification is the last treatment step. It describes the reduction of the pore number and their connectivity induced by heat treatment at elevated temperatures, close to the glass transition temperature of the final material, where it starts to move by a viscous flow (only valid for amorphous materials). The porous gel structure is transformed into a dense glass structure, when there are no more pores left and the density reaches the one of fused quartz or fused silica. Sintering depends on whether a gel was prepared in basic or acidic conditions, as the latter generally has a higher surface area and starts to densify at lower temperatures.[50,51]

An illustration of the different steps of the sol-gel process leading to dense films, aerogels, dense ceramics and uniform particles, starting from a metal alkoxide precursor is shown in figure 1.5.

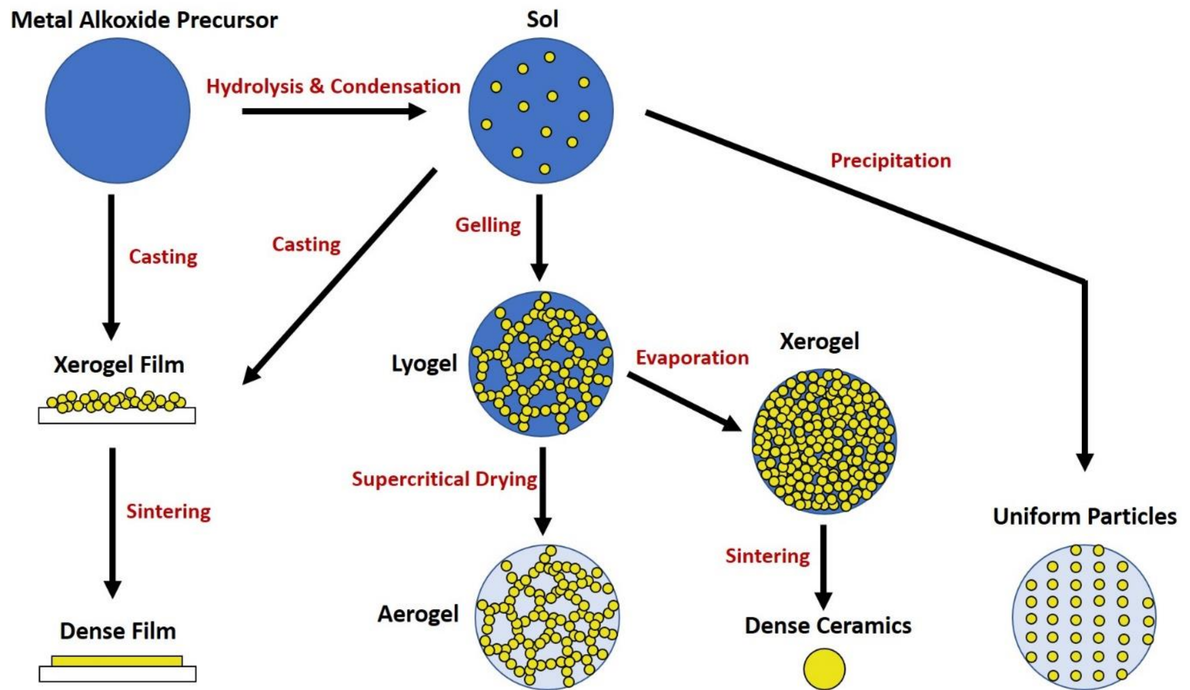

Figure 1.5.: Schematic diagram of the different steps of a sol-gel process and the different final products.

1.2.2 Sol-Gel Fabrication of Carbides

A carbide is a compound material consisting of C and an element with less electronegativity. The sol-gel process, besides other fabrication techniques, can be used for the fabrication of a variety of different carbides. This technique offers advantages like the relatively low synthesis temperature, the availability of a number of different precursor materials and a good accuracy to achieve specific compositions.[52] Also, the adjustment of the synthesis conditions and temperature allow the control of the morphology, porosity and size of the final product. Due to the liquid precursor material in sol-gel synthesis, infiltration of templates is possible. The different morphologies that can be obtained include e.g. nano- and micro-particles, fibres, spheres, needles and coatings.[53] Commonly known representatives for carbides which find application in different fields are for example titanium carbide (TiC), zirconium carbide (ZrC), boron carbide (B_4C), tungsten carbide (WC) and SiC, but also more exotic species like hafnium carbide (HfC). Typically, alkoxides of the respective metal species and e.g. phenolic resin are used as precursor materials for the sol gel-process as described in chapter 1.2.1. The last process step includes a high temperature treatment,

typically carbothermal reduction, where the required temperatures for the transformation depend on the species.[54–56]

1.2.3 Sol-Gel Fabrication of SiC

For the sol-gel synthesis of SiC a variety of different materials can be employed as Si-source, where Si alkoxides represent the main class of network forming agents used. The most commonly alkoxides used as Si-source are tetramethoxysilane $Si(OCH_3)_4$ (TMOS) and tetraethoxysilane $Si(OCH_2CH_3)_4$ (TEOS). TMOS leads, compared to TEOS, to a faster hydrolysis reaction but has the disadvantage that toxic methanol is generated during this process step.[52,57]

As carbon source, a variety of different materials can be used, as has been demonstrated in different reports. These include phenyl compounds but also, natural substances like sucrose, rayon fibres or wood.[58–60] Independent from the used Si- and C-source, the first step of the sol-gel process is the preparation of a sol containing the respective C- and Si-source, water as well as a catalyst and a solvent. This sol undergoes gelation, aging and drying as described in section 1.2.1., which leads to the formation of a carbon rich silicate glass. In the last step this silicate glass undergoes a carbothermal reduction process in inert atmosphere where SiC is formed. The final product is crystalline SiC powder or whiskers.

1.3 Photovoltaics

1.3.1 Solar Energy

The technological progress of mankind was always tightly connected to the energy harvested from nature. Since the beginning of the industrialization in the second half of the 18th century, human labour was gradually replaced by other energy supplies, resulting in a growing demand for energy. The fossil fuel petroleum was discovered in the 19th century, marking a further step in energy evolution. It is a geological deposit of organic material which was transformed over millions of years under high temperature and pressure and has a high energetical content when combusted.[61] Nowadays about 82% of the world primary energy supply originates from fossil fuels in form of coal, gas or oil. Over the last decades more and more research effort is invested in renewable energy. This trend emerged not only because of the limited resources of fossil fuels on our planet, but also due to the negative

effects of burning fossil fuels. The consequences of the resulting emission of CO_2 on the environment, force governments to support this mission of utilizing alternative natural energy sources.[62,63] Cleaner alternatives as energy sources include wind, hydro, geothermal, bio and solar power.[64] Compared to the others mentioned, solar energy offers several advantages. It can be harvested in most geographical regions, as it does not need special conditions like wind- or hydro-power and can be used in small scales of single households, but also megawatt plants. Furthermore, the installation is relatively simple and solar panels have no moving parts, which significantly extends their lifetime compared to other technologies that require costly maintenance.[65] One of the challenges which still have to be overcome is the high fabrication and material cost for commercially available solar panels. Presently, this still results in costs for energy generation, which are higher, not only compared to fossil fuels, but also to some other renewable energy sources.[66] Extensive effort is put in to the research of alternatives to silicon-based photovoltaics for sustainable solar energy conversion.

The progress in the research of photovoltaics and obtained power conversion efficiencies from the late 1970s till now is illustrated in figure 1.6.[67] Solar cells using a single or multi-crystalline silicon wafer as active layer are called first generation solar cells and currently reach power conversion efficiencies (PCE) of more than 26%. Even though being very cost-intensive, they still dominate the commercial market because of their high stability and efficiency.[68] Second generation solar cells emerged from the approach of lower material cost by using thin film technologies for the deposition (e.g. CVD) of active layers on low-cost substrates like stainless steel or ceramics. The active layers of this generation have a thickness of few micrometres and consist of inorganic materials like amorphous silicon, cadmium telluride (CdTe), copper indium gallium selenide (CIGS) and related materials.[69] Solar cells from the 3rd generation are solution-processible and consist of organic materials (e.g. polymers or small molecules) and inorganic nanoparticles (e.g. quantum dots). Hybrid solar cells made from e.g. perovskites also belong to this group. The maximum efficiency of organic solar cells currently reaches 12.3% and is therefore not suitable for the commercial market despite cost-efficient large-scale production.[70] Expensive high-performance multi-junction cells also belong to the 3rd generation and exhibit up to 46% efficiency - the highest efficiency levels ever detected.[71]

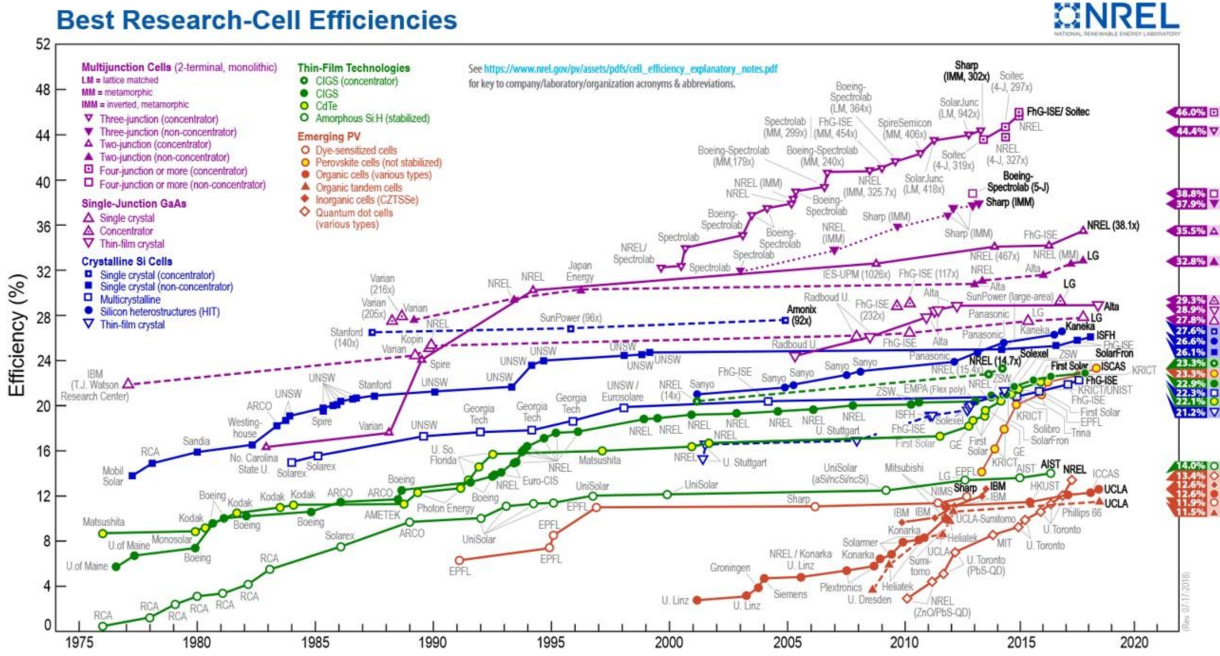

Figure 1.6.: Illustration of the progress and current solar cell efficiencies of various technologies.[67]

1.3.2 Organic and Hybrid Solar Cells

For organic as well as hybrid photovoltaics the right combination of materials is crucial to achieve good charge transport between the different phases leading to good PCEs. This section will discuss commonly used and well-investigated organic donor and acceptor materials, as well as inorganic acceptor materials. Further an overview of device architectures and the basic steps of charge generation by light harvesting will be given.

1.3.2.1 Active Layer Materials

<u>Organic donors:</u>

Conventional polymers, like polystyrene or polypropylene, are colourless insulators. The reason lies in their backbone, which comprises merely C-C single bonds, leading to generation of σ-orbitals. They possess no mobile charges and do not interact with electromagnetic waves in the visible range due to their too large σ/σ* energy gap (typically ~5 eV). There is another special class of polymers, called conjugated polymers, which are intrinsically conducting because of their molecular architecture. The backbone of a conjugated polymer is illustrated in figure 1.7. It consists of alternating single and double

bonds between carbon atoms. This configuration leads to formation of π-bonds, additional to the σ-bonds. The π-bonds allow the transport of electrons and their π/π* energy gap is small enough to interact with light. For a conjugated polymer, the overlap of multiple π-orbitals of the sub-units creates a system of delocalized π-electrons perpendicular to the planar skeleton of the backbone. This leads to the formation of a band-like structure, similar to conduction and valence band in an inorganic solid. The highest occupied molecular orbital (HOMO) forms the binding part equivalent to the valence band and the lowest unoccupied molecular orbital (LUMO) the anti-binding part equivalent to the conduction band. The bandgap energy lies in the visible and near infrared range (1.5 eV – 3 eV), allowing the formation of photogenerated charges upon excitation. This class of polymers exhibits extraordinary optical and electronical properties. Their conductivity can be changed by several orders of magnitude by doping to suit the requirements of specific applications. For p-doping the polymer is oxidized leading to a positive charge (removing an electron from the HOMO) and for n-doping it is reduced possessing a negative charge (adding an electron to the LUMO).[72–74]

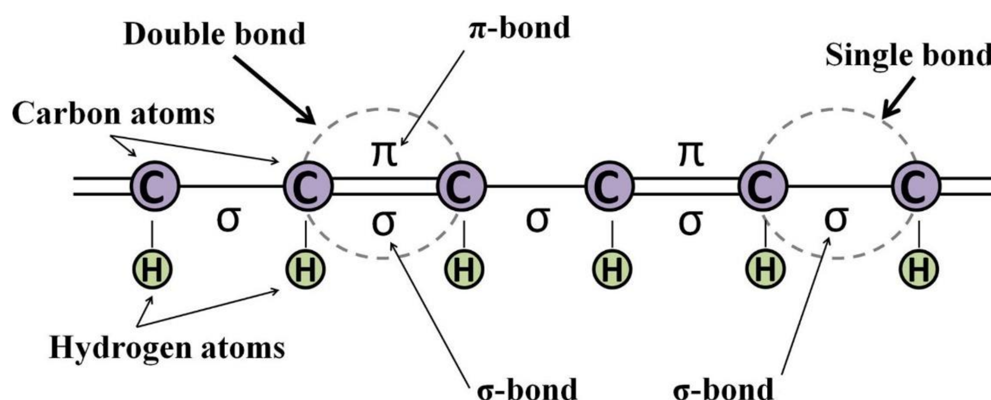

Figure 1.7.: Illustration of the backbone of a conjugated polymer with alternating single and double bonds.[72]

The first donor materials researched were based on poly(phenylene vinylene) derivatives that offered only low charge carrier mobilities and had a relatively large bandgap, limiting the light absorption and therefore the PCE. With the potential shown by these experiments, a lot of research has been carried out to push this field further. Nowadays, one of the most commonly used and well researched conjugated polymer in organic electronics is poly(3-hexylthiophene) (P3HT). It has a bandgap of about 1.9 eV, allowing absorption in a broad range of the visible spectrum. Furthermore, it is soluble in commonly used organic solvents

(e.g. Xylene) and offers a good charge carrier mobility. Another popular representative is poly[2,6-(4,4-bis-(2-ethylhexyl)-4*H*-cyclopenta[2,1-*b*;3,4-*b'*]dithiophene)-*alt*-4,7-(2,1,3-benzothiadiazole)] (PCPDTBT) as it has improved light harvesting abilities in the near-infrared wavelength range. The molecular structures of P3HT and PCPDTBT are depicted in figure 1.8. on the left and on the right, respectively.[75–78]

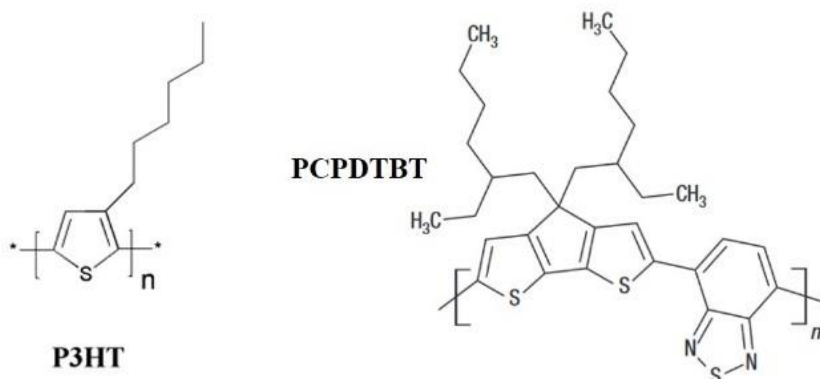

Figure 1.8.: Molecular structure of P3HT (left) and PCPDTBT (right).[78,79]

Organic acceptors:

Typically used organic materials for this purpose are derivatives of the Buckminster fullerene C_{60}, which was discovered in by H. W. Kroto in the 1980s (see figure 1.9., left).[80] Fullerenes belong to the group of small molecules and are arranged in a carbon cage structure consisting of hexagonal and pentagonal carbon rings. They can be regarded as 3-dimensional conjugated π-electron system.[81] These buckyball molecules display great properties for the use in photovoltaics like a high electron affinity, high mobility of electrons and low reorganization energy. The disadvantage of using the Buckminster fullerene (C_{60}) and its derivatives as acceptor molecules is its poor contribution to light absorption in the visible spectral range due to the high structural symmetry. Stronger absorption features only appear in the UV part of the spectrum. To suit specific requirements, the basic properties can be tailored by attaching different side groups to e.g. improve the solubility and tune the energy levels (to a certain extent) or surface energy.[82,83] Fullerenes used as acceptor molecules in organic electronics are for example [6,6]-phenyl-C_{61}-butyric acid methyl ester ($PC_{60}BM$) or Indene-C_{60} bisadduct (ICBA), which are shown in the middle and on the right of figure 1.9., respectively. Their HOMO and LUMO levels are lower than those of commonly used donor polymers, which is desired for application in organic solar cells (for more details see section 1.3.2.1.).[84,85]

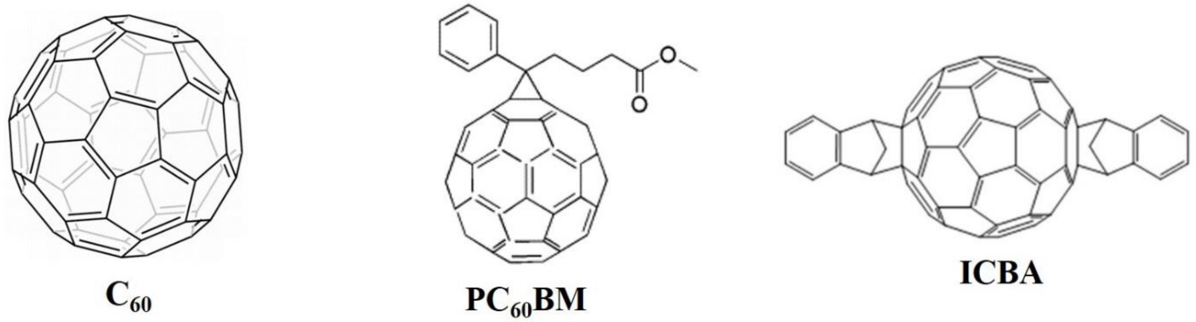

Figure 1.9.: Molecular structure of the Buckminster fullerene (left) and two of its derivatives PC61BM (middle) and ICBA (right).[77,79,86]

Inorganic acceptors:

A wide range of inorganic semiconducting materials is suitable for this application. Typically used and well investigated materials for polymer-nanocomposite solar cells include for example CdTe, cadmium sulfide (CdS), cadmium selenide (CdSe) and lead sulfide (PbS).[87] Furthermore, it was shown that SiC is a suitable candidate in its cubic configuration.[88] Compared to fullerenes, the inorganic semiconducting nanomaterials are able to contribute better to light harvesting in the visible range. Another benefit is that individual structuring of the materials and surface modifications are possible.[89] The bandgaps of inorganic nanoparticles can be tuned by adjusting the nanoparticle size. If they are smaller than the Bohr radius of the respective material, size reduction leads to a shift of the electronic excitation to higher energies due to the quantum confinement effect. This kind of particles, also referred to as quantum dots, are regarded as 0-dimensional and typically have a size of 1 – 10 nm. Quantum rods, e.g. carbon nanotubes, are an example for 1-dimensional particles.[90,91] The aggregation or oxidation of the inorganic particles should be avoided, to allow sufficient charge transfer. This could be done for example by the application of ligands, acting as surfactants, to the surface of inorganic particles. The choice of surfactant should be made carefully, as the charge transport might be lowered through the nanoparticle polymer interface, resulting in a poorer performance.[92]

A schematic energy level diagram of several organic and inorganic semiconducting materials as well as electrode materials is summarized in figure 1.10.[82,88,93–97]

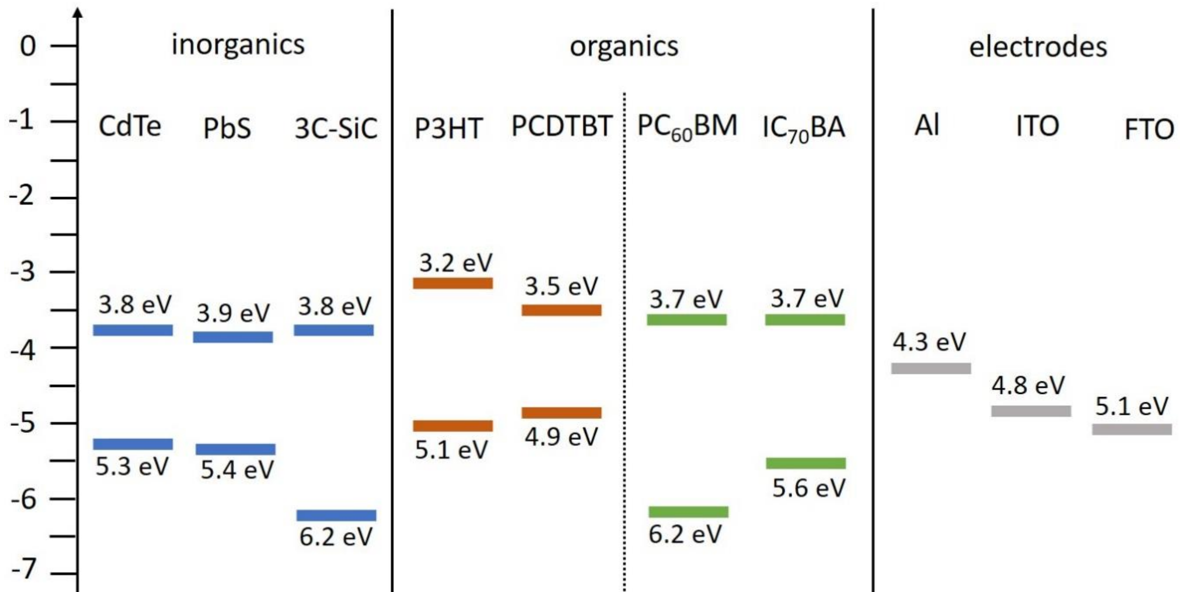

Figure 1.10.: Overview of the energy levels of commonly used organic and inorganic materials used in organic and hybrid photovoltaics.

1.3.2.2 Device Architecture

The architecture of solar cells is crucial as it can heavily affect the overall efficiency. For commonly used device structures, like single layer, bilayer and bulk heterojunction (BHJ) devices, the active layer is wedged between two electrodes. One of the electrodes must be transparent in the visible range to allow the absorption of photons in the active layer. Generally high work function metal oxides are used, like indium tin oxide (ITO) and fluorine-doped tin oxide (FTO). The second electrode is usually a low work function metal, e.g. Al, which reflects the incoming light (see figure 1.10.).[98,99]

Single layer devices:

Single layer diodes represent the simplest device architecture, where the active layer consists of a single phase sandwiched between two electrodes with asymmetric work functions (shown in figure 1.11., left). This architecture enables a dual function of the device: it works as a light emitting diode (LED) under forward bias and creates photoinduced free charge carriers under reverse bias. When used as a solar cell, the potential difference between anode and cathode needs to be high enough to generate free charge carriers, which massively limits the performance of such devices.

Bilayer devices:

To enhance the charge carrier generation, bilayer devices consisting of an electron donor and an electron acceptor material stacked on top of each other are used, as illustrated in figure 1.11., middle.[98] Bilayer devices yield very low PCEs because of the low exciton diffusion length in organic materials combined with the low interface area between donor and acceptor phase, meaning that only excitons created close to the interface can contribute to the generation of charge carriers.[100]

Bulk heterojunction devices:

The fabrication of BHJ devices was a breakthrough in the field of organic solar cells towards higher performances. The first successful implementation of BHJ solar cells was reported in 1995.[101] This device architecture allows an intimate intermixture of donor and acceptor phase of ideally 10 – 20 nm domain size, leading to a massive increase in the interfacial area, which results in a significantly higher number of excitons reaching the interface within their diffusion length.[77] Figure 1.11. on the right shows a device in BHJ architecture, where an electron transport layer (ETL) and a hole transport layer (HTL) are incorporated. As HTLs, commonly molybdenum trioxide (MoO_3) or conductive polymers like poly(3,4-ethylenedioxythiophene)-poly(styrenesulfonate) (PEDOT:PSS) are used, which also act as electron blocking layers. ETLs prevent hole transport to the cathode and protect the sensitive polymer from the hot metal atoms during thermal evaporation. Lithium fluoride (LiF) is a material typically used for this purpose.[84,102] Beside the above discussed conventional BHJ devices, also BHJ solar cells in inverted configuration are topic of current research. In these devices the high work function electrode collects the electrons (cathode) and the low work function electrode (anode) the holes and also the position of the ETL and HTL are adapted corresponding to the electrodes.[103,104] Nowadays, most studied BHJ devices employ conjugated polymers like P3HT as donor and a C_{60}-derivative as acceptor material. The control of the blend morphology, in terms of the formation of domain sizes in the range of 10 – 20 nm and percolated pathways to the electrodes, continues to remain a challenge.

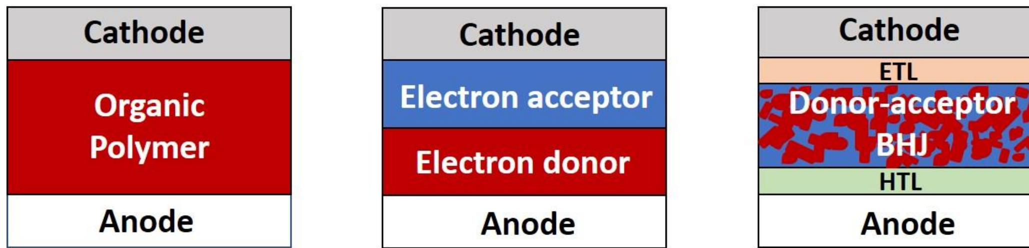

Figure 1.11.: Schematic illustration of single layer devices (left), double layer devices (middle) and devices in the BHJ geometry (right).

1.3.2.3 Hybrid Bulk-Heterojunction Devices

There are different types of hybrid systems like dye-sensitized, nanoparticle-sensitized, perovskite solar cells and solar cells in the bulk heterojunction geometry. The first successful fabrication of hybrid solar cells was reported in 2002, where CdSe nanorods were embedded in a P3HT matrix.[105]

From this point on, the general term hybrid solar cell will be used for hybrid solar cells in the bulk heterojunction concept, as they are the ones fabricated and investigated in the scope of this thesis. Hybrid solar cells comprise the benefits of both classes of materials (for details see section 1.3.2.1.). The advantages of organic materials are easy synthesis, relatively low production cost, light weight and the solution-based fabrication of devices.[77] For inorganic materials, the doping levels (for p- and n-doping) can be easily tailored by adapting the synthetic route to match the energy levels of organic materials. Nanoparticles offer large surface areas, supporting efficient charge separation and can also provide high absorption coefficients and photoconductivity as well as good electrical properties.[106] The fabrication and operation of hybrid solar cells is very similar to that of organic solar cells. The main difference is that the organic acceptor material is replaced by an inorganic acceptor, so that nanosized particles in form of crystallites or even more complex structures like rods, wires or tetrapods are embedded in a polymer matrix.[87]

1.3.2.4 Working Principles

The process of photoinduced charge carrier generation in organic BHJ solar cells is illustrated in figure 1.12. in form of a schematic band diagram and includes several physical mechanisms:[77,107]

- Absorption of photons:

Photons are only absorbed when their energy is equal or higher than the band gap energy of the absorbing material. Excess energy is thermalized.

- Generation of excitons:

An exciton is the excited state of a molecule. It can be seen as a quasiparticle (electron-hole pair), that is generated after light absorption in the donor material by lifting an electron to the LUMO band, while a hole remains on the HOMO. It is a mobile (within diffusion length limits) excited but neutral state with a finite lifetime.

- Diffusion of excitons:

Diffusion of the exciton in the donor material to the donor/acceptor interface takes place as long as there is no recombination between electron and hole, within the exciton diffusion length of 10-20 nm.

- Dissociation of excitons:

For this step a high internal electrical field is necessary. It is generated by the difference in the HOMO energy of the donor and the LUMO energy of the acceptor material, which creates a gradient in the chemical potential of electrons and holes at the donor acceptor interface. The result is a charge-transfer state, with a hole on the donor site and an excited electron on the acceptor site, which are strongly bound by Coulomb attraction.

- Separation of electron-hole pair:

The Coulomb attraction (typically around 0.4 eV) needs to be overcome in order to separate the photoexcited excitons into free charge carriers at the donor/acceptor interface. The driving force for this step is the work-function offset between the two electrodes.

- Charge transport towards the electrodes:

Free electrons move through the acceptor and free holes through the donor material, dominated by hopping transport. Band-like transport along conjugated units occurs, but is interrupted by breaks in conjugation within or between molecules. The mobility of the charge carriers can be reduced by traps.

- Charge collection at the electrodes:

Finally, the electrons and holes are collected at the respective electrodes. The Fermi energy of the anode material must be larger than the HOMO energy of the donor and the Fermi energy of the cathode smaller than the LUMO level of the acceptor.

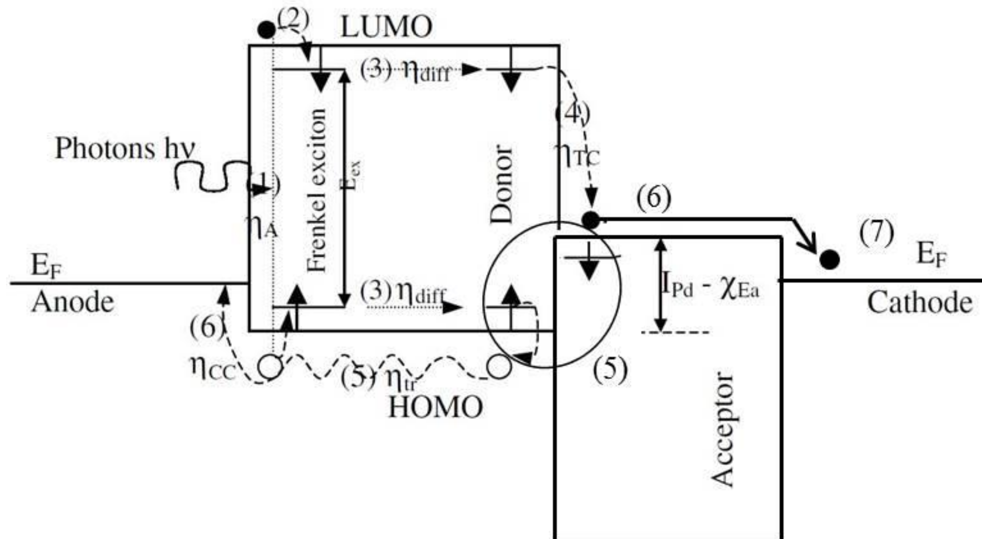

Figure 1.12.: Schematic illustration of the basic steps for photoinduced charge carrier generation in an organic BHJ device.[107]

The working principle of organic-inorganic hybrid solar cells is very similar to the one of organic devices. But there is one major difference: the magnitude of the exciton binding energy. In organic semiconductors the binding energies are high (about 1000 meV), requiring the shifted band gaps and resulting differences in HOMO and LUMO energy of donor and acceptor material as driving force for the dissociation of excitons. These tightly bound excitons are called Frenkel excitons, depicted in figure 1.13 on the right. In inorganic materials, excitons with much lower binding energies (between 4 meV and 30 meV for commonly used semiconducting materials) are generated, called Mott-Wannier excitons, shown in figure 1.13. on the left. Their weak bonding is a result of the relatively high dielectric constants. Therefore, Mott-Wannier excitons can be easily separated by thermal energy and lattice vibrations.[91,92,108–110]

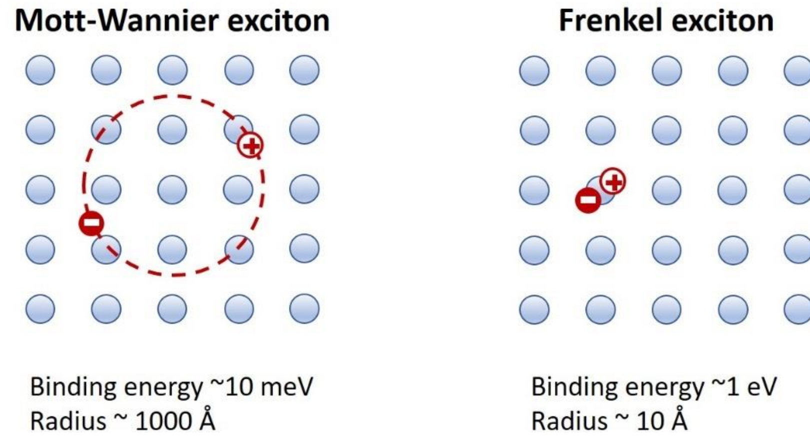

Figure 1.13: Illustration of weakly bound Mott-Wannier excitons and tightly bound Frenkel excitons.

1.4 Objectives and Structure of the Thesis

Hybrid photovoltaics are topic of extensive research as they combine the benefits of both, organic and inorganic semiconductors. One of the issues that hybrid solar cells suffer from is the toxicity of commonly used materials, which are e.g. lead- or cadmium-based compounds. SiC is a good alternative as it offers merits like a high electron affinity, high electron mobility and low toxicity. The cubic polytype 3C-SiC has the smallest bandgap (2.4 eV) among all polytypes and therefore is the most suitable for the use in photovoltaics.

Here a novel application for SiC is demonstrated as an electron co-acceptor in organic inorganic hybrid solar cells. In this study a bottom-up approach for preparation of suitable SiC powder samples with different dopants for integration in organic semiconductor films is used. The material is obtained by a sol-gel-based and carbothermal reduction-assisted fabrication route. The process is suitable for the fabrication of material of the cubic polytype in the nano- to microscale and even enables in-situ n- and p-doping. This allows more cost-efficient fabrication of high-purity and high-surface area material than commonly used top-down methods like e.g. via wet chemical etching.

The present thesis is arranged in three experimental chapters:

The first chapter is included as published peer-reviewed scientific article “Characterization of Surface and Structure of In Situ Doped Sol-Gel-Derived Silicon Carbide” and deals with the sol-gel based synthesis of N- and Al-doped SiC powders and the determination of their bulk and surface properties.

The second chapter is dedicated to the implementation of N-doped Sic in organic/inorganic bulk-heterojunction hybrid PV devices where it acts as acceptor/co-acceptor within an organic matrix consisting of the common conjugated P3HT and $PC_{60}BM$ acting as donor and acceptor, respectively.

The third chapter describes the fabrication of Ga-doped SiC with different nominal doping concentrations and discusses their impact on the defect density, surface termination and morphological characteristics. Further, hybrid solar cells with high and low co-acceptor fractions of Al-, Ga- and N-doped SiC are fabricated. The device physical and photophysical characteristics of the solar cells are investigated in reference to the applied dopant.

2 EXPERIMENTAL AND CHARACTERIZATION

In this chapter the process steps and materials used for the synthesis of SiC powders and solar cell devices are described. Further, the details of the analytical methods used for characterization are given.

2.1 SiC Synthesis and Device Fabrication

2.1.1 Sol-Gel Fabrication of SiC Powders

Tetraethyl orthosilicate (TEOS, Sigma Aldrich, ≥ 99%) and sucrose (Sigma Aldrich, puriss.) were employed as Si and C source, respectively. A xerogel, with a Si to C ratio of 1:4, was prepared using the process steps as described in the following. A visual summary of the process is shown in figure 2.1. First, TEOS and ethanol (Sigma Aldrich, ≥ 98%) as solvent were mixed under magnetic stirring. Then the saccharose and one of the doping materials (sodium nitrate, Sigma Aldrich, ≥ 99%; metallic aluminium powder, 5 µm, 99.5%; Gallium(III) ethoxide, Alfa Aeser) were dissolved in water (deionized) under magnetic stirring at mild heat (about 50°C). When fully dissolved, HCl (Sigma Aldrich, 37%, puriss.) was added to accelerate the gelation of the Si-C sol. A TEOS:H_2O:HCl ratio of 1:8.2:27 was used. All materials were used as received without any further purification. The sol was placed in a drying cabinet in a closed glass container at 60°C for at least 12 h for gelification. To remove the excess water and residual solvent, the lyogel was placed in an open glass container on a hot plate at 150°C for at least 24 h. The resulting xerogel was placed in a tube furnace and annealed at 1000°C for 3.5 h under Ar flow leading to the formation of a C rich silicate glass. The last step is the carbothermal reduction of the precursor, carried out in an induction furnace at a temperature of 1800°C for 10 min in static Ar atmosphere, where SiC powder is formed.

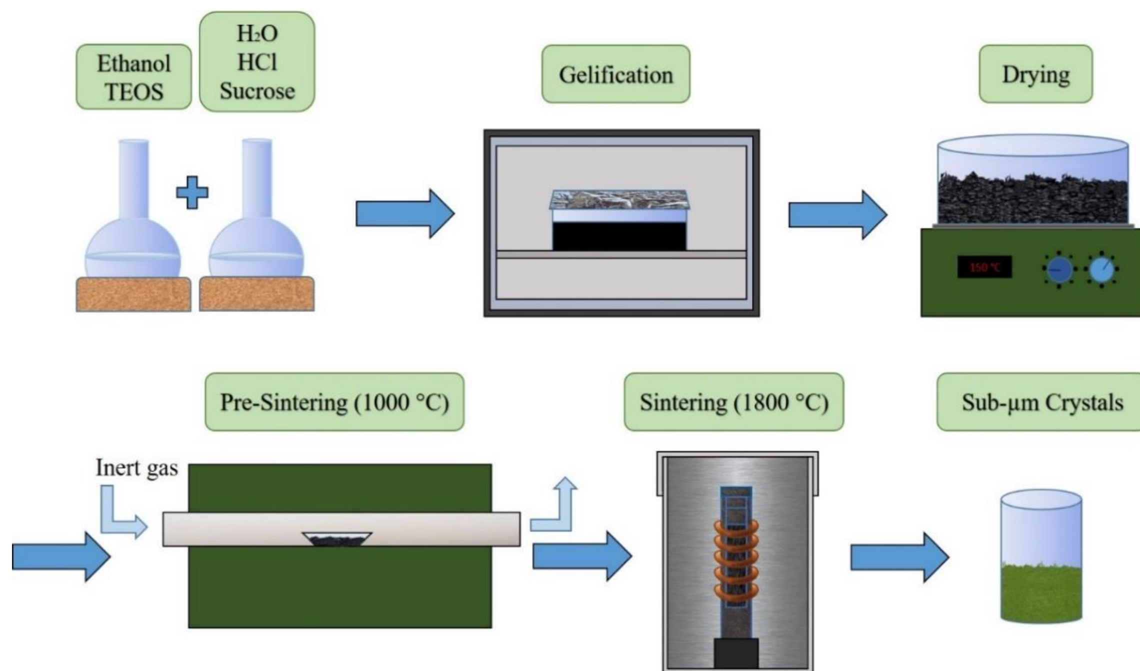

Figure 2.1: Schematic illustration of the different process steps involved in the sol-gel based carbothermal reduction synthesis of SiC.

2.1.2 Solar Cell Device Fabrication

Materials used:

- Prepixelated anode substrates:
  Glass with ITO (Indium-doped tin oxide (SnO_2:In, 20 Ω/square), Ossila Ltd.)
- Buffer layer:
  PEDOT:PSS (poly(3,4-ethylenedioxythiophene) polystyrene sulfonate) with a PEDOT:PSS ratio of 1:6 (Heraeus-Clevios GmbH., P Jet OLED, aqueous ink)
- P3HT (Rieke Metals LLC., RMI-001 EE)
- $PC_{60}BM$ (Nano-C inc., 99.5% purity)
- Doped SiC powder, synthesized in-house
- Chlorobenzene (anhydrous, 99.8%, Sigma-Aldrich)
- Cathode: Aluminium (Goodfellow GmbH, 99.999%)
- Encapsulation epoxy resin (Robnor Resins, PX681)

The photoactive layer materials P3HT and $PC_{60}BM$ were used as received, the SiC powder was synthesized in-house (see chapter 2.1.1.). The solutions/suspensions for the active layer were prepared from anhydrous chlorobenzene at least 24 hours before sample preparation

and stirred and heated at 70°C to allow complete dissolution of the materials. The pixelated anode substrates, illustrated in figure 2.2 on the left, were cleaned via sonication in acetone and isopropanol (IPA) for 10 min, followed by drying under a CO_2 gas stream. Afterwards the surface was activated by O_2-plasma treatment (100 W, 10 min) to achieve the desired low work function of the ITO. Immediately after the plasma treatment, a PEDOT:PSS electron blocking layer was spin coated from aqueous suspension (sonicated for 10 min and filtered by a 0.2 µm PP filter) at 4000 rpm for 40 sec under ambient conditions, followed by annealing at 180°C for half an hour under Ar flow to remove the residual moisture from the thin films. This leads to a desired film thickness of about 40 nm. In the next step the samples were immediately transferred to an Ar filled glove box to prevent the hygroscopic PSS from water uptake. In the inert atmosphere the active layers were spin coated on top of the hole transportation layer at 2220 rpm for 60 sec from hot solution (70°C). Annealing of the films was carried out on a hotplate at 140°C for 10 min, to allow the polymer to recrystalize and thereby increase the device performance.[111] Each device was completed by the evaporation of an Al cathode through a shadow mask which defines the device active area of 4.5 mm^2. The evaporation was carried out at a base pressure of $1.5 \cdot 10^{-5}$ mbar or below with an evaporation rate of around 0.4 - 0.8 Å/s to a thickness of 100 nm. After I-V measurements in the dark and under illumination were performed in inert atmosphere, the devices were encapsulated with a two-component epoxy resin and a cover glass slip to perform further measurements in ambient conditions. An illustration of a completed solar cell is shown in figure 2.2 on the right.

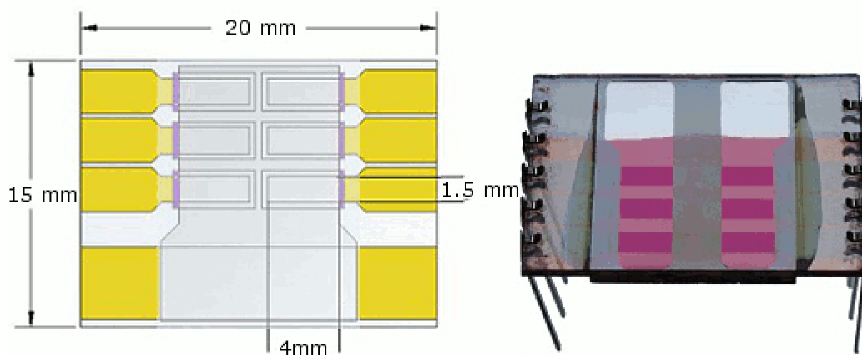

Figure 2.2: Schematic illustration of the pixelated anode substrate (left) and photograph of a solar cell device (right).[112]

For conducting photophysical measurements, spectrosil quartz glass substrates were used. They were cleaned with the same procedure as used for cleaning the solar cell device

substrates. Here only the active layer was deposited, followed by annealing under the same conditions as mentioned above.

For acquiring XPS measurements, indium platelets were used, where the SiC powder samples were pressed on. For infrared measurements the samples were prepared the same way.

2.2 Analytical Methods

2.2.1 Optical Microscopy

Optical microscopy is a technique which uses light in the visible range to investigate the topography of samples. An optical microscope can operate in two different modes: the bright field mode (figure 2.3 on the left) and the dark field mode (figure 2.3 on the right). The bright field mode uses light that is projected from the lamp through the imaging optic to the sample. The light which is reflected by the sample is imaged by the microscope optics. In order to investigate samples in the dark field mode they are placed on an opaque base underneath the condenser lens. Only light that hits the sample from the side is used (usually provided by an external light source placed next to the sample), while the central part of the illumination beam is blocked. The light which reaches the microscope optics originates from reflections of the sample on the slide and is collected from the same optical path as for bright field images.[113]

For topography investigations of SiC powder samples and solar cell devices an optical microscope from Olympus (model BX52) equipped with a camera (Olympus Wide Zoom, modelC-5060) was used to record light and dark field images. The software Olympus DP-Soft 5.0 was used to edit the images.

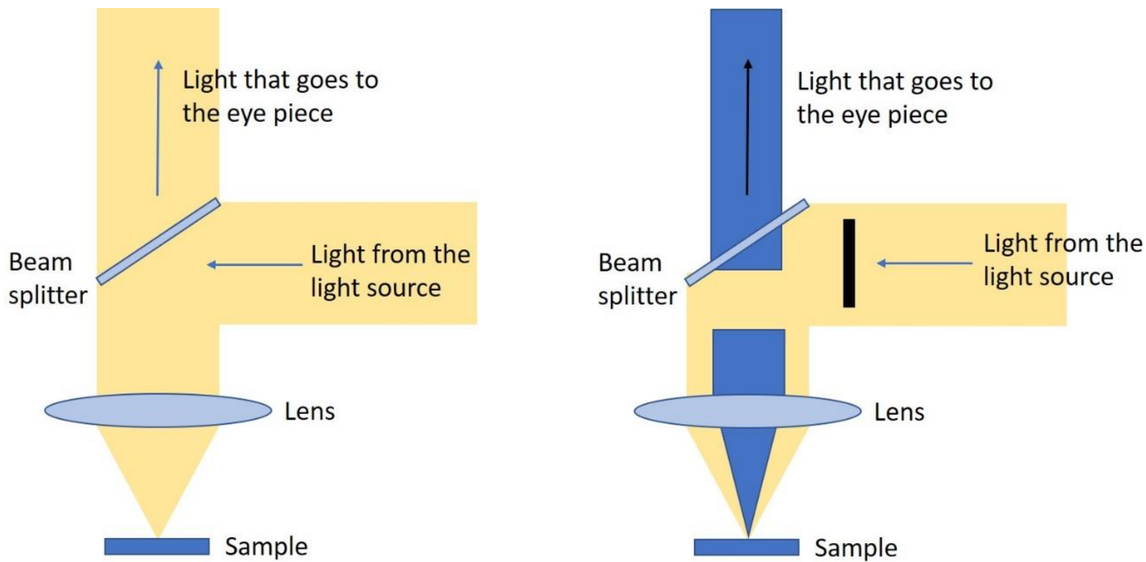

Figure 2.3: Schematic illustration of bright field imaging (left) and dark field imaging (right).

2.2.2 Scanning Electron Microscopy (SEM)

Scanning electron microscopy uses the interaction of a focused electron beam with a sample to create images with high magnification. The electrons are generated by an electron source, accelerated and then focused in order to scan across the sample line by line under high vacuum conditions. High vacuum is necessary to reduce interactions with gas molecules, as this would negatively impact the imaging quality. Depending on electron energy and target density the electrons can penetrate the sample in the range of 10 nm to 10 µm (black bulb in figure 2.4).[114] The interaction of the electron beam with the sample gives information at each point of the sample. The retrieved signal is usually not simply from a single scattering event but a multitude of different interactions. Various different signals are generated, most commonly used are: secondary electrons (SE) backscattered electrons (BSE), Auger electrons (AE) and X-ray radiation (X).

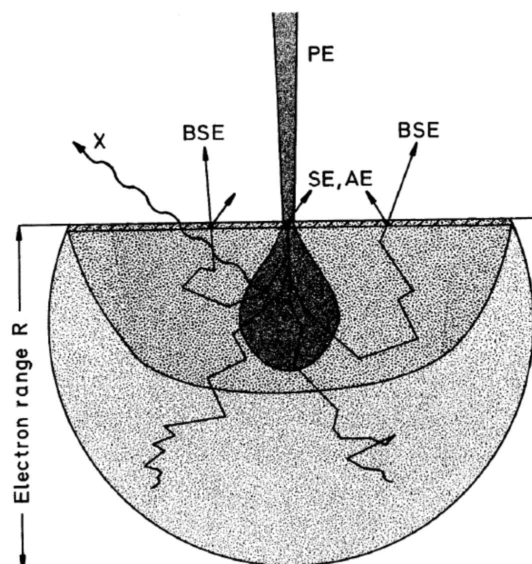

Figure 2.4: Schematic depiction of the information depth and lateral extension of an electron beam with a sample and the origin of different signals (AE: Auger electrons, SE: Secondary electrons, BSE: back scattered electrons, X: X-ray radiation).[114]

SE are low energy electrons which are excited upon inelastic scattering and per definition have energies below 50 eV. The information yielded from SE has the best resolution of all SEM signals and mainly stems from the topography (i.e. the first few nanometres of the sample). The reason for this is that SE from further inside the sample are reabsorbed and cannot reach the surface. This results in a resolution down to a few nanometres, close to the diameter of the electron beam.

BSE are higher energy electrons with energies higher than 50 eV. BSE are elastically back scattered from the nuclei of the sample atoms. Because of their higher energy they can have an origin deeper in the sample, which results in a larger information volume. The larger exit area of BSEs leads to a worse lateral resolution compared to SE. The image resolution can be improved by using electrons with lower energies. The contrast in BSE-SEM images is from chemical differences in the sample, i.e. different atomic number Z.[115]

X-ray radiation (Bremsstrahlung and characteristic X-rays) is produced when the electron beam interacts with the sample. On the one hand, the so-called Bremsstrahlung is emitted when the electrons are decelerated in the vicinity of the sample. The lost kinetic energy is converted into X-ray radiation, creating a continuous background, which does not yield any information on the sample. On the other hand, characteristic X-ray radiation stems from the

interaction of the electron beam with the sample and can be used to analyse the chemical composition. The characteristic X-rays depend on the sample, as they are emitted when an electron from the beam interacts with an inner shell electron and ejects it. The excited atom then relaxes to its ground state by filling the inner shell with an electron from a higher shell and the emission of an X-ray photon. As the set of transitions (from higher to lower shells) is limited, the emitted photons are characteristic for each element. The depth of the production of X-ray radiation depends on the energy of the electron beam and can only be produced in the region where the electron beam penetrates the sample and the electrons still have enough energy to eject electrons from the inner shells of atoms. Therefore, the region of X-ray production is always smaller than the electron beam penetration. Therefore, the lateral resolution is restricted by the width of the beam-sample interaction (black bulb in figure 2.4). The analysis is usually carried out with either EDX (energy dispersive X-ray spectroscopy) but can also be done with WDX (wavelength dispersive X-ray spectroscopy). EDX evaluates the energy of the radiation and allows qualitative and quantitative analysis.[115]

The experiments in this thesis where carried out on a Zeiss DSM982 Gemini equipped with a thermal field emission gun as electron source and an Everhart Thornley Detector.

2.2.3 Transmission Electron Microscopy (TEM) and Electron Energy Loss Spectroscopy (EELS)

This technique allows to study a wide range of materials including ceramics, polymers, glasses, semiconductors and metals. The specimen investigated with a TEM are analogous to thin films, but without a carrier substrate. They need to be transparent to electrons, which means that a sufficient number of electrons must be able to transmit in order to get a high enough intensity at the detector (scintillator or direct CCD). The thickness of the film necessary for getting an interpretable image is dependent on the electron energy and the average atomic number Z of the specimen and therefore depends on the investigated material. Specimen can be prepared by a variety of different methods, where the choice of preparation technique depends highly on the sample composition. One preparation method is by a focussed ion beam (FIB). Here, a single ion gun generates a well-controlled beam of i.e. Ga atoms used for thinning of the specimen which includes several different process steps until the desired thickness is reached.

The different scattering processes which occur are schematically depicted in figure 2.5. As electrons are charged particles, they are strongly scattered at the electron clouds surrounding

the nuclei of the atoms. Electrons which are scattered elastically represent the major source of contrast in a TEM image. As they traverse the specimen, they do not lose any energy. Elastic scattering is mainly coherent but becomes more incoherent at higher angles of scattering. Inelastically scattered electrons, also called energy-loss electrons, are equally important as this kind of scattering creates a wide range of signals which contain information on the chemistry of the specimen. Inelastic scattering is always incoherent and can create beam damage and heat the sample. Additionally, several other signals arise, where the most important ones are secondary electrons and characteristic X-rays.[116]

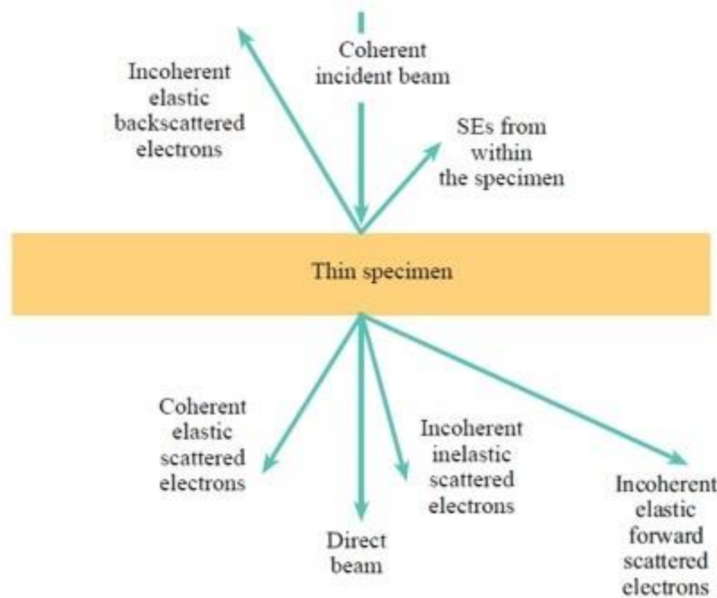

Figure 2.5 Illustration of the different kinds of scattering arising from a thin specimen.[116]

Different elements present in different regions of the sample can be identified from spectra which exhibit characteristic peaks. An analysis method which allows not only to identify but also to quantify elements present in a sample can be conducted via electron energy loss spectroscopy (EELS). This method can also yield information on chemical bonds. The typically recorded EELS spectrum shows a plot of the electron intensity versus the energy loss and can be separated in the low-loss region (figure 2.6, a) and the core-loss region (figure 2.6, b). The zero-loss peak originates from electrons that pass the specimen without scattering and from elastic scattered electrons where the energy loss is negligible. In almost all solids, a collective effect occurs: the oscillation of electrons. This leads to the occurrence of plasmon peaks. Compared to the low-loss part of the spectrum, the high-loss part has a much smaller intensity. In this part of the spectrum ionization edges in different shapes

belonging to the core electron can be found with an edge threshold depending on the binding energy of each shell. White line peaks are a fine structure of the ionization edges appearing close to the edge threshold.[117]

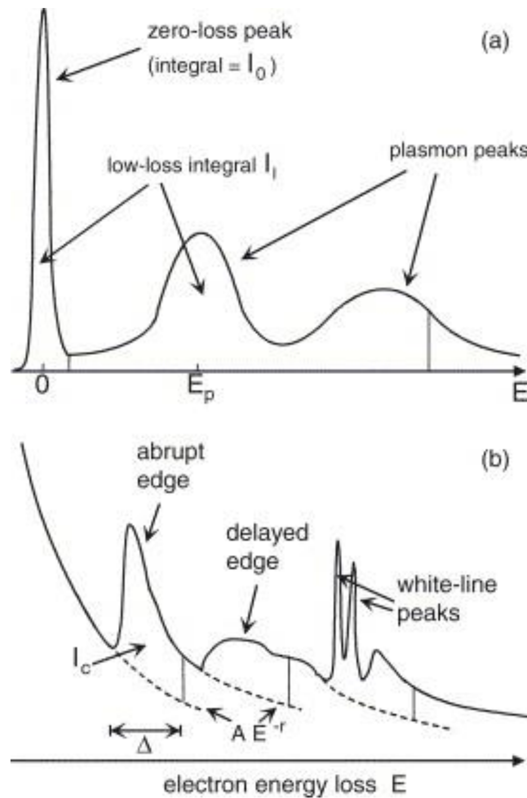

Figure 2.6: Schematic illustration of the low-loss region (a) and the core-loss region (b) of a typical EELS spectrum.[117]

In this thesis, TEM images were obtained using a **FEI Titan³ G2 60–300** equipped with a high brightness electron gun (FEI X-FEG) and a high sensitivity energy dispersive X-ray spectrometer (FEI ChemiSTEM technology with Super-X detector by Bruker). Cross-sectional slices of thin film samples were prepared by focussed ion beam (FIB/SEM Dual Beam Microscope FEI NOVA200 with Ga-ion source).

2.2.4 Electron Paramagnetic Resonance (EPR)

EPR spectroscopy is a tool which allows to identify paramagnetic defects in a material. This is called Zeeman splitting. The two states are separated by an energy differences ΔE which depends on the following formula:

$$\Delta E = g\ \mu_B\ B_0 = h\nu \qquad (2.1)$$

Here, g is the proportionality factor or g-factor, μ_B is the Bohr magneton, h is Planck`s constant and ν frequency of the electromagnetic radiation. The g-factor acts as a fingerprint for certain species. To determine ΔE, which depends linearly on the magnetic field, and to be able to calculate the g-factor, the samples are irradiated by microwave radiation with a fixed frequency while sweeping the magnetic field. Resonant absorption takes place when equation 2.1 is fulfilled, meaning that the energy difference of the two spin states matches the energy of the incident microwave radiation. Another less common approach is to keep the magnetic field constant and scan the frequency of the electromagnetic radiation. A schematic illustration of the working mechanism of EPR spectroscopy is shown in figure 2.7.[118,119]

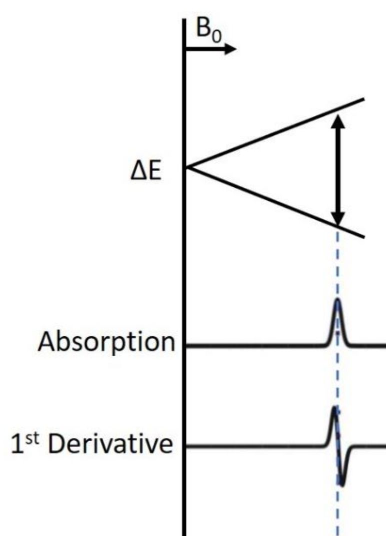

Figure 2.7: Schematic depiction of an EPR experiment.

EPR measurements were carried out using a conventional X-band (≈ 9.10 GHz with 0.01 GHz accuracy) spectrometer RE 13-06 with 100 kHz field modulation at 77 K by submerging samples in a cold-finger dewar filled with liquid nitrogen. The calibration of the magnetic field was carried out by using a polycrystalline DPPH standard with g = 2.0036 ± 0.0001. Quantitative analysis was performed by weighing approximately equal amounts (16 mg ± 20%) of SiC powder and comparing the double integral of room temperature EPR signals with a reference DPPH with a known number of spins ($2.6 \cdot 10^{16}$ ± 10%).

2.2.5 X-Ray Diffraction (XRD) and Rietveld Refinement

Crystal structures can be studied by diffraction of photons, neutrons and electrons, depending on wavelength and the structure of the specimen. Powder X-ray diffraction is a non-destructive method, extensively used for the investigation of crystal structures as the wavelength of the radiation is in the range of Ångström (Å) and thereby is in the same dimension as the spacing between the atoms. It allows to study the atomic arrangement of materials, and also the chemical composition and phase arrangement for samples where atoms are arranged in a periodic array. This method cannot be applied to amorphous materials, as they do not provide an atomic long-range order.

This technique uses a focused and monochromatic X-ray beam, which hits the specimen at selected angles. Diffraction only occurs when Braggs law (eq. 2.2) is satisfied.

$$n\lambda = 2d\sin\theta \tag{2.2}$$

Here n is the order of diffraction, d is the spacing between two lattice planes and θ the incident angle.

Braggs law is fulfilled for wavelength $\lambda \leq 2d$, which leads to constructive interference and detectable diffraction peaks. Each of these peaks can be attributed to certain sets of parallel lattice planes and so be used to analyse the atomic structure of a sample. An illustration of the diffraction law is shown in figure 2.8.

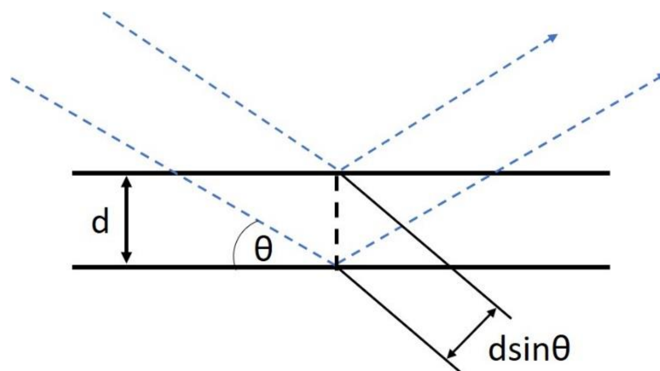

Figure 2.8: Illustration of Braggs law, where d is the distance between two adjacent net planes and θ the incident angle.

The information gained in form of diffraction angles and intensities is characteristic for each crystalline species and therefore allows a distinct identification.[91,120]

In this thesis an X-ray diffractometer in Bragg-Brentano geometry (Siemens D 501) was used. A schematic illustration of the set-up, where the X-ray tube and the detector are moved relative to each other circular around the sample is shown in figure 2.9. The radiation used was CuKα with a wavelength of 1.5418 Å and a graphite monochromator was used. The diffraction vector is always normal to the sample surface and indicated by s. The incident angle ω, between sample and radiation source, is always half of the diffraction angle 2θ between incident beam and detector. Both, X-ray tube and detector are rotated at a constant speed, to allow the detector to collect the diffracted radiation. The recorded patterns were identified by comparison with standard reference patterns.

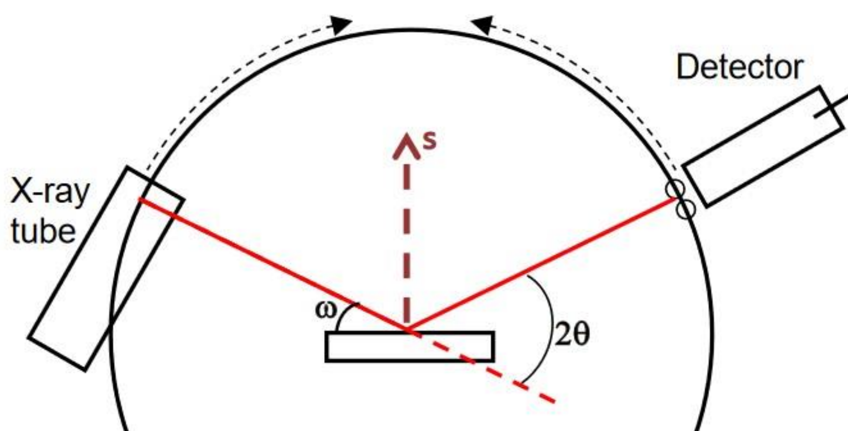

Figure 2.9: Schematic depiction of an X-ray diffractometer in Bragg Brentano geometry.[121]

Rietveld analysis is an iterative method that allows the refinement of the crystal structures from X-ray diffraction data which gives information about the atomic arrangement of the crystalline sample. The species and the according Bragg reflections need to be identified before using the Rietveld method. There the information content of an XRD pattern (peak position, peak intensity, peak shape and background) in the form of stepwise scanned intensity data is refined utilizing a least squares method. This approach, where the entire powder pattern needs to be modelled, compares the scanned and calculated pattern of a specific material with the aim to minimize the difference. The profile R-factor, which is a measure for the agreement between the measured and calculated pattern, is the value commonly used to evaluate the quality of the refinement.[122]

Rietveld refinements were performed using the software Bruker AXS, Topas Version 3.

2.2.6 X-Ray Photoelectron Spectroscopy (XPS)

X-Ray photoelectron spectroscopy (XPS) is a spectroscopic method used for the investigation of solids and gives valuable information about the composition and chemical states present at the surface. All elements except for hydrogen and helium can be detected through measurement of the binding energies of photoelectrons. The sample is irradiated by a beam of highly monochromatic, soft X-ray radiation. Commonly used sources are Mg Kα (1253.6 eV) or Al Kα (1486.6 eV). The absorption of these photons of the energy ħω leads to the emission of electrons from the core shells of the atoms, due to the photo-effect. A schematic illustration of this process is shown in figure 2.10. The kinetic energy E_{kin} of the emitted photoelectrons is measured by an electron energy analyzer and follows the formula:

$$E_{kin} = \hbar\omega - \phi - E_b \tag{2.3}$$

With ϕ the work function and E_b the binding energy.

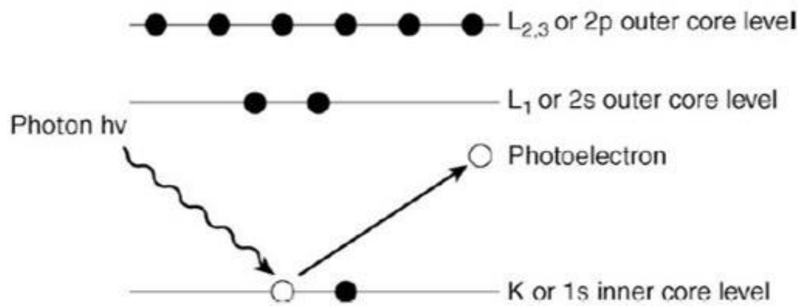

Figure 2.10: Schematic illustration of the emission of photoelectrons after excitation with X-rays.[123]

This method requires ultra-high vacuum and has a detection limit of 0.01 – 0.1 at.%. The variation of the binding energy of photoemission lines belonging to a certain element allow the identification of chemical states. The incident X-ray photons are able to penetrate many µm deep into the sample but the short path length of the photoelectrons make XPS a surface sensitive method. The sampling depth lies between 0.5 and 3 nm which equals 3 – 8 atomic layers.[123]

XPS measurements carried out for the investigation of the surface composition of differently doped SiC powder samples presented in this thesis were acquired using a monochromatic Thermo Fisher spectrometer equipped with a Mg Kα X-ray source. The spectra, recorded at

room temperature, were background corrected and Gaussian/Lorentzian mixed functions were used for peak fitting (software XPSPEAK41).

2.2.7 Reflection Absorption Infrared Spectroscopy (RAIRS)

Infrared (IR) spectroscopy is a commonly used spectroscopic method using light in the mid infrared range at wavelengths between 2.5 μm (4000 cm^{-1}) and 25 μm (400 cm^{-1}) which is rapid, sensitive and offers a variety of sampling techniques for samples in the gas, liquid and solid state. IR spectra provide information about the molecular structure of the investigated sample due to vibrations of the bound atoms that are caused by the absorption of infrared light. These vibrations can be distinguished in stretching vibrations, originating from changes in the bond length, and deformation vibrations, caused by a change in the bond angle. The latter can be further divided into bending modes, wagging modes, twisting modes and rocking modes. There are different measurement techniques which are based on transmission measurements or reflection measurements.

The measurement technique used in the scope of this thesis is the reflection absorption method RAIRS, where the investigated sample is placed on a reflective substrate as illustrated in figure 2.11. The incident infrared light, which hits the sample at an angle α, passes the sample twice leading to a kind of a transmission spectrum. The steeper α gets the longer the effective path length in the sample becomes. If the sample thickness exceeds the wavelength of the incident beam, the absorbance values correspond to the larger effective path inside the sample. Very thin samples lead to a dependence of the transmission not only on the optical properties but also on the variations of the regular field in the vicinity of the reflective surface the sample is placed on.[124]

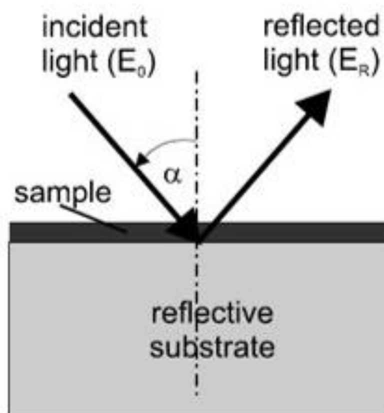

Figure 2.11: Measurement of reflection absorption where α is the angle of incidence.[124]

RAIRS spectra were obtained under vacuum with a base pressure of 4 mbar, utilizing a motorized polarizer and a reflection unit, both from Bruker Optics. The incident angle of the measurements was 74°.

2.2.8 Current-Voltage Characterization

There are four parameters, the so-called key parameters, which characterize a solar cell: The open circuit voltage (V_{OC}), the short circuit current density (J_{SC}), the fill factor (FF) and the power conversion efficiency (PCE), which is based on the previous three parameters. In the following these parameters will be discussed in brief. An exemplary depiction of current voltage characteristics, where the key parameters are obtained from, recorded in the dark and under illumination are shown in figure 2.12, plotted linearly (a) and semi-logarithmically (b). The characteristics in the dark show the diode behaviour of the solar cell where almost no current flows until charge carriers are injected by the electrodes for $V > V_{OC}$. To extract information about transport mechanisms and mobility of the charge carriers, the dark characteristic needs to be considered in a semi-logarithmic way. When the solar cell is illuminated by light in the visible wavelength range, power is generated in the fourth quadrant. The maximum current flows under short circuit current conditions. The maximum power point (mpp) is indicated by a yellow rectangle and shows the point where the product of V_{OC} and J_{SC} is a maximum.[125]

Open Circuit Voltage:

The V_{OC} is defined as the applied voltage where no current flows in the solar cell. For metal-insulator-metal devices this value is determined by the work function difference of the electrodes. The maximum V_{OC} in organic and hybrid solar cells that can be achieved is determined by the offset between the energy levels offset of the donor (HOMO) an acceptor material (LUMO/conduction band energy). Typically, losses of about 0.2 eV appear at each of the electrodes. Also, the nanomorphology of the active layer and the interface between active layer and electrodes in terms of oxide formation has an impact on this sensitive parameter.[77,126,127]

Short Circuit Current Density:

This parameter is a measure of the efficiency of a solar cell and scales with the device active area. If the contacts are regarded as loss free the J_{SC} is determined by the density of charge carriers generated upon light absorption and their mobility within the device:

$$J_{SC} = ne\mu E \tag{2.4}$$

Here n is the density of charge carriers, e is the elemental charge, μ the mobility and E the electric field. A lowered J_{SC} mainly stems from issues with the charge carrier mobility, as it is not only a material dependent parameter but also strongly influenced by the morphology of the active layer.[77]

Fill Factor:

The FF is calculated by values derived from the I-V characteristics and follows the following formula:

$$FF = \frac{J_{mpp} \cdot V_{mpp}}{J_{SC} \cdot V_{OC}} \tag{2.5}$$

Where J_{mpp} and V_{mpp} are the current and the voltage at the maximum power point. This value is a measure of the squareness of a solar cell and would reach 100% in an ideal device. In a real device this value is lower as there is a competition between transport and recombination of charge carriers.[77,125]

Power Conversion Efficiency:

The PCE can be calculated according to the following formula:

$$PCE = \frac{J_{SC} \cdot V_{OC} \cdot FF}{P_{in}} \cdot 100\% \tag{2.6}$$

P_{in} is the incident light power. The latter value is standardized at 1000 W/m^2 for the testing of solar cells to a spectral intensity distribution which is equal to that of the sun on earth at an incident angle of 48.2° (AM 1.5 G spectrum).[106]

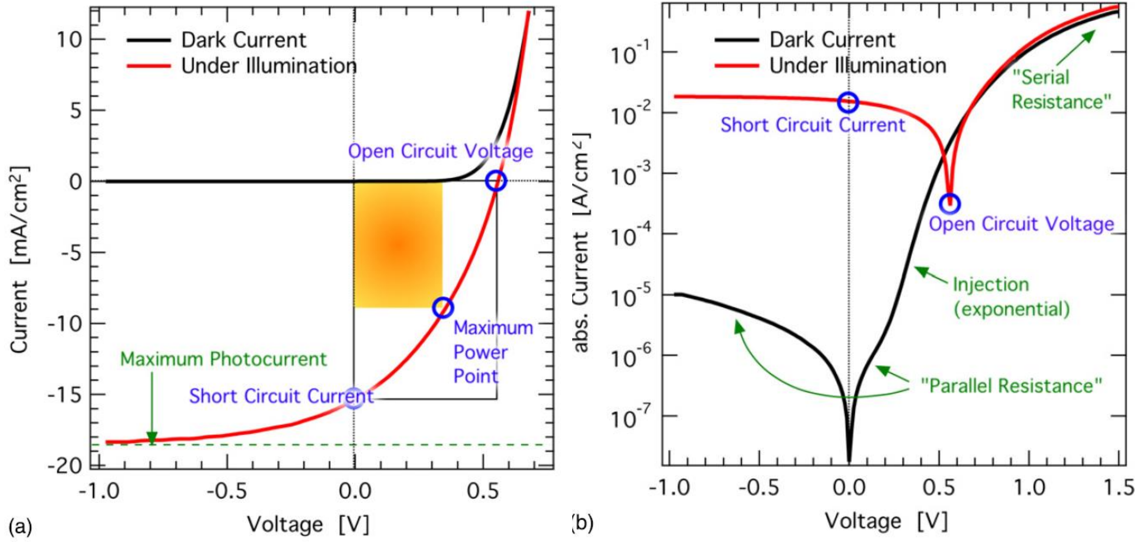

Figure 2.12: Illustration of typical I-V curves recorded in the dark and under ilumination, plotted linear (a) and semi-logarithmic (b).[125]

Current-voltage curves were recorded by sweeping the voltage in a step size of 0.02 V from -1.0 to +1.5 V for dark I-V curves and from -1.0 to +1.0 V for light I-V curves with a computer-controlled source meter (Keithley 2636A). Both measurements were performed in an Ar filled glovebox. Light I-V characteristics were carried out under AM 1.5 G conditions with 100 mW/cm^2. As light source a solar simulator from ABET technologies (model 10500) was used, which produces a collimated 25 mm beam. It is designated with a rating of ABB (spectral match between 0.75 and 1.25, irradiance spatial non-uniformity of 5% and temporal instability of 5%).

2.2.9 Spectral Response

Another important parameter, which characterises the performance of solar cells is the spectral response or external quantum efficiency (EQE). It gives information not only about current generation but also about recombination of charge carriers and their collection at the respective electrode. It can be calculated in % via the following formula:

$$EQE(\lambda) = \frac{1240 \cdot J_{SC}(\lambda)}{\lambda \cdot P_{in}(\lambda)} \quad (2.7)$$

Where $J_{sc}(\lambda)$ represents the short circuit current density at a certain wavelength, $P_{in}(\lambda)$ is the incident light power and λ is the wavelength.[128]

The spectral response is defined by the following equation:

$$S(\lambda) = \frac{e\lambda}{hc} \cdot EQE(\lambda) \qquad (2.8)$$

Here $S(\lambda)$ is the spectral response in the unit AW^{-1}, e the elementary charge of an electron, h is Planck's constant and c the speed of light.[129]

The external quantum efficiency is measured by shining white light through a monochromator and a filter wheel on the device and using a reference diode to detect the number of incident photons which are compared to the number of generated charge carriers. This measurement is usually performed for the whole visible wavelength range and therefore gives information about the current as a function of the wavelength of the incident light.

For this thesis, light of a 250 W tungsten halogen broad band white light source (built in house), a monochromator (Spectral Products, CM110) giving a wavelength resolution of 5 nm, a computer-controlled Keithley 2636 A source meter and a calibrated Si photodiode were used.

2.2.10 Transient Photocurrent Measurements

The measurement of transient photocurrents allows to gain information about dynamic processes taking place in organic and hybrid solar cells that are related to transit times of charge carriers, trapping and detrapping of charges and the dynamics of recombination. To acquire these characteristics, the thin films are excited with an optical square pulse and the response in form of a photocurrent is recorded by an oscilloscope. The duration of the square pulse of light, used to create the electron hole pairs has to be longer than the transit time that the generated charge carriers need across the device. The curves are typically recorded as a function of pulse illumination intensity or applied bias voltage.

A schematic illustration of two transient curves is illustrated in figure 2.13. The labels "On" and "Off" mark the time when the optical square pulse is switched on and off. In the upper image no transient photocurrent appears, indicating a trap free device. A different situation is depicted in the lower image, where two transient peaks with different polarities can be seen. The overshoot after switching on the optical pulse can be associated with build-up of charge carriers. The overshoot after switching off typically stems from a slow release of charge carriers. Negative spikes as shown in the lower image of the illustration also indicate

the presence of trap states. After switching on the light pulse the photocurrent will eventually reach the steady state photocurrent when the system is in equilibrium.[130–132]

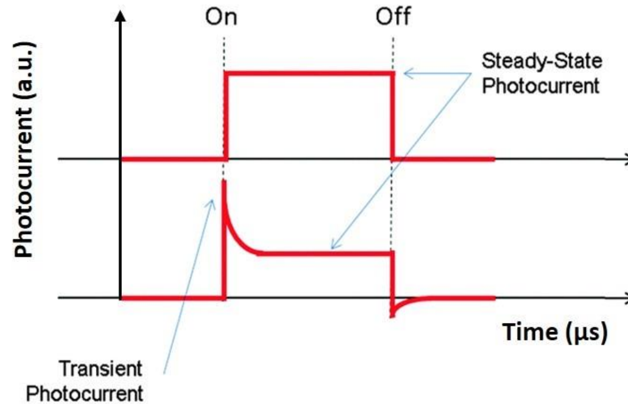

Figure 2.13: Schematic illustration of two photocurrent responses to a square light pulse, the upper one without a transient photocurrent and the lower one with. (adapted from [130])

In order to record the photocurrent transients, the devices were illuminated with a 530 nm green LED (Thorlabs, M530L2). To create a 300 µm square pulse of light a function generator at 1 kHz (HAMEG HMF 2550) was used. An oscilloscope (HAMEG HMO 3302 Series) with an input impedance of 50 Ω was used to detect the generated photocurrent. The voltage-dependent photocurrent transient curves were obtained by connecting the solar cells to a computer-controlled source meter (Keithley 2636A) in DC mode.

2.2.11 Light-Beam induced Current (LBIC) Measurements

LBIC measurements are a well-established method used to display the lateral photocurrent distribution of solar cell devices. Spatially resolved photocurrent maps are obtained by measuring the photocurrent generated by locally confined illumination of the devices. By scanning the whole active device area in steps of several µm, knowledge of local inhomogeneities like agglomerations, but also degradation can be gained.[133]

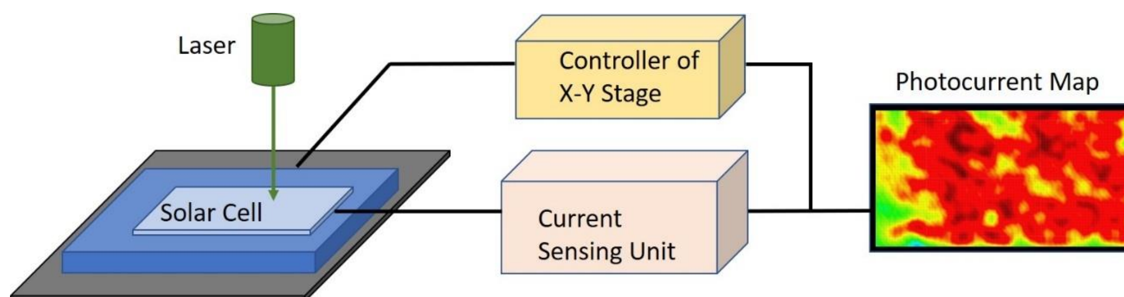

Figure 2.14: Schematic illustration of LBIC set-up and a resulting photocurrent map.

In the present work the samples were illuminated from the glass/ITO side by a 532 nm focused diode laser beam (<5 mW) with a spot size of ~ 2 µm. For spatial photocurrent mapping a custom written computer program and a 2D translation stage (NanoControl NC-2-3 from Kleindiek Nanotechnik) were used to raster scan across the photoactive area of 4.0 mm x 1.5 mm with a step size of 25 µm. The values of the local short circuit current were translated to a colour at each point which leads to a 2-dimensional photocurrent map, where dark red shows areas of the highest performance going through warm and cold colours to black for areas with the lowest photocurrent generation.

2.2.12 UV-vis Spectroscopy

UV-Vis absorption spectroscopy is the method of choice for the investigation of the absorption profile in the visible and ultraviolet wavelength range.

According to the law of Lambert-Beer, the absorbance depends on the absorption coefficient of the material and is directly proportional to the layer thickness of the sample. The intensity of the incident light beam decays exponentially.[134,135] The absorbance can be derived from the experimentally measured transmittance:

$$T(\lambda) = \left(\frac{I(\lambda)}{I_0(\lambda)}\right) \tag{2.9}$$

$$A = -log_{10}\left(\frac{I(\lambda)}{I_0(\lambda)}\right) = \varepsilon lc \tag{2.10}$$

This technique is based on the frequency dependent absorption of electromagnetic radiation of materials. Electrons are lifted up to a higher energy level, if the energy of the incident photons equals the difference of energy between two electronic states. Depending on selection rules only certain transitions are allowed. These transitions which are not only of electronic but also vibrational nature can be explained via the Franck-Condon principle

(illustrated in figure 2.15). It states that the motion of the nuclei setting up the molecular skeleton is much slower than the electronic transitions. As illustrated on the left-hand side of figure 2.15 these transitions are taking place for fixed positions of the nuclei, which is indicated by a straight arrow starting in the electronic ground state S_0 at the vibrational ground state $n_v = 0$. If there is no affection by the electronic excitation and therefore no displacement (indicated by the displacement coordinate X), the transition leads to the vibrational ground state S1.

A transition in that manner results in a spectrum consisting of a single sharp peak as shown in the upper right image of figure 2.15. If the excitation causes a shift in the position of the nuclei (lower left image) the electronic excitation is coupled to a vibrational one. This is indicated by the vertical arrow ending in the excited vibrational state $n_v = 1$ in the level S1. The result is a spectrum exhibiting a distinct fine structure (bottom right). Also transitions to higher or lower vibrational states are possible. By variation of the frequency of the incident light beam an absorption spectrum over the whole visible and ultraviolet range can be recorded.[74,113,135,136]

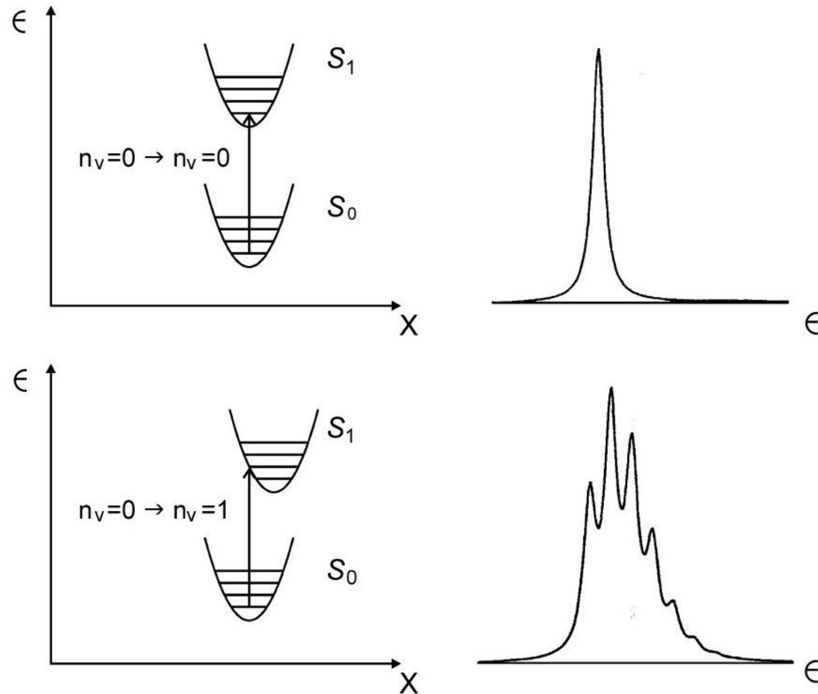

Figure 2.15: Schematic illustration of the Franck-Condon principle.[136]

Absorption spectra of the blends where recorded with a two-lamp spectrometer (halogen and deuterium) with an operation wavelength between 190 and 1100 nm from Shimadzu (UV-1800) allowing the measurement of the actual sample and a reference at the same time.

2.2.13 Photoluminescence (PL) and Quantum Yield (QY) Measurements

Luminescence in solids originates from the radiative recombination of excited electronic states, after being excited by an external source. Photoluminescence is a broad expression that can be roughly divided into long-lived phosphorescence (originating from a large range of inorganic bulk- and nano-materials) and short-lived fluorescence (originating mostly from small molecules, polymers and inorganic nano-materials), where for many applications it is not of interest whether the emitted light originates from phosphorescence of fluorescence. A big advantage of this method is that it is a non-contact and non-destructive method making it applicable to solids, solid suspensions, liquids and gasses. The physical principles behind PL spectroscopy can be explained by having a look at the Jablonski diagram (illustrated in figure 2.16). The absorption of a photon leads to the excitation of an electron from the electronic ground state (S_0) to a certain vibrational level ν of an excited state (e.g. S_1). Vibrational relaxation (VR) to the lowest vibrational level of the excited state typically takes place within 10^{-12} seconds. If the electron resides at a higher excitation level than S1 (e.g. S_2) it relaxes to S1 through internal conversion (IC) if a vibrational state of an excited state couples to a vibrational state of an electronically lower excited state. The ground state can then be reached by radiative (emission of a photon) or non-radiative decay. The non-radiative relaxation happens through internal conversion quenching, collisional quenching or intersystem crossing to a triplet excited state (T_1) which is usually located at a lower energy than the first excited state S_1. From T1 the electron can relax to S_0 either via emitting a photon or through internal conversion.[123,137,138]

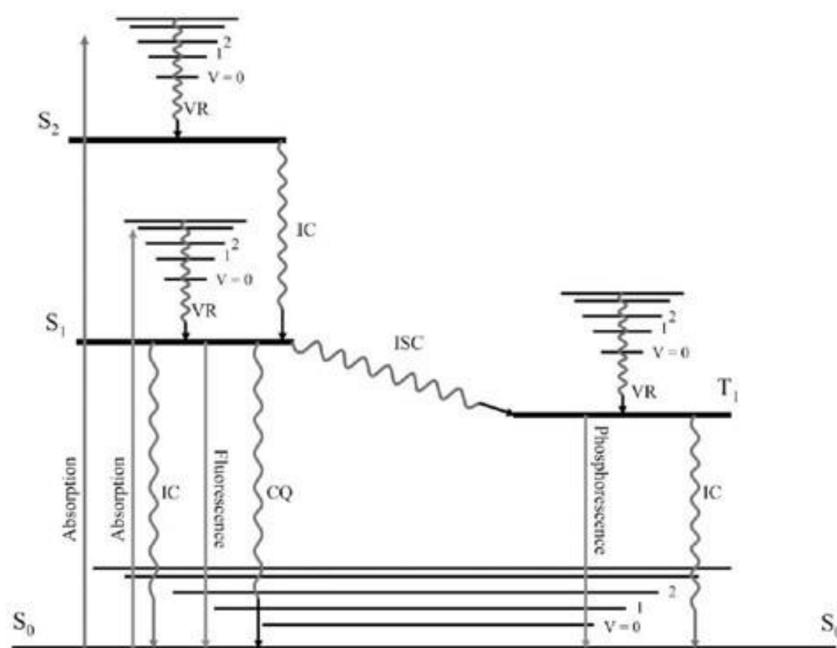

Figure 2.16: Schematic depiction of the processes behind PL on the basis of the Jablonski diagram.[123]

The luminescence quantum yield is defined as the number of emitted photons divided by the number of absorbed photons. This value can be measured either from solution or from the solid phase. The difficulty of this method is to determine the total emission in the full solid angle, which can be overcome by using an integrating sphere.[139]

PL spectra and resultant calculated QY, used to investigate the effectiveness of quenching between donor and acceptor materials, were obtained using a Fluorolog3 spectrofluorometer (Horiba Jobin Yvon) equipped with a photomultiplier sensitive in the near-infrared wavelength range (Hamamatsu R2658). The absolute luminescence QY was obtained using an integrating sphere (Horiba). The wavelength used for exciting the samples can be found in the respective chapters of this thesis.

3 RESULTS AND PUBLICATIONS

3.1 Characterization of Surface and Structure of In Situ Doped Sol-Gel-Derived Silicon Carbide

Olivia Kettner, Sanja Šimić, Birgit Kunert, Robert Schennach, Roland Resel,

Thomas Grießer, and Bettina Friedel

Author Contributions

The following paper is published in the Journal of Advanced Engineering Materials. It is inserted here as original publication together with the supplementary information.

The author and Bettina Friedel defined the research plan. The author synthesized the doped SiC powder samples. The author recorded the SEM images together with Sanja Šimić. Birgit Kunert recorded the XRD powder diffraction patterns and carried out the Rietveld refinement. The derived results were discussed with Roland Resel. The results from the IR measurements were interpreted with the help of Robert Schennach. The author did the literature review, evaluated and interpreted the data and wrote the manuscript. The project was supervised by Bettina Friedel.

FULL PAPER
ADVANCED ENGINEERING MATERIALS
Silicon Carbide
www.aem-journal.com

Characterization of Surface and Structure of In Situ Doped Sol-Gel-Derived Silicon Carbide

*Olivia Kettner, Sanja Šimić, Birgit Kunert, Robert Schennach, Roland Resel, Thomas Grießer, and Bettina Friedel**

Silicon carbide (SiC), is an artificial semiconductor used for high-power transistors and blue LEDs, for its extraordinary properties. SiC will be attractive for more applications, but large-scale or large-surface area fabrication, with control over defects and surface is challenging. Sol-gel based techniques are an affordable alternative toward such requirements. This report describes two types of microcrystalline SiC derived after carbothermal reduction from sol-gel-based precursors, one with nitrogen added, the other aluminum. Characterization of their bulk, structure, and surface shows that incorporation of dopants affects the formation of polytypes and surface chemistry. Nitrogen leads exclusively to cubic SiC, exhibiting a native oxide surface. Presence of aluminum instead promotes growth of hexagonal polytypes and induces self-passivation of the crystallites' surface during growth. This is established by hydrogenation of silicon bonds and formation of a protecting aluminum carbonate species. XPS provides support for the suggested mechanism. This passivation is achieved in only one step, solely by aluminum in the precursor. Hence, it is shown that growth, doping and passivation of SiC can be performed as "one-pot synthesis". Material without insulating oxide and a limited number of defects is highly valuable for applications involving surface-sensitive charge-transfer reactions, therefore the potential of this method is significant.

1. Introduction

Silicon carbide is a high-temperature stable, non-oxidic ceramic and first been synthesized by Acheson in 1890,[1] and due to its high Mohs hardness of 9.3, was widely produced and used as an abrasive.[2] Still today, SiC is an important material, used to improve mechanical and thermal properties of machine parts,[3] and preventing from wear in abrasive or corrosive environments.[4,5] But SiC is also a wide band gap semiconductor, highly attractive for high power transistors, light emitting diodes, and solar cells, due to its extraordinary electrical properties, often referred to as the third generation of semiconductor materials.[6–9] Silicon carbide appears in more than 200 polytypes, which differ by the stacking sequence of the Si–C tetrahedrals.[10] However, obtaining semiconductor grade material is comparatively more challenging: Single crystals from hexagonal polytypes can be grown via sublimation, where mostly nitrogen-doped or nominally undoped wafers are commercially available.[11] Initially p-doped material is rare because the deeper valence band of wide bandgap materials makes it hard to reach sufficient densities,[12] but can be established post-growth via ion-implantation or CVD epitaxial growth. Cubic polytype 3C-SiC, can merely be grown by heteroepitaxial growth, for example, on silicon,[13] also nitrogen-doped or nominally undoped. However, lattice mismatch and different thermal expansion coefficients lead to mechanical tension in the grown material, with tendency to cracking, therefore 3C-SiC wafers are enormously expensive.[14]

SiC preparation via sol-gel processing is a low-cost, solution-processable and environmentally-friendly addition to those traditional methods,[15] with the potential to expand into further fields of applications particular by its ability to facilitate the production of large-area and high-surface area materials. It is suitable for fabrication of nano- to microscale films, of nano- to microparticles and bulk materials alike.[16] As has been shown, its high degree of freedom regarding precursor composition even enables in situ doping, such as highly doped n-type SiC:N obtained by the introduction of nitric acid or sodium nitride, and p-type SiC:Al with reasonable charge carrier densities by introduction of aluminum chloride or metallic aluminum powder during wet-chemical precursor preparation.[17,18] Thereby, evidence supporting the dopants presence and position in the SiC material was found by electron paramagnetic

Prof. Dr. B. Friedel
illwerke vkw Endowed Professorship for Energy Efficiency, Energy Research Center, Vorarlberg University of Applied Sciences, 6850 Dornbirn, Austria
E-mail: bettina.friedel@fhv.at

Prof. Dr. B. Friedel, O. Kettner, B. Kunert, Prof. Dr. R. Schennach, Prof. Dr. R. Resel
Institute of Solid State Physics, Graz University of Technology, 8010 Graz, Austria

S. Šimić
Graz Centre for Electron Microscopy (ZFE), 8010 Graz, Austria

Prof. Dr. T. Grießer
Institute of Chemistry of Polymeric Materials, Montanuniversität Leoben, 8700 Leoben, Austria

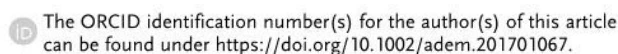
The ORCID identification number(s) for the author(s) of this article can be found under https://doi.org/10.1002/adem.201701067.

DOI: 10.1002/adem.201701067

 © 2018 WILEY-VCH Verlag GmbH & Co. KGaA, Weinheim

ADVANCED SCIENCE NEWS
www.advancedsciencenews.com

ADVANCED ENGINEERING MATERIALS
www.aem-journal.com

resonance spectroscopy and associated modeling of the related defect signals for N- and Al-doping, respectively.[16,19] This motivates a broadening of SiC's application range toward new fields, such as the electronic acceptor in organic/inorganic hybrid photovoltaics, as robust photoelectrode in catalysis and for nanostructured blue light emitters, where nanoscale or large surface area is required.[20,21] In particular from hybrid solar cells, it is a well-known fact that the surface properties of the inorganic component substantially determine the efficiency of the device, for example, via surface trap states fostering trap-mediated recombination or inter-particle charge transport limitations, caused by their stabilizing ligands.[22–24] In the case of silicon carbide nanoparticles within a conjugated polymer matrix, Kettner et al. have observed extended emission lifetimes, assigned to the formation of longer lived polarons upon photoinduced electron transfer to the inorganic acceptor or surface trap states,[21] which have been suggested in either case to be beneficial for their function in hybrid photovoltaics.[25] However, also here the surface is the most crucial point, when incorporating SiC nanoparticles into the organic semiconductor matrix of a hybrid solar cell.

Investigations on the surface of traditionally derived SiC have been done in the past, for example, by Mac Millan et al.,[26] Afanesev et al.,[27] and Kaplan.[28] Thereby, they mainly focused on the formation of native oxide (SiO_2) on hexagonal SiC and the interface formation between SiC and SiO_2, also depending on which site was exposed, Si or C. Formation of native oxides on SiC is a strong disadvantage for most (opto)electronic applications, as the insulating SiO_2 layer hinders charge transfer. Further, it has been reported that SiC can show considerable densities of surface defects under certain circumstances, for example after etching processes. In one important example, namely blue emitting porous SiC, those defects can detrimentally diminish the original emission properties, and subsequent surface passivation is vital.[29]

In this paper, our experimental observations regarding the dopant-related surface termination of sol-gel derived 3C-SiC crystalline particles are reported. The work aims to give new insights in the special characteristics of surface formation in doped sol-gel derived cubic SiC and, therefore, is a further step to exploit the full potential of this material. The work is based on thorough surface characterization utilizing X-ray photoelectron spectroscopy (XPS) depending on the introduced dopant. This is accompanied by results on their crystallite size, unit cell and polytype distribution, as characterized by scanning electron microscopy (SEM) and X-ray diffraction (XRD) with Rietveld refinement.

2. Experimental Section

2.1. Preparation of Silicon Carbide Powders

Silicon carbide sub-micrometer powders were fabricated via sol-gel processed precursors and their carbothermal reduction, which is described in detail elsewhere.[17,18] All chemicals used for the fabrication of the precursor material were purchased from Sigma-Aldrich and used as received without any further purification. In brief, sucrose (>98.5%) as carbon source and tetraethoxysilane (TEOS) (≥99%) as silicon source were dissolved in deionized water and ethanol (≥98%), respectively, to get a carbon-rich silica-sol in ethanolic solution as precursor material. The silicon-to-carbon ratio was adjusted to 1:4 and hydrochloric acid (37%) was added as the catalyst. The molar ratio between metal-organic precursor, water and catalyst TEOS:H_2O:HCl is at 1:8.2:27. For p- and n-doping, the precursors were modified by adding nominally 5 at% relative to silicon of aluminum (metallic aluminum powder, 5 μm, 99.5%) or nitrogen (sodium nitrate, ≥99%), respectively. The silica-sol was allowed to gel at 60 °C in a sealed container for about 12 h, leading to formation of an amber lyogel, and by drying in an open container at 150 °C for 48 h to get a black xerogel. Next, the precursor was annealed at 1000 °C for 3.5 h under argon gas flow, during which left organic degradation products of the former sucrose get carbonized and vitrification of the silicate gel is completed. To convert that gained carbon-rich silicate glass into silicon carbide, the precursor was sintered at 1800 °C in argon atmosphere for 15 min in an induction furnace. Some nitrogen-doped samples were subsequently annealed in oxygen atmosphere at 1000 °C for 10 min to demonstrate oxidation effects.

2.2. Characterization

Imaging on the SiC crystals was performed via scanning electron microscopy (SEM) (Zeiss DSM 982 Gemini). The microscope was equipped with a thermal field emission gun as source and an Everhart Thornley Detector. Secondary electron images were recorded with an acceleration voltage of 10 keV. The structure was investigated by X-ray diffraction (XRD) using a Siemens D 501 diffractometer in Bragg-Brentano geometry operated at 40 kV and 30 mA using Cu K_α radiation and a graphite monochromator at the secondary side. The XRD data were refined by Rietveld analysis for phase fractions and lattice parameters (Bruker AXS, Topas Version 3.0). Qualitative phase analysis was performed on basis of PDF-2. XPS was performed with a monochromatic Thermo Fisher K-Alpha spectrometer equipped with an Al X-ray source (1486.6 eV) operating at a base pressure in the range of 10^{-8} to 10^{-10} mbar. High resolution scans were acquired at a pass energy of 50 eV and a step size (resolution) of 0.1 eV. Survey scans were acquired with a pass energy of 200 eV and a step size of 1.0 eV. The instrument work function was calibrated to give a binding energy (BE) of 83.96 eV for the Au $4f_{7/2}$ line for metallic gold. All measurements were performed at room temperature. The peaks were fitted utilizing Gaussian/Lorentzian mixed functions employing a linear background correction (program XPSPEAK41). Absorption infrared spectroscopy (RAIRS) was used to obtain electronic and chemical material information. A detailed description of the set-up and measurement procedure used for performing reflection measurements can be found elsewhere.[30] In short, the spectra were recorded utilizing a reflection unit with variable angle and a motorized polarizer (Bruker Optics). The measurements were performed with an incidence angle of 74° under vacuum with a base pressure of about 4 mbar. A correction for the substrate absorption (indium foil) was done for the recorded spectra.

© 2018 WILEY-VCH Verlag GmbH & Co. KGaA, Weinheim

ADVANCED SCIENCE NEWS
www.advancedsciencenews.com

ADVANCED ENGINEERING MATERIALS
www.aem-journal.com

3. Results

3.1. Structural Analysis

Appearance and morphology of the nitrogen- (SiC:N) and aluminum-doped SiC (SiC:Al) powder samples were investigated by SEM. The easiest obtainable form of sol-gel derived SiC (beside fibers, thin films, and porous structures) are microcrystals. **Figure 1** shows two examples of microcrystalline samples of SiC:N (a) and SiC:Al (b). Optical microscopy images of the samples (not shown) show SiC:N microcrystals in their typical green color, while SiC:Al microcrystals appear dark blue. One of the most obvious features of the crystals of SiC:N are the triangular shaped facets, originating from the truncated tetrahedron, typical and characteristic for the zinc blende structure of the cubic SiC polytype 3C–SiC. In comparison, the SiC:Al sample is dominated by hexagonal facets of rather flat crystals, which cannot be clearly assigned to a certain polytype merely from the image. They might still be truncated tetrahedra of different tracht and habit, therefore showing full hexagonal instead of triangular faces and flattened shape. It is another possibility that these are hexagonal flat crystals, which are typical for the so-called Lely platelets of the hexagonal polytype 6H–SiC.

A clear identification and distinction of polytypes in the two doped microcrystalline samples can be obtained by XRD powder diffraction. The XRD patterns of equally derived SiC:N and SiC:Al microcrystalline powders are shown in **Figure 2**a and b, respectively. In the displayed angular range both, the SiC:N (a) and SiC:Al (b) patterns show common most prominent peaks at 35.7°, 41.5°, 60.1°, 71.8°, and 75.6°. The according lattice constants were calculated to $d_{111} = 2.51$ Å, $d_{200} = 2.18$ Å, $d_{220} = 1.54$ Å, $d_{311} = 1.31$ Å, and $d_{222} = 1.26$ Å, respectively. These are in good agreement with literature values for 3C-SiC and can be assigned to its (111), (200), (220), (311), and (222) crystal planes.[31] Further, the 3C–SiC (111) diffraction peak shows two satellites at 34.2° and 38.2° for both samples. With their calculated lattice constants of $d_{101} = 2.62$ Å and $d_{103} = 2.36$ Å, they have been identified as the (101) and (103) crystal planes of the 6H–SiC polytype. Thereby the intensity of the satellites in comparison to the 3C–SiC (111) is less intense for SiC:N than for SiC:Al, which could indicate a larger contribution of the 6H–SiC polytype in the SiC:Al sample. The XRD pattern of SiC:N shows further minor peaks, of which all but one could be assigned to 6H–SiC. This confirms that the cubic polytype 3C–SiC and a minor portion of the hexagonal 6H–SiC polytype, dominate the phase composition of the nitrogen-doped SiC microcrystals (Figure 2a). No contributions of SiO_2 or foreign species such as silicon nitride were found. In comparison, the pattern for the aluminum-doped SiC microcrystals (Figure 2b) is slightly more complex. Here, the 3C–SiC phase is still the most prominent one, according to their peak intensity, but overlaid with a large number of further diffraction peaks. Part of them are the aforementioned 6H-SiC satellites at 34.2° and 38.2°, along with the additional minor signals of 6H–SiC, which in general show higher intensity than for the ones in the SiC:N powder. Two small shoulders to the 6H–SiC peaks appearing in both sample patterns at 37.7° and 64.7 °C are caused by negligible contributions of the polytype 15R–SiC. The additional diffraction peaks, which are not present for SiC:N, have been assigned to the hexagonal polytype 4H-SiC. It should be noted that the peak at 26.6° is a SiO_2 contribution (quartz (011)), does not originate from of the actual sample (as confirmed by FTIR and XPS) but is an external contamination with agate. No foreign impurities such as aluminum oxide have been found. These structural results indicate that the SiC:Al samples exhibit a different polytype composition than SiC:N despite identical preparation conditions besides the dopant.

For a distinct quantitative analysis of the phase-composition of the samples, Rietveld refinement on the respective XRD patterns has been performed to obtain the dopant-dependent unit cell dimensions and the crystallite sizes of certain polytype phases.[32,33] The obtained values are summarized in **Table 1** and **2** for SiC:N and SiC:Al, respectively. The detailed comparison of the observed pattern with the data gained from Rietveld analysis and their differential-plots can be found in the supplementary information. According to Rietveld refinement, the SiC:N powder consists of 93% of the cubic 3C–SiC polytype and 7% of the hexagonal 6H–SiC. The peaks belonging to 3C–SiC are sharp and can be fitted to crystal sizes larger than 200 nm. The peaks assigned to the 6H–SiC are broadened, leading to calculated crystal sizes of around 30 nm. There is no indication of other polytypes in the SiC:N sample according to Rietveld refinement. In comparison, the evaluation of data collected from the SiC:Al microcrystalline powder revealed a phase-composition of about 53% 3C–SiC, 37% 6H–SiC, and 10% 4H–SiC polytype. In this case, 3C–SiC and 6H–SiC both, gave particle sizes larger than 100 nm, while the line broadening of

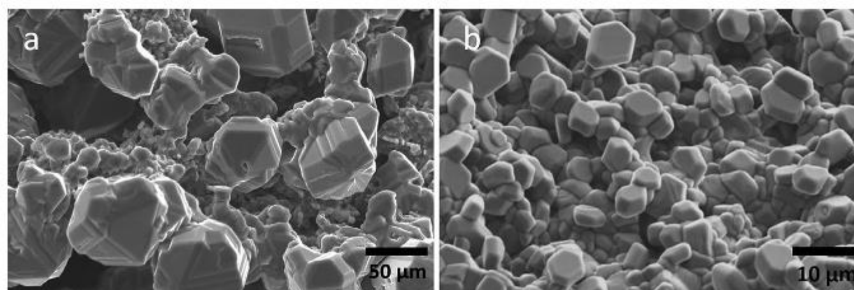

Figure 1. SEM images of doped silicon carbide microcrystals as derived from the sol-gel based precursor after carbothermal reduction for a nitrogen- a) and aluminum-doped SiC sample b).

 © 2018 WILEY-VCH Verlag GmbH & Co. KGaA, Weinheim

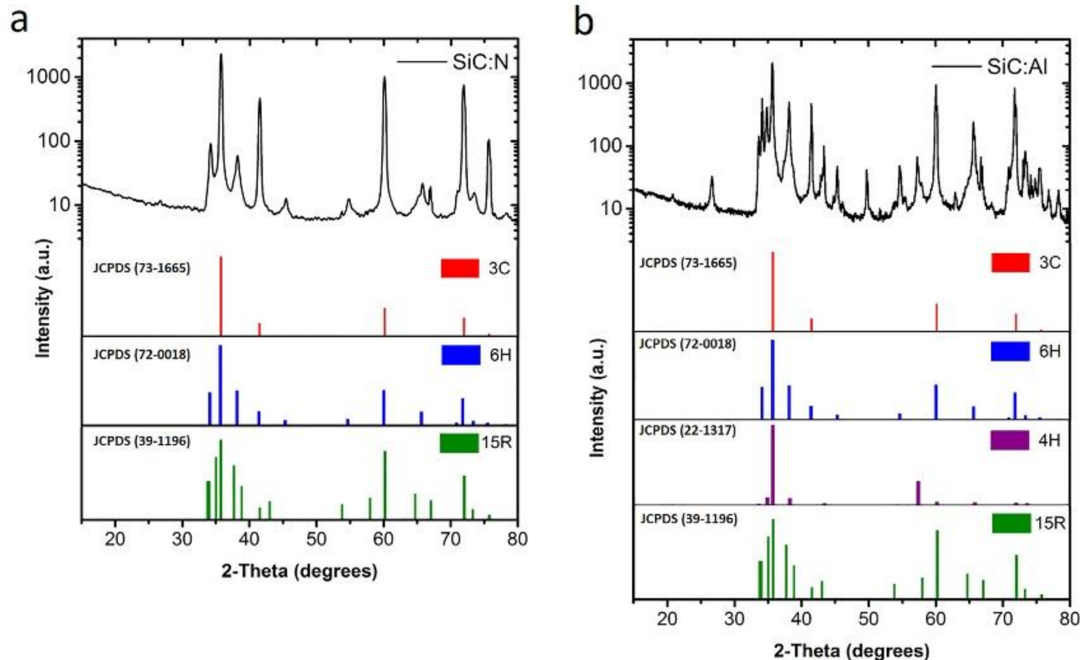

Figure 2. X-ray diffraction patterns of pristine nitrogen-doped SiC powder a) and aluminum-doped SiC powder b) in comparison with the reference pattern of the different SiC polytypes 3C (red bars, JCPDS 73–1665), 6H (blue bars, JCPDS 72–0018), 4H (purple bars, JCPDS 22–1317) and 15R (green bars, JCPDS 39–1196). (Note: The peak at 66.9° is a machine-related artefact, the peak at 26.6° is a preparation-induced agate contamination).

peaks related to 4H-SiC indicate smaller particle sizes of around 30 nm. This confirms first indications from SEM imaging that SiC:N indeed is dominated by the cubic 3C–SiC polytype of relatively large sizes, while the smaller particles can be assigned to the hexagonal 6H–SiC minority. The SiC:Al on the other hand has large contributions of both, the cubic 3C–SiC and the hexagonal 6H–SiC polytype with intermediate crystal sizes, while here a minority of small particles of another hexagonal polytype 4H–SiC have formed. A reason for the difference in polytype formation despite identical synthesis parameters must be related to the presence of the dopant. Thereby the effect of the dopant on polytype formation can have a kinetic as well as a chemical origin, as it was shown by Jepps et al. that nitrogen as impurity promotes the growth of 3C–SiC.[10] Aluminum, in contrast, tends to stabilize the hexagonal modifications.[34]

The unit cell data (axial length a for cubic, basal axial length a, and height c for hexagonal unit cells) of each polytype fraction of the SiC:N and SiC:Al samples were derived by Rietveld refinement and are also presented in Table 1 and 2, respectively. The value for the lattice constant of nominally undoped 3C–SiC at room temperature is specified with $a_{3C-SiC} = 4.3596$ Å,[35] which is in good agreement with the obtained unit cell data for the cubic component of SiC:N with $a_{3C\text{-}SiC:N} = (4.359 \pm 0.005)$ Å, and SiC:Al with $a_{3C\text{-}SiC:Al} = (4.36 \pm 0.01)$ Å. Regarding hexagonal contributions the polytypes 6H-SiC and 4H-SiC are significant for Rietveld refinement of the samples SiC:N (6H) and SiC:Al (6H, 4H). Thereby literature refers to lattice parameters of basal axis of $a_{6H\text{-}SiC} = 3.0806$ Å and height of $c_{6H\text{-}SiC} = 15.1173$ Å for nominally undoped 6H-SiC.[35] The calculated values for SiC:N are $a_{6H\text{-}SiC:N} = (3.081 \pm 0.005)$ Å and $c_{6H\text{-}SiC:N} = (15.118 \pm 0.005)$ Å, and for SiC:Al $a_{6H\text{-}SiC:Al} = (3.09 \pm 0.01)$ Å and height of $c_{6H\text{-}SiC:Al} = (15.13 \pm 0.01)$ Å, respectively. All parameters lie entirely within this range, merely the height of the 6H-SiC:Al unit cell appears to be slightly elongated, even with the considered deviation of the refinement. Reported unit cell dimensions for 4H-SiC are $a_{4H\text{-}SiC} = 3.0730$ Å for its axis and $c_{4H\text{-}SiC} = 10.0530$ Å for its height.[2] Rietveld refinement on the SiC:Al here led to $a_{4H\text{-}SiC:Al} = (3.08 \pm 0.01)$ Å and height of $c_{4H\text{-}SiC:Al} = (10.10 \pm 0.01)$ Å, again in good agreement for the axis component, but a significant elongation of the height. Comparing these lattice parameters of sol-gel derived nitrogen- and aluminum-doped SiC with literature, it can be observed that the hexagonal unit cells for SiC:Al are slightly larger, while they are unchanged for the cubic component or nitrogen incorporation. The elongation of lattice parameters for hexagonal SiC:Al, which makes $\Delta c_{6H\text{-}SiC:Al} = (0.01 \pm 0.01)$ Å and $\Delta c_{4H\text{-}SiC:Al} = (0.05 \pm 0.01)$ Å can be explained by the larger covalent radius of the Al atom (1.18 Å), which resides on a silicon-position (Si covalent radius 1.11 Å) in the lattice, which has been proven by Li et al. for 4H–SiC.[36] Nitrogen, which resides at carbon sites,[37] has a slightly smaller covalent radius of 0.75 Å, compared to carbon

Table 1. Phase composition, unit cell dimensions and crystallite sizes determined by Rietveld for a nitrogen-doped SiC powder.

SiC Polytype	Composition [%]	a [Å]	c [Å]	Particle size [nm]
3C	93	4.3585	–	200
6H	7	3.0807	15.1174	30

 © 2018 WILEY-VCH Verlag GmbH & Co. KGaA, Weinheim

ADVANCED SCIENCE NEWS
www.advancedsciencenews.com
ADVANCED ENGINEERING MATERIALS
www.aem-journal.com

Table 2. Phase composition, unit cell dimensions and crystallite sizes determined by Rietveld for an aluminum-doped powder.

SiC Polytype	Composition [%]	a [Å]	c [Å]	Particle size [nm]
3C	53	4.3603	–	100
6H	37	3.0817	15.1275	100
4H	10	3.0800	10.0980	30

with 0.77 Å, but does not lead to significantly changed unit cell dimensions in this case.[38]

3.2. Surface Composition

Surface chemistry of the differently doped sol-gel derived SiC powders was investigated via XPS to identify any connections between the surface termination and the incorporated dopant, in particular the effect on native oxide formation. Therefore the silicon Si 2p and carbon C 1s core level spectra were utilized to distinguish different silicon and carbon species in the samples and are shown in **Figure 3**. A comparison of the Si 2p core level spectra of SiC:N (top) and SiC:Al microcrystalline powder (bottom) is shown in Figure 3a. The Si 2p spectra can be deconvoluted into peaks arising from the different oxidation states of silicon Si^0, Si^{1+}, Si^{2+}, Si^{3+}, and Si^{4+},[39] which are located at different binding energies, thus allow identification of chemical bonds and make deductions of related compounds. In the present case, the Si 2p spectrum of SiC:N shows only two distinct peaks, one at a binding energy of 103.7 eV and another at 100.8 eV, whereas the latter has considerably higher intensity. While the low-energy signal can be assigned to the Si^+ state in SiC,[40] the other at higher energy arises from Si^{4+} in SiO_2,[41–43] indicating the presence of a significant native surface oxide layer on the SiC:N microcrystals.

In comparison, the Si 2p core level spectrum of the SiC:Al microcrystals shows merely one dominant peak at a binding energy of 99.7 eV with a tail toward the high-energy side. The strong peak can be assigned to Si^0, which originates either from Si-Si bonds in bulk silicon,[44,45] or from Si–H bonds, as typically observed for hydrogenated SiC at this energy.[46–48] The tail originates from a quite weak underlying peak centered at 101.3 eV, which can be assigned to a shifted Si^+ signal from SiC or a Si^{2+} contribution originating from an imperfect sub-oxide layer (SiO_x with $0 < x < 2$) or a combination of both.[39,49] There are no signs of a native oxide layer on the surface of the SiC:Al crystallites.

The C 1s core level spectra of SiC:N (top) and SiC:Al (bottom) microcrystalline powders are shown in Figure 3b. The SiC:N spectrum exhibits an asymmetric line feature built by two underlying peaks, a strong one located at 282.9 eV and a minor one at 284.8 eV. The low-energy peak at 282.9 eV can be clearly identified as originating from the C–Si bond of silicon carbide.[43,50] The less intense peak at 284.8 eV can roughly be assigned to some kind of C–C bond, but the exact origin is unclear.[50] In literature, C 1s peaks occurring at 285.0 ± 0.4 eV have been discussed related to various origins,[51] such as diamond-like sp^3 carbon (285.0 eV),[52] graphitic sp^2 carbon (284.6 eV),[53] adventitious carbon (285.1 eV) from organic post-fabrication deposites,[54] or mixed sp^2/sp^3 phases.[55] Estrade-Szwarckopf investigated asymmetric C 1s features, where a broad peak occurred, shifted against the graphitic sp^2 peak with its intensity varying with the treatment of the sample and referred to this broad 285 eV peak as "defect carbon".[56] Also Emtsev et al. and Rani et al. found such a broad C 1s peak close to 285 eV when investigating graphene grown epitaxially onto SiC or Gold, respectively, and also

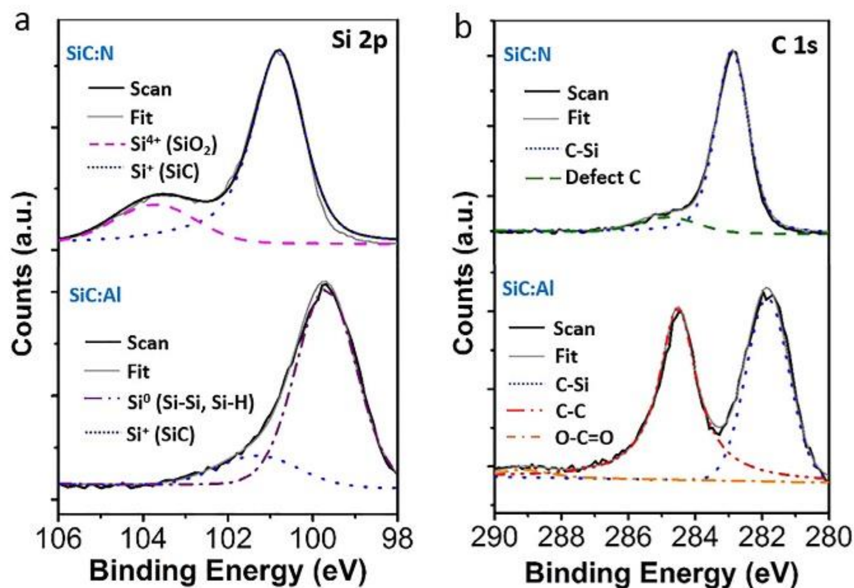

Figure 3. XPS spectra (solid line) for Si 2p core level a) and C 1s core level b) with simulated peak deconvolution of the components (broken lines) for SiC:N (top) and pristine SiC:Al (bottom) microcrystalline powders. For better visibility, spectra have been normalized.

© 2018 WILEY-VCH Verlag GmbH & Co. KGaA, Weinheim

ADVANCED SCIENCE NEWS
www.advancedsciencenews.com
ADVANCED ENGINEERING MATERIALS
www.aem-journal.com

ascribed it to sp^2 defects at the graphene-substrate interface.[57,58] Finally, Iwanowski et al. suggested carbonaceous surface exclusions from a carbon-saturated cubic silicon carbide ($Si_{1-x}C_x$ with $x > 0.54$) crystal lattice, being responsible for the observed 285 eV peak.[59] In the present C 1s spectra for SiC:N, the small signal intensity of that peak makes surface sp^2, sp^3 or mixed carbons rather unlikely as origin, and also adventitious carbons can be excluded in absence of exposure to organics between high-temperature synthesis and characterization. Therefore, here it is suggested that the observed 284.8 eV feature is related to buried defect C–C bonds at the interface between the SiC and the native silicon oxide layer.[60]

The C 1s spectrum of the SiC:Al microcrystalline powder indicates at first glance a completely different surface composition in comparison to SiC:N. The spectrum can be deconvoluted into two almost equally strong peaks at 281.9 and 284.5 eV and a very weak one at 289.1 eV. The most intense feature, arising at 281.9 eV, was attributed to C–Si bonding in silicon carbide.[44] Its significant shift in binding energy compared to SiC:N can be ascribed to the notably different sample composition, because binding energies are known to shift with the polytype.[59] The slightly less intense peak with its maximum at 284.5 eV was clearly identified as C–C bonding of graphitic surface carbon.[61] The weak signal at 289.1 eV was ascribed to O–C = O bonding, suggesting the formation of minor carbonates on the surface.[62] These results indicate that the surface structure of the SiC:Al crystallites is composed of a hydrogenated silicon interface buried under a graphene surface layer, similar to what has been reported by Pallechi et al.[63] Thereby the thickness of the graphene layer can be estimated from the intensity ratio between the carbide and graphitic peak to be nominally between one and two monolayers.[64] The very small carbonate signal suggests that the $Al_2(CO_3)_3$ is merely present as a small density of distributed "defect-like" sites below or above the carbon surface.

3.3. Bulk Properties

The RAIRS spectra of SiC:N and SiC:Al microcrystals are illustrated in **Figure 4**. Both samples clearly show a strong peak between 750 and 1000 cm^{-1}, which is referred to as the "*reststrahlen band*", a typical feature arising from the phonon-polariton resonance of bulk SiC. This peak generally dominates spectra recorded from SiC and is caused by vibrations of the Si- and C-sublattices against each other.[65] The tail of the phonon band toward higher wavenumbers for SiC:N is an effect that originates from high dopant concentration.[66] The unusual sharpness of the peak compared to the rather broad reststrahlen band usually seen for SiC single crystal wafers is a result of the present microcrystalline morphology of the material. Narrowing of the reststrahlen band has been reported for porous structures and powders and assigned to an increase in surface area.[26] On the high wavenumber side, where SiC:Al shows no further features, SiC:N exhibits an additional absorption band at about 1110 cm^{-1}. This peak can be assigned to Si–O–Si vibrations of SiO_2.[67] This peak is superposed with a very broad absorption in the region between 2350 and 970 cm^{-1}. The latter is a result of plasmon-phonon interactions, which occur when plasmon and phonon modes appear in a similar frequency range.[65] The

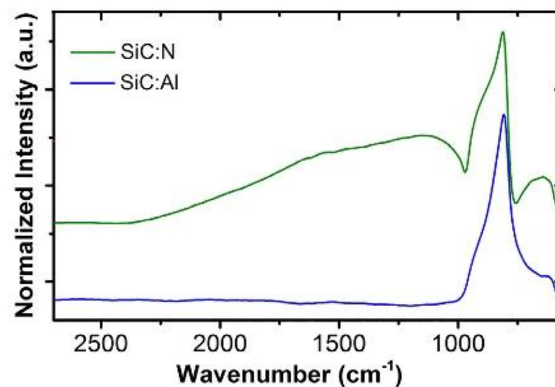

Figure 4. Infrared reflection absorption (RAIRS) spectra of SiC:N (top curve) and SiC:Al (bottom curve) microcrystalline powders. For better comparability, spectra have been normalized.

plasma frequency of undoped SiC lies typically in the microwave range, but strongly depends on charge carrier concentration, effective electron mass and the electron mobility. Here, the shift to higher energies emerges from large charge carrier concentration, which was found to be $N_D–N_A = 2.1 \cdot 10^{19}\,cm^{-3}$ from Hall-measurements on this synthesized material.[17] The small absorption peak at about 640 cm^{-1} for SiC:N can be attributed to the coupling of the longitudinal optical phonon to the plasmon.[65] The absence of both these features in SiC:Al is caused by its considerably lower charge carrier concentration from p-doping, which was found to be merely $N_D–N_A = -6.8 \cdot 10^{11}\,cm^{-3}$.[68] The absence of the 1110 cm^{-1} oxide peak in the spectrum of the SiC:Al is in good agreement with the XPS results, which is showing no silicon oxide present on the surface. The absence of a carbonate contribution in spectrum is not surprising because it appeared only in trace amounts on the surface, and undetectable for rather bulk sensitive IR measurements.

4. Discussion

While the incorporation of a nitrogen dopant with this SiC synthesis method results in SiC:N microcrystals exhibiting typical common surface composition of SiC with a native oxide (SiO_2) layer and some imperfect graphite species, the equivalent incorporation of aluminum in the process leads to a very different surface composition. The SiC:Al exhibits apparently a quite stable hydrogen-terminated surface (Si–H), most likely buried under a graphene mono- or bilayer surface, while oxygen is merely found bound in a very small density of aluminum carbonate sites near the surface. These seem to cause a self-passivation effect on the SiC:Al crystallites and hinder formation of a native oxide layer. Hydrogen is known to saturate dangling bonds in semiconductors, especially in silicon, but also in SiC and therewith deactivating potential luminescence quenching or charge trapping sites.[29] The presence of a high density of Si–H bonds and absence of a Si-dangling bond signal (BE < 99 eV) for SiC:Al here, indicates successful deactivation of these defects. Further, the carbonate layer, despite having less than nominally

 © 2018 WILEY-VCH Verlag GmbH & Co. KGaA, Weinheim

ADVANCED SCIENCE NEWS
www.advancedsciencenews.com
ADVANCED ENGINEERING MATERIALS
www.aem-journal.com

1 nm thickness judged by the intensity of the signal, seems to have passivated the SiC surface against the typical formation of silicon oxide at exposure to air. Potential reasons for this different surface composition of the present SiC:Al lay in the fact that during this "one-pot synthesis" and in particular during the final annealing step, all chemical components are enclosed in the reaction chamber volume. The carbothermal reduction of silicon species in the precursor and formation of SiC occurs merely at temperatures $> 1700\,°C$, following the reaction SiO_2 (s) + 3C (s) → SiC (s) + 2CO (g). This happens in two ways: (1) directly reacting with solid carbon via SiO_2 (s) + C (s) → SiO (g) + CO (g), and SiO (g) + 2C (s) → SiC (s) + CO (g), and (2) indirectly by reaction with CO via SiO_2 (s) + CO (g) → SiO (g) + CO_2 (g) and SiO (g) + 3CO (g) → SiC (s) + $2CO_2$ (g). As also the aluminum compounds go into the gas phase during this process, where some aluminum is built into the SiC lattice as dopant, also secondary chemical reactions between Al and CO/CO_2 are likely. It is suggested that here aluminum carbonate is formed at the surface of the SiC crystals during the cooling below 1700 °C, when silicon species are no longer in a stable gas phase nor reacting with C or CO. Three scenarios are imaginable for their formation: 1) Few separated near-surface aluminum sites in the SiC lattice react with the CO/CO_2 gas; 2) remaining gaseous aluminum species condensate on the SiC surface and subsequently react with surface carbon or the CO/CO_2 gas; 3) gaseous aluminum species react in the gas phase with CO/CO_2 and subsequently condensate on the SiC surface. However, since aluminum carbonate $Al_2(CO_3)_3$ is known not to be environmentally stable, thus would have been decomposed to $Al(OH)_3$ by the time of measurement. Therefore it is assumed that the carbonate sites are also buried underneath the graphene surface layer, which stabilizes them. No other aluminum species like Al_2O_3 or $Al(OH)_3$ were found. This was also confirmed by FTIR, which also proves the absence of SiO_2 in the SiC:Al sample and further demonstrates the typical difference in charge carrier concentration between the n- and p-doped SiC by the appearance of the plasmon-phonon interaction. The observed formation of different polytypes, triggered by the incorporated dopant and also the different sizes of the according crystallites, allows certain speculations about the role of the dopant in the crystal growth process. The dopant might be acting "only" as a catalyst or by its displacement of carbon or silicon in the lattice, leading to changes of the unit cell size and thus giving preference to certain polytype formation. The role of the dopant as chemical pathway with strong impact on the final polytype has also been discussed by Ariyawong et al.,[69] who addressed the link between the crystal chemistry and growth process parameters. Therein SiC is treated as a solid solution and the polytypes evaluated in terms of their respective C and Si activities. They found that 3C–SiC is always obtained with high Si activity in SiC, that is, close to the SiC–Si two-phase boundary. In the present case, the dominant polytype for SiC:N is 3C–SiC and the crystals are oxidized on the surface. With Al incorporation in SiC:Al, the hexagonality increases and the SiC surface is not oxidized. Therefore, it could be considered that the reducing conditions on SiC by Al might increase the C activity in the crystals, thus promoting formation of the hexagonal polytypes.

Most important in terms of usability of this material in electrochemical and (opto)electronic applications is clearly the role of aluminum for self-passivation of the as-formed crystals, protecting from oxidation and most likely deactivation of surface defects by saturation with hydrogen. The deactivation of dangling bonds and prevention of insulating oxide layers is vital for efficient charge transfer and transport in this material, for example, in LEDs or catalysis. This sort of surface passivation is usually only achieved by post-treatment such as alumina or titania deposition on freshly HF-etched SiC surfaces.[29] In contrast, our synthesis route via sol-gel precursors and carbothermal reduction allows to obtain SiC growth, doping, and surface passivation as a one-step process.

5. Conclusions

In summary, nitrogen- and aluminum-doped SiC microcrystalline powders have been synthesized from sol-gel based precursors after carbothermal reduction and have been investigated regarding the effect on surface properties and structural changes triggered by the incorporated dopant. Therefore SEM, XRD, XPS, and RAIRS were used to gain knowledge about the polytype composition, crystallite size, unit cell size, bulk chemistry, and surface chemistry.

It was revealed that SiC:N consists mostly of the cubic polytype 3C–SiC, while SiC:Al is divided into 50% 3C–SiC and 50% hexagonal polytypes 6H–SiC and 4H–SiC. This might be caused either by catalytic properties of the aluminum, promoting formation of the more energy expensive formation of hexagonal phase, or triggered by the change in unit cell size, which decreases where the smaller nitrogen atom replaces carbon and increases where the larger aluminum atom replaces silicon. Independent from this bulk effect, also the surface composition of the two materials is very different. While the nitrogen dopant leads to formation of SiC:N microcrystals with a typical SiO_2 surface layer, the equivalent incorporation of aluminum generates SiC:Al crystallites with a surface of hydrogenated silicon bonds and a small density of aluminum carbonate sites buried under a graphene layer. This leads to two valuable effects for SiC: deactivated defect sites by hydrogen saturation of dangling bonds and passivation of the crystallites surface to prevent formation of a native oxide.

The SiC:N instead exhibits no signs of hydrogenation and no graphitic carbon, but the commonly seen native oxide layer, where dangling bonds are saturated by unfavorable oxygen. This difference between SiC:N and SiC:Al might be caused by the high reactivity of aluminum and the longer stability of gaseous aluminum species after SiC formation at the end of the high-temperature process, leading to the natural formation of a passivation layer on the SiC crystallites directly after growth. The nature of this passivation layer appeared as a carbonate feature in XPS, which for aluminum is known to be unstable in air. Therefore it is suggested that the carbonate is formed at the interface between the SiC and the graphene surface, which stabilizes it. The fact that SiC growth, doping and surface passivation can be achieved in one step with our "one-pot synthesis" is a vital key for the application of such affordably prepared materials in applications involving surface-sensitive charge-transfer reactions. This is promising for its potential use in LEDs, photovoltaics, and catalysis.

© 2018 WILEY-VCH Verlag GmbH & Co. KGaA, Weinheim

Acknowledgements

O. K. and B. F. are grateful to the Austrian Science Fund (FWF) for financial support under Project No. P 26968.

Supporting Information

Supporting information is available online from Wiley Online Library or from the author.

Conflict of Interest

The authors declare no conflict of interest.

Keywords

Self-passivation, silicon carbide, sol-gel processing, surface termination

Received: November 28, 2017
Revised: January 30, 2018
Published online: February 26, 2018

[1] E. G. Acheson, Production of artificial crystalline carbonaceous materials, carborundum. *British Pat. 17911*, **1892**.
[2] M. E. Levinshteĭn, S. L. Rumyantsev, M. Shur, *Properties of Advanced Semiconductor Materials: GaN, AlN, InN, BN, SiC, SiGe*, Wiley, New York **2001**.
[3] S. Prochazka, Hot pressed silicon carbide. *US Pat. US3853566*, **1974**.
[4] F. Mubarok, N. Espallargas, *J. Therm. Spray Technol.* **2015**, *24*, 817.
[5] K. Miyoshi, D. H. Buckley, *Wear* **1982**, *75*, 253.
[6] J. Rabkowski, D. Peftitsis, H. Nee, *EEE Ind. Electron. Mag.* **2012**, *6*, 17.
[7] A. Elasser, M. H. Kheraluwala, M. Ghezzo, R. L. Steigerwald, N. A. Evers, J. Kretchmer, T. P. Chow, *IEEE Trans. Ind. Appl.* **2003**, *39*, 915.
[8] R. Dietmueller, H. Nesswetter, S. J. Schoell, I. D. Sharp, M. Stutzmann, *ACS Appl. Mater. Interfaces* **2011**, *3*, 4286.
[9] S. E. Saddow, F. La Via (Eds.), *Advanced Silicon Carbide Devices and Processing*, InTech, Rijeka, Croatia **2015**.
[10] N. W. Jepps, T. F. Page, *Prog. Cryst. Growth Charact.* **1983**, *7*, 259.
[11] S. Müller, R. C. Glass, H. M. Hobgood, V. F. Tsvetkov, M. Brady, D. Henshall, J. Jenny, D. Malta, C. H. Carter, *J. Cryst. Growth* **2000**, *211*, 325.
[12] P. Deák, B. Aradi, A. Gali, U. Gerstmann, *Phys. Status Solidi (B)* **2003**, *235*, 139.
[13] Y. Hattori, T. Suzuki, T. Murata, T. Yabumi, K. Yasuda, M. Saji, *J. Cryst. Growth* **1991**, *115*, 607.
[14] D. L. Smith, Includes index, *Thin Film Deposition and Applications*, McGraw-Hill, New York **1995**.
[15] M. Helgesen, R. Søndergaard, F. C. Krebs, *J. Mater. Chem.* **2010**, *20*, 36.
[16] S. Greulich-Weber, B. Friedel, *MSF* **2009**, *615–617*, 637.
[17] B. Friedel, S. Greulich-Weber, *MRS Proc.* **2006**, *963*, 0963-Q15-10.
[18] B. Friedel, S. Greulich-Weber, *MSF* **2006**, *527–529*, 759.
[19] A. Konopka, B. Aşik, U. Gerstmann, E. Rauls, N. J. Vollmers, M. Rohrmüller, W. G. Schmidt, B. Friedel, S. Greulich-Weber, *IOP Conf. Ser.: Mater. Sci. Eng.* **2010**, *15*, 12013.
[20] G. Chris, J. A. van de Walle, J. Neugebauer, *Nature* **2003**, *423*, 626.
[21] O. Kettner, C. E. Finlayson, B. Friedel, *Nanosci. Nanotechnol. Lett.* **2015**, *7*, 56.
[22] D. V. Talapin, J.-S. Lee, M. V. Kovalenko, E. V. Shevchenko, *Chem. Rev.* **2010**, *110*, 389.
[23] F. Gao, Z. Li, J. Wang, A. Rao, I. A. Howard, A. Abrusci, S. Massip, C. R. McNeill, N. C. Greenham, *ACS Nano* **2014**, *8*, 3213.
[24] K. M. Noone, S. Subramaniyan, Q. Zhang, G. Cao, S. A. Jenekhe, D. S. Ginger, *J. Phys. Chem. C* **2011**, *115*, 24403.
[25] J. Piris, N. Kopidakis, D. C. Olson, S. E. Shaheen, D. S. Ginley, G. Rumbles, *Adv. Funct. Mater.* **2007**, *17*, 3849.
[26] M. F. MacMillan, R. P. Devaty, W. J. Choyke, D. R. Goldstein, J. E. Spanier, A. D. Kurtz, *J. Appl. Phys.* **1996**, *80*, 2412.
[27] V. V. Afanasev, M. Bassler, G. Pensl, M. Schulz, *Phys. Status Solidi (A)* **1997**, *162*, 321.
[28] R. Kaplan, *Surf. Sci.* **1989**, *215*, 111.
[29] W. Lu, Y. Ou, E. M. Fiordaliso, Y. Iwasa, V. Jokubavicius, M. Syväjärvi, S. Kamiyama, P. M. Petersen, H. Ou, *Sci. Rep.* **2017**, *7*, 9798.
[30] M. Djak, E. Gilli, E. Kontturi, R. Schennach, *Macromolecules* **2011**, *44*, 1775.
[31] J. Ruska, L. J. Gauckler, J. Lorenz, H. U. Rexer, *J. Mater. Sci.* **1979**, *14*, 2013.
[32] H. M. Rietveld, *J. Appl. Crystallogr.* **1969**, *2*, 65.
[33] A. L. Ortiz, F. L. Cumbrera, F. Sánchez-Bajo, F. Guiberteau, H. Xu, N. P. Padture, *J. Am. Ceram. Soc.* **2000**, *83*, 2282.
[34] P. A. Kistler-De Coppi, W. Richarz, *Int. J. High Technol. Ceram.* **1986**, *2*, 99.
[35] A. Taylor, R. M. Jones, *Proc. Conf. Silicon Carbide* Pergamon Press, New York **1960**.
[36] Y. Li, J. Li, C. Chen, Z. Yang, Y. Yang, Z. Lin, *Appl. Surf. Sci.* **2012**, *259*, 21.
[37] S. Greulich-Weber, *Phys. Status Solidi (A)* **1997**, *162*, 95.
[38] B. Zhang, J. Li, J. Sun, S. Zhang, H. Zhai, Z. Du, *J. Eur. Ceram. Soc.* **2002**, *22*, 93.
[39] X. Y. Chen, Y. F. Lu, L. J. Tang, Y. H. Wu, B. J. Cho, X. J. Xu, J. R. Dong, W. D. Song, *J. Appl. Phys.* **2005**, *97*, 14913.
[40] T. Parrill, Y. Chung, *Surf. Sci.* **1991**, *243*, 96.
[41] A. Stoch, J. Stoch, A. Rakowska, *Surf. Interface Anal.* **1994**, *22*, 242.
[42] B. Herreros, T. L. Barr, P. J. Barrie, J. Klinowski, *J. Phys. Chem.* **1994**, *98*, 4570.
[43] A. A. Galuska, J. C. Uht, N. Marquez, *J. Vac. Sci. Technol. A: Vac., Surf., Films* **1988**, *6*, 110.
[44] I. Kusunoki, Y. Igari, *Appl. Surf. Sci.* **1992**, *59*, 95.
[45] S. A. Chambers, V. A. Loebs, *Phys. Rev. B* **1993**, *47*, 9513.
[46] M. M. Kamble, V. S. Waman, A. H. Mayabadi, S. S. Ghosh, B. B. Gabhale, S. R. Rondiya, A. V. Rokade, S. S. Khadtare, V. G. Sathe, T. Shripathi, H. M. Pathan, S. W. Gosavi, S. R. Jadkar, *J. Coat.* **2014**, *2014*, 1.
[47] T. Seyller, *J. Phys.: Condens. Matter* **2004**, *16*, S1755.
[48] S. Gallis, M. Huang, H. Efstathiadis, E. Eisenbraun, A. E. Kaloyeros, E. E. Nyein, U. Hommerich, *Appl. Phys. Lett.* **2005**, *87*, 91901.
[49] W. Zhang, S. Zhang, Y. Liu, T. Chen, *J. Cryst. Growth* **2009**, *311*, 1296.
[50] S. Contarini, S. P. Howlett, C. Rizzo, B. A. de Angelis, *Appl. Surf. Sci.* **1991**, *51*, 177.
[51] S.-H. Nam, M.-H. Kim, J.-S. Hyun, Y. D. Kim, J.-H. Boo, *J. Nanosci. Nanotechnol.* **2010**, *10*, 2741.
[52] F. Arezzo, N. Zacchetti, W. Zhu, *J. Appl. Phys.* **1994**, *75*, 5375.
[53] M. M. Waite, S. I. Shah, *Appl. Phys. Lett.* **1992**, *60*, 2344.
[54] S. J. Harris, A. M. Weiner, *Appl. Phys. Lett.* **1989**, *55*, 2179.
[55] J. C. Arnault, S. Saada, S. Delclos, L. Intiso, N. Tranchant, R. Polini, P. Bergonzo, *Diamond Relat. Mater.* **2007**, *16*, 690.
[56] H. Estrade-Szwarckopf, *Carbon* **2004**, *42*, 1713.
[57] K. V. Emtsev, F. Speck, T. Seyller, L. Ley, J. D. Riley, *Phys. Rev. B* **2008**, *77*, 155303.
[58] J. R. Rani, J. Lim, J. Oh, D. Kim, D. Lee, J.-W. Kim, H. S. Shin, J. H. Kim, S. C. Jun, *RSC Adv.* **2013**, *3*, 5926.

 © 2018 WILEY-VCH Verlag GmbH & Co. KGaA, Weinheim

ADVANCED SCIENCE NEWS
www.advancedsciencenews.com

ADVANCED ENGINEERING MATERIALS
www.aem-journal.com

[59] R. Iwanowski, K. Fronc, W. Paszkowicz, M. Heinonen, *J. Alloys Compd*. **1999**, *286*, 143.
[60] C. Önneby, C. G. Pantano, *J. Vac. Sci. Technol. A: Vac., Surf., Films* **1997**, *15*, 1597.
[61] H. Estrade-Szwarckopf, B. Rousseau, *J. Phys. Chem. Solids* **1992**, *53*, 419.
[62] W. Si, X. Wu, J. Zhou, F. Guo, S. Zhuo, H. Cui, W. Xing, *Nanoscale Res. Lett*. **2013**, *8*, 247.
[63] E. Pallecchi, F. Lafont, V. Cavaliere, F. Schopfer, D. Mailly, W. Poirier, A. Ouerghi, *Sci. Rep*. **2014**, *4*, 4558.
[64] M. H. Oliveira, T. Schumann, F. Fromm, R. Koch, M. Ostler, M. Ramsteiner, T. Seyller, J. M. J. Lopes, H. Riechert, *Carbon* **2013**, *52*, 83.
[65] H. Mutschke, A. C. Andersen, D. Clément, T. Henning, G. Peiter, *Astron. Astrophys*. **1999**, *345*, 187.
[66] R. T. Holm, P. H. Klein, P. E. R. Nordquist, *J. Appl. Phys*. **1986**, *60*, 1479.
[67] Z. An, R. K. Y. Fu, P. Chen, W. Liu, P. K. Chu, C. Lin, *J. Vac. Sci. Technol. B* **2003**, *21*, 1375.
[68] B. Friedel, *Doctoral Thesis*, University of Paderborn, **2007**.
[69] K. Ariyawong, C. Chatillon, E. Blanquet, J.-M. Dedulle, D. Chaussende, *CrystEngComm* **2016**, *18*, 2119.

 © 2018 WILEY-VCH Verlag GmbH & Co. KGaA, Weinheim

Supplementary Information

DOI: 10.1002/adem.((please add manuscript number))

Characterization of Surface and Structure of in-situ Doped Sol-Gel-Derived Silicon Carbide **

By *Olivia Kettner*, *Sanja Šimić*, *Birgit Kunert*, *Robert Schennach*, *Roland Resel*, *Thomas Grießer* and *Bettina Friedel**

[*] *Dr. B. Friedel*
illwerke vkw Endowed Professorship for Energy Efficiency, Energy Research Center, Vorarlberg University of Applied Sciences
6850 Dornbirn, Austria
E-mail: bettina.friedel@fhv.at
Dr. B Friedel, O. Kettner, B. Kunert, Prof. Dr. R. Schennach, Prof. Dr. R. Resel
Institute of Solid State Physics, Graz University of Technology
8010 Graz, Austria
S. Šimić
Graz Centre for Electron Microscopy (ZFE)
8010 Graz, Austria
Prof. Dr. T. Grießer
Institute of Chemistry of Polymeric Materials, Montanuniversität Leoben
8700 Leoben, Austria

S1. Rietveld Refinement of X-ray data for sol-gel derived doped 3C-SiC powders

Observed X-ray diffraction pattern and calculated data for the nitrogen and aluminum doped silicon carbide powder samples are illustrated in **Figure S1** and **Figure S2**, respectively. On the bottom of each figure the differential plots between the observed and calculated data are shown. The weighted residual error and expected error are R_{wp}=28.19 and R_{exp}=17.15 for SiC:N, and R_{wp}=33.55 and R_{exp}=15.86 for SiC:Al.

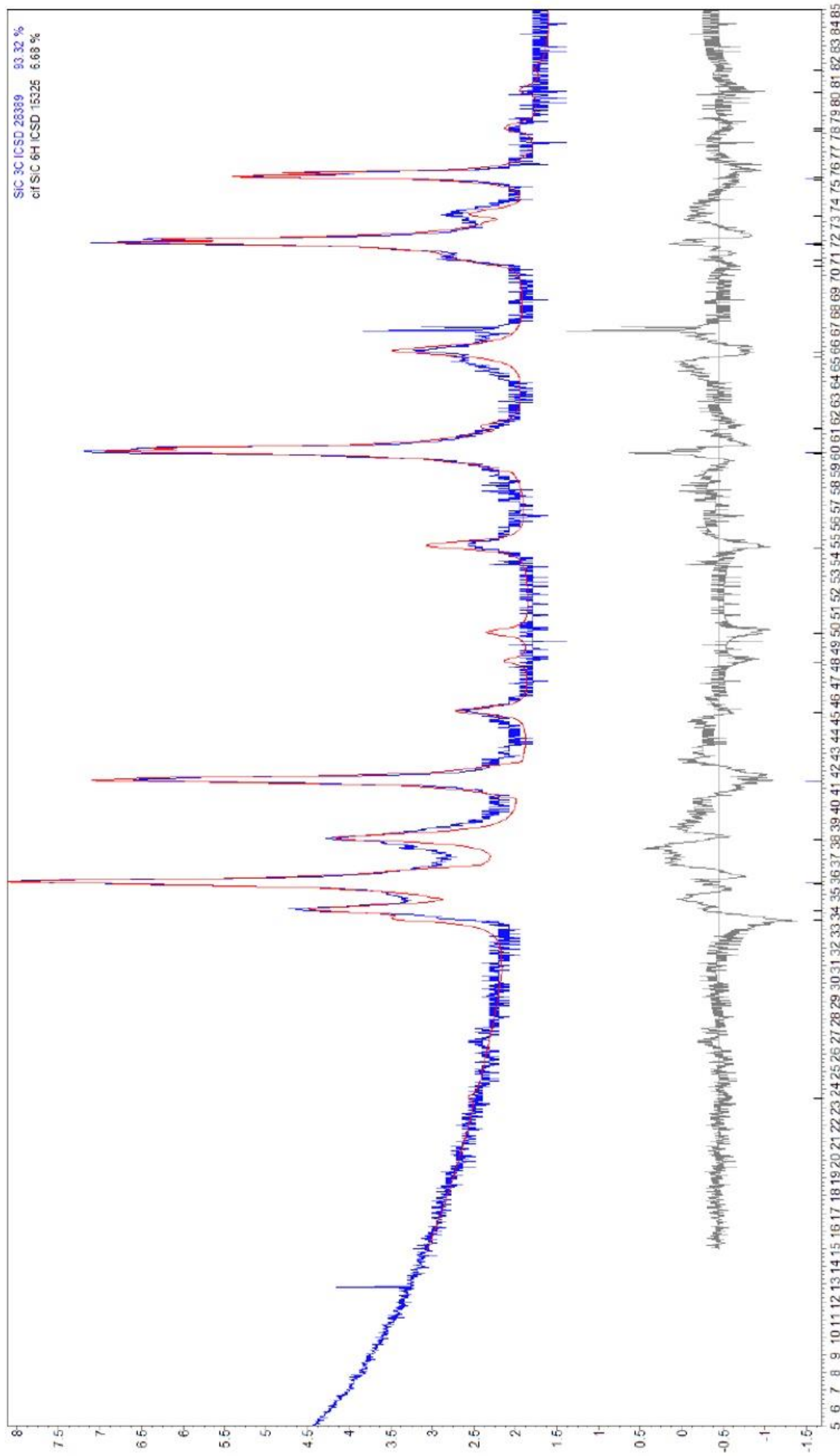

Fig. S1. Measured diffraction pattern, Rietveld refinement and difference function for the nitrogen-doped SiC-sample

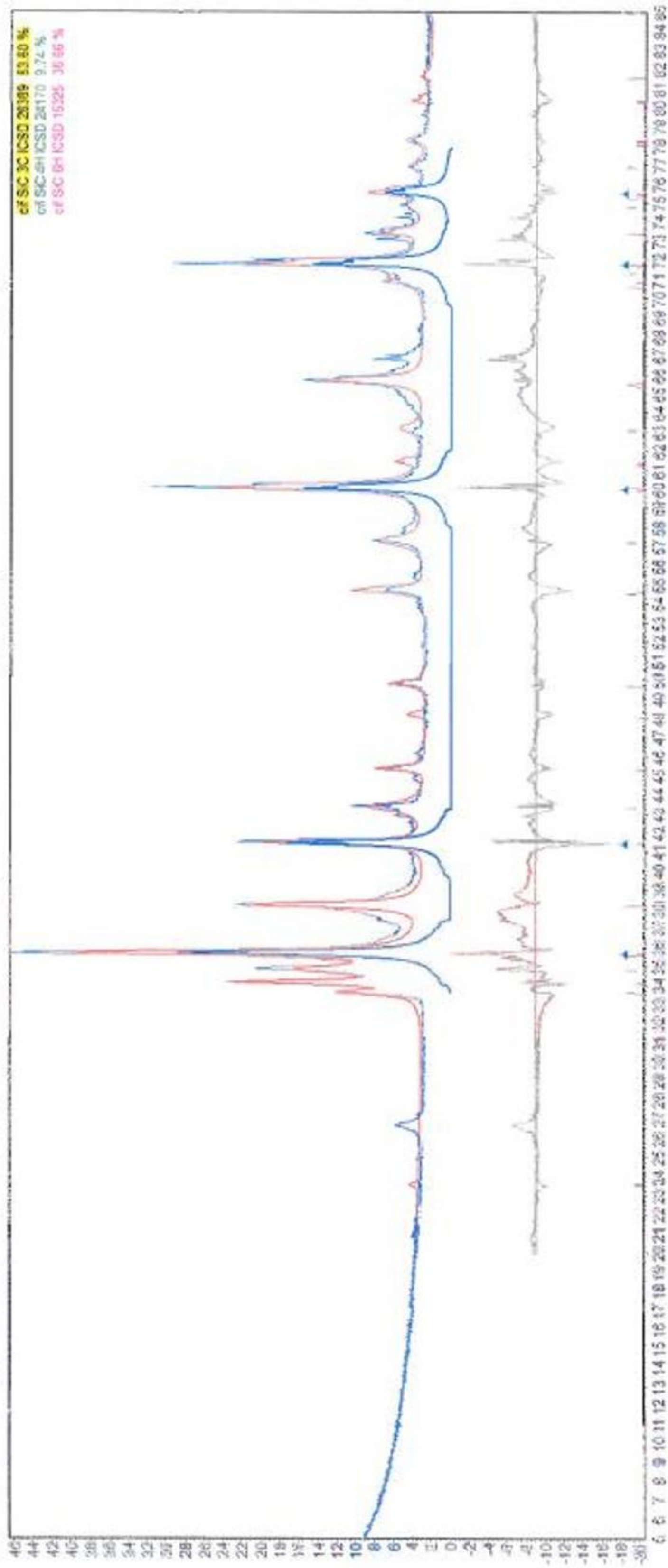

Fig. S2. Measured diffraction pattern, Rietveld refinement and difference function for the aluminum-doped SiC-sample.

3.2 Incorporation of Nitrogen-Doped SiC Nanocrystals in Organic Solar Cells

3.2.1 Introduction

One of the best investigated organic solar cell systems in the bulk heterojunction geometry is the system using P3HT as donor and $PC_{60}BM$ as acceptor material.[140–142] As mentioned in section 1.3.2.1, fullerene derivatives only contribute to light harvesting in the UV range. SiC offers better charge carrier mobilities than $PC_{60}BM$.[143,144] Furthermore, it is expected to be able to harvest light in the visible range, as additional states within its wide band-gap can be created by doping. Even though the energy levels of 3C-SiC and P3HT are staggered and match perfectly for application in organic inorganic hybrid solar cells, only very little can be found in the literature. A trial for incorporating SiC fibres was reported[145], no reports in literature of using SiC nanocrystals as acceptor or co-acceptor were found. Therefore, the goal presented in this chapter was to replace the $PC_{60}BM$ acceptor in steps of 20 wt.% by SiC:N nanocrystals and investigate the impact of this exchange on the performance of solar cells. This will allow novel insights into functionality of devices containing SiC nanocrystals. This way, a suitable organic/inorganic acceptor ratio in ternary blends can be determined or if it would be even possible to replace $PC_{60}BM$ by SiC:N as acceptor material, completely. The denotation of the samples and the according blend compositions of the thin films are listed in table 3.1. The all-organic binary devices (0 wt.% SiC) *b6* act as a reference.

Table 3.1.: Summary of the sample denotations and blend compositions.

Name	P3HT (mg/ml)	SiC:N (mg/ml)	$PC_{60}BM$ (mg/ml)	SiC fraction of acceptor (wt.%)
b1	18	18	0	100
b2	18	14.4	3.6	80
b3	18	10.8	7.2	60
b4	18	7.2	10.8	40
b5	18	3.6	14.4	20
b6	18	0	18	0

Within this chapter it will be demonstrated how incorporation of SiC as co-acceptor in P3HT:$PC_{60}BM$ blends can improve the device performance by investigating not only the photophysics and electrical characteristics, but also the blend morphology in terms of how and where in the thin films the inorganic crystallites tend to accumulate. The solar cell devices and samples used for photophysical investigations were obtained upon blending P3HT with SiC and/or $PC_{60}BM$ as described in chapter 2.1.2.

3.2.2 Incorporation of SiC Nano-Crystals in P3HT:$PC_{60}BM$ Blends

To ensure an as small as possible size distribution of the SiC nanocrystals, the as-synthesized material was dispersed in IPA and sonicated for 2 - 4 hours. The suspension was then left for at least four hours to allow the larger SiC crystallites to sediment and the smaller ones to form a colloidal solution. Afterwards, the supernatant final nanocrystal suspension was extracted and placed on a hot plate to evaporate the solvent. A SEM image of the obtained material is shown in figure 3.1. As can be seen, the shape of the crystallites exhibits a tetrahedral-like structure, which is an indication for the cubic polytype of SiC. The majority of particles are facetted crystals with a size of about 100 nm, but there are also aggregates of much smaller crystals with less than 10 nm.

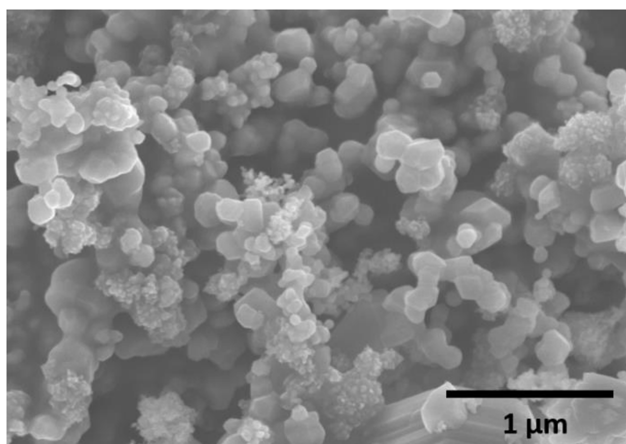

Figure 3.1: SEM image of SiC nano-crystallites after sedimentation separation.

To gain knowledge about the SiC distribution in the films and its agglomeration behaviour, an ultrathin lamella of an exemplary film sample of intermediate SiC concentration (*b4*, 40wt% SiC) was extracted perpendicular to the casting plane by a focused ion beam for electron microscopic and associated spectroscopic investigation. This should give insights not only in the vertical distribution of the three components present in the thin film, but also

in the functional morphology. Phase-separation is a critical point as domains with suitable sizes are beneficial for the exciton dissociation and charge transport and thus support a higher J_{SC} and therefore lead to a higher PCE. A HAADF STEM image of the lamella extracted from the *b4* film is illustrated in figure 3.2. on the left. This method allows to distinguish between different elements as the intensity depends on the atomic number Z, but it cannot provide contrast between the organic domains. Clusters of SiC particles are visible in light grey in the cross-sectional image, due to the strong mass thickness contrast, where the organic material appears in black. The SiC clusters with sizes of up to 300 nm tend to accumulate on top of the organic material, causing the layer thickness to locally exceed by far the desired 150 nm in those regions. This is an indication for a not completely homogeneous distribution of the inorganic particles within the organic matrix, which is also representative for other regions of this lamella and the other samples (not shown).

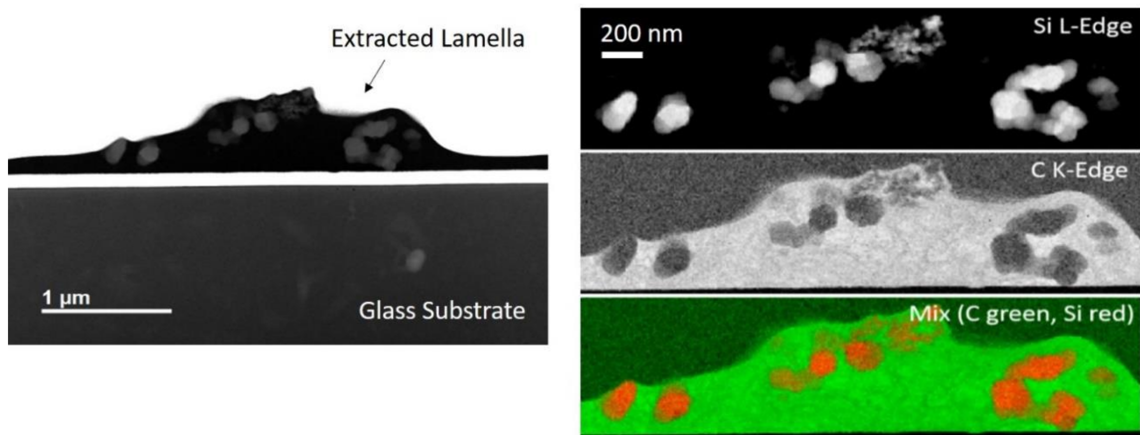

Figure 3.2.: HAADF STEM image (left) and elemental maps extracted from the EELS spectra of an exemplary region of a *b4* lamella (right).

Elemental maps were extracted from the EELS spectra, which were recorded from the same lamella from plasmon loss peaks at around 20 eV. In figure 3.2. on the right, the Si L-edge and C K-edge intensity maps are shown, with the bright areas representing the location of larger signal, and thus higher element concentration. A false-coloured combined map demonstrates where green areas are C-rich and red areas are Si-rich. The shift of the bulk plasmon peak can be used to visualize the SiC particles as well as to distinguish between the two organic constituents of the matrix. To have a closer look at the intermix of the three components, detailed images are depicted in figure 3.3., where SiC appears in blue, P3HT in red and orange and $PC_{60}BM$ in green. These coloured elemental maps were created by a

Gaussian fit of every pixel of the FWHM EELS images. The image on the left shows that the SiC agglomerations have a finer structure than first suggested by the STEM images, indicating a more sufficiently intermixed morphology on the nanoscale. This nanomorphology is expected to ensure that the majority of excitons is able to reach the D/A interface before recombination takes place. Looking in more detail at the elemental maps, it can be observed that the SiC clusters are preferentially surrounded by $PC_{60}BM$. In figure 3.3. on the right, an elemental map in higher resolution shows a SiC crystallite (in blue), with a size of about 60 nm and which is completely surrounded by $PC_{60}BM$ (in green). The well coverage of SiC by the $PC_{60}BM$ is essential for the charge transport. Inorganic materials tend to have surface defects which would trap generated electrons. A $PC_{60}BM$ layer around the particles can support faster detrapping or even avoid trapping of the charge carriers. This is also suggested to be beneficial for the charge carrier transport as it supports the formation percolated pathways of a combination of the two acceptor materials and the donor material to the respective electrodes.

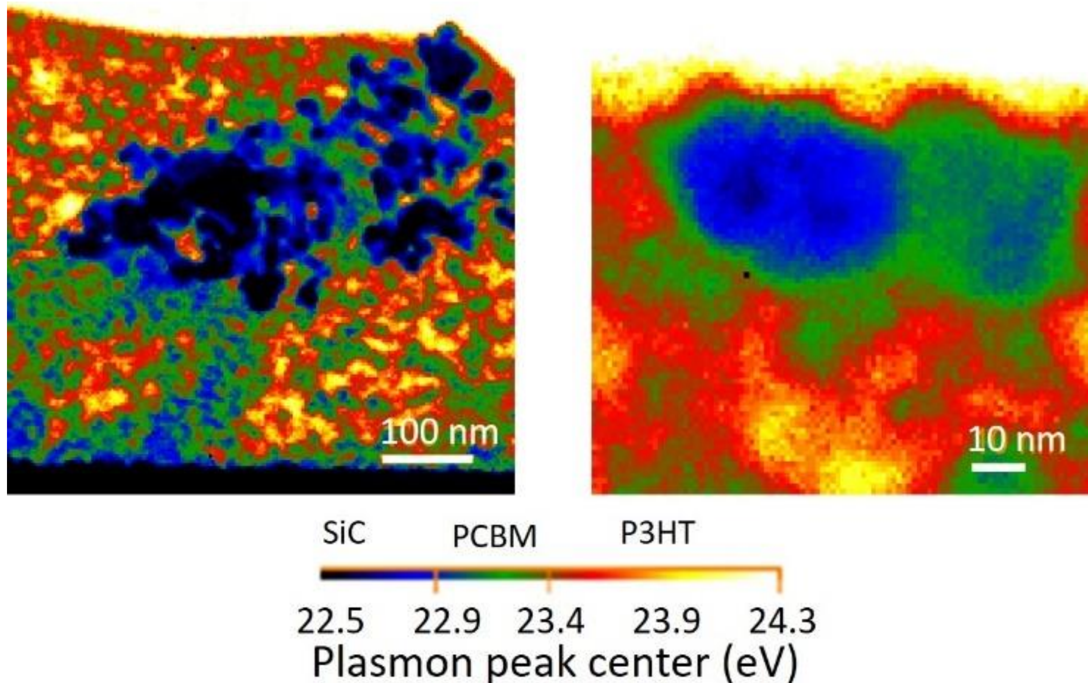

Figure 3.3.: Elemental maps derived from plasmon loss peaks of the ternary blend, where black and blue shows SiC, green $PC_{60}BM$ and red to yellow P3HT.

Survey optical microscopy images were taken in order to monitor the composition inside the blend and also the general appearance of the active layers in device stacks with and without SiC. The images of the reference device *b6* (no SiC) and sample *b5* (20 wt.% SiC) are

compared in figure 3.4. on the left and the right, respectively. The brighter rectangle in the middle of each of them is the ITO electrode, defining the active area of the devices. The reference sample (*b6*) shows a very smooth homogeneous appearance. The few dark spots are contaminations of the substrate or agglomerations of the PEDOT:PSS hole transportation layer. P3HT and $PC_{60}BM$ do not cause any visible features, as they are both very soluble in chlorobenzene.[146] Even though *b5* is the ternary blend containing the lowest amount of SiC, the film appearance seems to change drastically. The SiC nanocrystals cause serious agglomerations, turning up as bluish yellow areas, which are surrounded by P3HT rich areas, appearing in dark red. These images match the results from the TEM investigation of the lamellae very well, since also agglomerations of larger SiC particles were visible in the cross-sectional images.

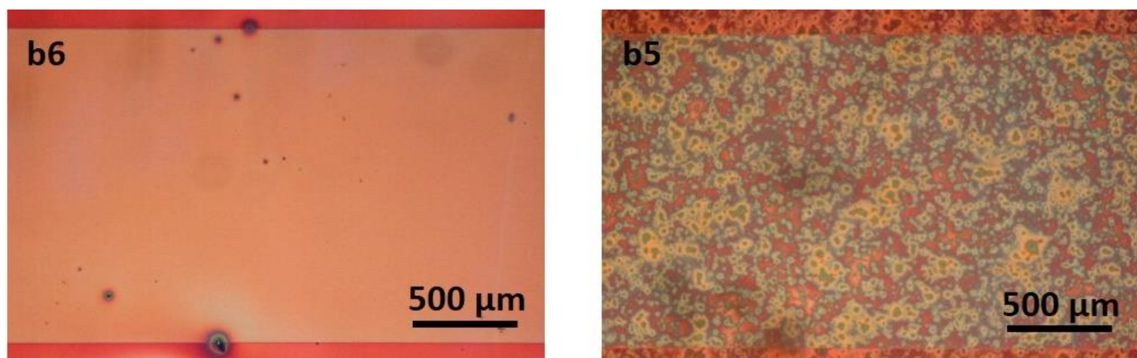

Figure 3.4.: Optical microscopy images of the devices *b6* and *b5*.

3.2.3 Integral Device Behaviour

In order to investigate the impact of step-wise exchange of $PC_{60}BM$ with SiC:N nanocrystals on the device performance, measurements of the current-voltage characteristics in the dark and under simulated solar Air Mass 1.5 Global (AM1.5G) irradiation were conducted. While keeping the P3HT-to-acceptor mass fraction constant, the $PC_{60}BM$ and SiC mass fractions of the acceptor part were changed in steps of 20 wt.% in the devices' active layer. The according dark and light I-V characteristics are compared in figure 3.5. and 3.6., respectively. Each of the chosen illustrated curves was representative for the according condition (i.e. acceptor composition in devices' active layer).

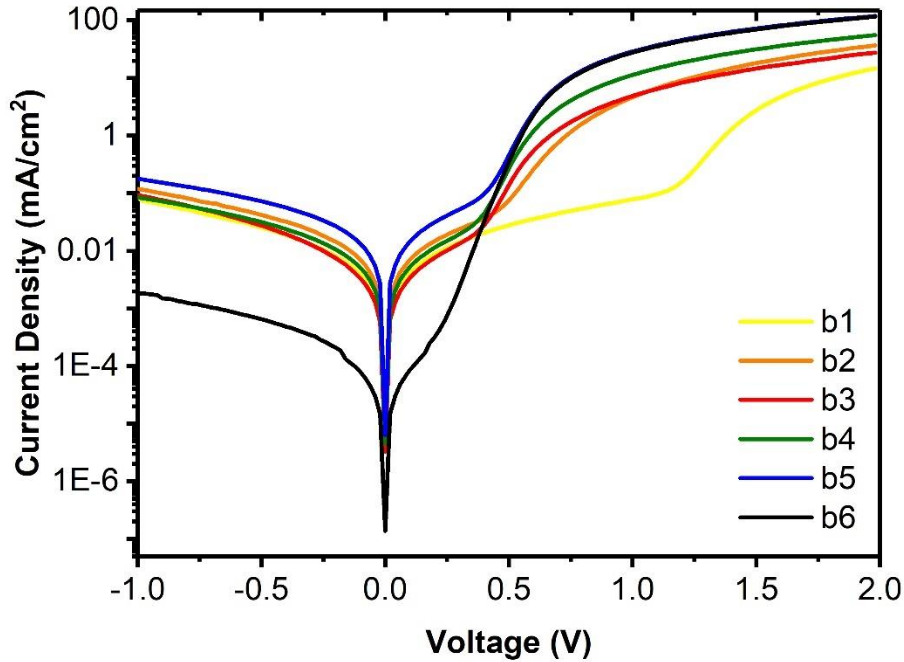

Figure 3.5.: Semi-logarithmic plot of the I-V characteristics recorded without illumination for devices with decreasing SiC acceptor fraction, from 100 wt.% SiC (*b1*) to no SiC (*b6*).

To be able to make statements about the diode properties of the devices, the recorded dark I-V curves are plotted semi-logarithmic. For all samples clear ohmic behaviour can be found in the shunt region between -0.2 and 0.2 V. The *b1* (100 wt.% SiC) characteristic exhibits a dip at about 1.2 V, indicating that there are charge traps present in the device, where for detrapping of the carriers a particular amount of energy (larger than the trap energy) is required. Sample *b2* exhibits also a slightly different shape than *b3 – b6*. This can be explained by surface trapping that is still present for *b2* as the SiC crystallites are not completely covered by the organic $PC_{60}BM$, but distinctively less strong than for *b1* where the organic acceptor material is completely absent. However, no such features occur in the dark I-V curves recorded from the other devices. In the space charge limited current region (>1 V), the slopes of all devices except for *b1* and *b2*, show no significant difference, indicating that their charge carrier mobility is comparable. Under reverse bias (V < 0) the reference sample *b6* (no SiC) shows a current density of $1.8 \cdot 10^{-3}$ mA/cm^2 at -1 V. This value is with up to two orders of magnitude, remarkably lower than for any devices containing SiC, where the current density at -1 V lies between 0.07 mA/cm^2 for *b1* and 0.17 mA/cm^2 for *b5*, indicating the presence of significant leakage pathways.

As can be seen from the light I-V curves (figure 3.6.), *b1* with exclusively SiC as acceptor, exhibits only a very low photocurrent under AM1.5G illumination and even under higher forward bias merely a flat current onset. This is an indication that strong trapping and charge transfer barriers at high light intensities lead to failure of the device.

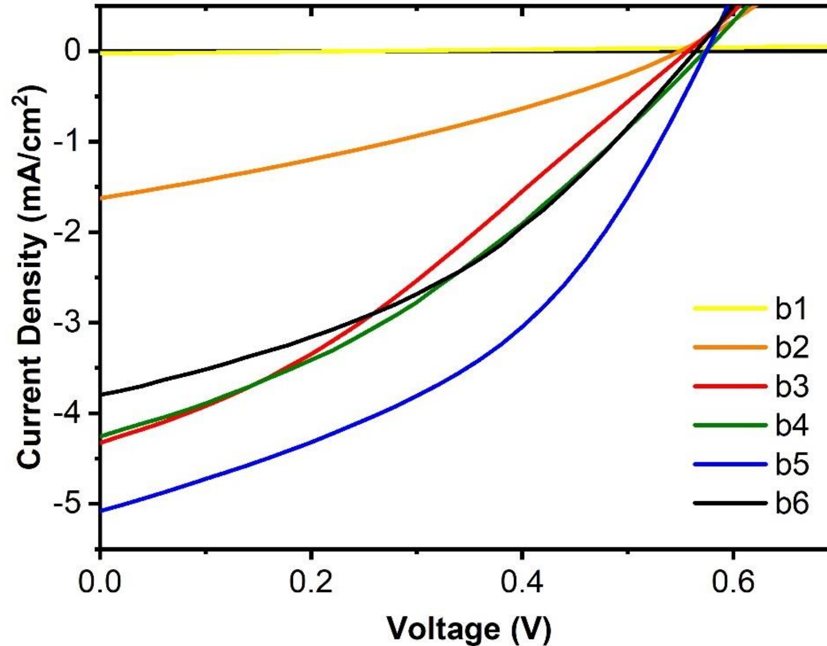

Figure 3.6.: Light I-V characteristics of devices with decreasing SiC acceptor fraction from 100 wt.% (*b1*) to 0 wt.% (*b6*), recorded under AM 1.5G conditions.

For a small addition of $PC_{60}BM$ in sample *b2* the performance already improves remarkably, showing a significant photocurrent, although the current onset is still flat and FF is low. This improvement originates from the incomplete coverage of SiC crystallites by $PC_{60}BM$, already leading to the partial deactivation of the trap state of the SiC surface. The V_{OC} and J_{SC} of the curves recorded for intermediate compositions in *b3* (60 wt.% SiC) and *b4* (40 wt.% SiC) are very similar, but it can be seen that their rectangularity and therefore the FF increases with decreasing SiC content. The best performance is clearly reached for *b5*, the sample with smallest acceptor fraction of SiC (20 wt.%). The reference sample *b6* (without SiC) in contrast, exhibits decent rectangularity but significantly lower photocurrent than the *b3* and *b4* devices.

To visualize relative changes of the solar cell key values better, namely V_{OC}, J_{SC}, FF and PCE, they were extracted or calculated from the corresponding characteristics, normalized and summarized in figure 3.7.

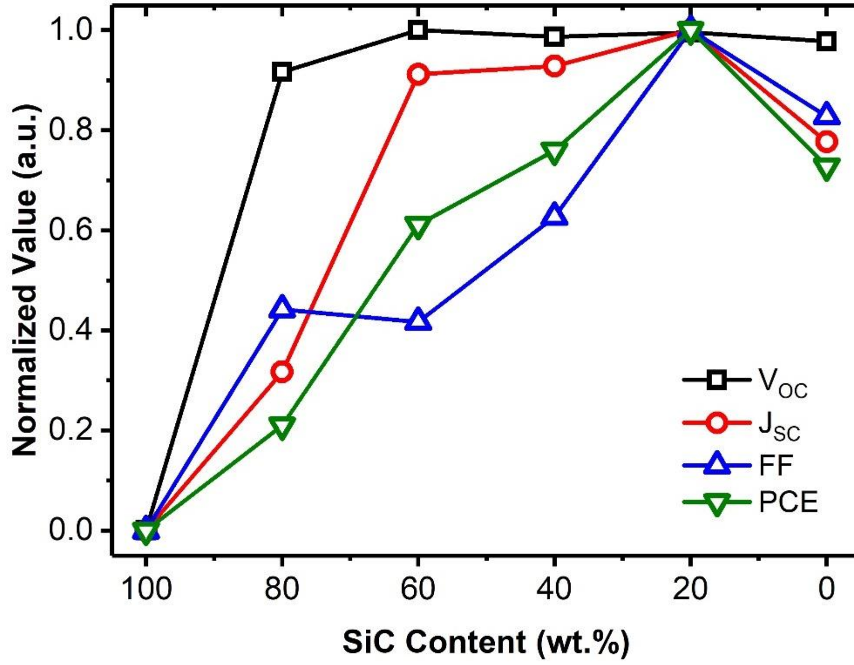

Figure 3.7: Illustration of the evolution of solar cell key parameters with changing SiC content in the devices.

The corresponding values of the photovoltaic performance parameters are averaged over at least 24 devices for each different active layer composition and are listed in table 3.2.

Table 3.2: Summary of the averaged values of the key parameters obtained for the different active layer compositions.

Name	SiC fraction of acceptor (wt.%)	V_{OC} (V)	J_{SC} (mA/cm^2)	FF (%)	PCE (%)
b1	100	0.08	-0.02	19.4	$9\cdot10^{-4}$
b2	80	0.52	-1.47	29.5	0.46
b3	60	0.56	-4.19	28.9	1.34
b4	40	0.55	-4.26	33.7	1.67
b5	20	0.55	-4.59	42.2	2.20
b6	0	0.55	-3.57	38.3	1.60

For clarification: The discussed device performances for samples *b1 – b6* addressed in the following, always refer to the averaged batch values, unless stated otherwise, e.g. when directed to representative curves of an according sample batch from figure 3.6.

The all-organic binary reference *b6* shows a PCE of 1.6%, a V_{OC} of 0.55 V, a J_{SC} of -3.57 mA/cm^2 and an FF of 38.3%. These values act as standard, utilized to demonstrate the impact that SiC has on the solar cell key parameters.

The poorest performance is exhibited by *b1*, which is a binary blend of P3HT and SiC in a weight ratio of 1:1. This reflects in all averaged key parameters as can be seen in table 3.2. and is clearly visible from plotted values in figure 3.7. The reason for this low output with a PCE of $9 \cdot 10^{-4}$% is most likely the circumstance that the inorganic SiC and the conjugated polymer interact insufficiently with each other. This is also supported by the absorbance measurements (see section 3.2.4.), suggesting completely undisturbed crystallisation of P3HT in presence of SiC, indicating the SiC surface rather acting repellent against P3HT wetting. For the charge transfer and charge transport processes between these two phases, which are vital for the device's functionality, this is disadvantageous. Most performance losses here originate from the inorganic material possessing a high abundance of traps due to surface defect states, which affect exciton dissociation, charge recombination and the mobility. That problem commonly appears for this class of materials. Another reason, which has a negative impact on the charge transport is that SiC crystallites do not form enough percolated pathways throughout the film, as is supported by the film's cross-sectional images of the extracted lamella (see section 3.2.2.). Furthermore, a lack of inter-crystalline contact by oxide layers or problems with the wettability causing limited P3HT/SiC interfacial contact are possible reasons for the low performance. By the addition of a small amount of $PC_{60}BM$ for *b2*, the device performance already shows a notably increased PCE value of 0.46%, which is induced by a rise of both, V_{OC} and J_{SC}. However, the FF remains fairly low. This behaviour indicates that replacing 20 wt.% of SiC by $PC_{60}BM$ is already highly beneficial for charge carrier transport, while charge transfer from P3HT to SiC is still partially corrupted. For *b3* and *b4* the performance improves further, resulting in PCEs of 1.34% and 1.67%, respectively. For these two intermediate film compositions (SiC fractions 60 and 40 wt.%), current density and voltage already reach (V_{OC}) and even exceed (J_{SC}) the values of the all-organic control blend *b6*, with FF being the only remaining comparatively low value. This indicates that the charge transfer still could be more efficient. The best overall device performance with a PCE of 2.2% can be found in *b5*, with SiC weight fraction

of 20 wt.%. The FF shows a modest enhancement of 4% compared to the control batch and the J_{SC} is elevated by more than 1 mA/cm^2 compared to the all-organic binary system.

The remarkably small V_{OC} for *b1* probably originates from trap-assisted recombination of the charge carriers or/and hindered charge-transfer at interface barriers (e.g. oxide layers on SiC crystallites). What supports the first theory, is the fact that a massive V_{OC} rise from 0.08 V in *b1* to 0.52 V in *b2* is observed, which suggests that a small fraction (20 wt.%) of $PC_{60}BM$ in the acceptor phase (80 wt.% SiC) already helps to nearly overcome this problem. For samples *b3* to *b6* the V_{OC} settles at a stable value of 0.55 – 0.56V. The J_{SC}, also extremely small in *b1*, already improves strongly by the addition of $PC_{60}BM$ in *b2*. For *b3* to *b5* photocurrent is higher compared to the control samples, but peaking with the highest values is *b5*, with 20 wt.% SiC and 80 wt.% $PC_{60}BM$.

As can be seen from figure 3.7., *b1* to *b4* exhibit a relatively low FF, but gradually improving nevertheless with increasing amount of $PC_{60}BM$ in the active layer. This is an indication for insufficient charge transfer between active layer's SiC phase and the cathode at absence or too low concentrations of $PC_{60}BM$, suggesting that a coverage of the SiC crystals by $PC_{60}BM$ (as was seen in the elemental maps (see figure 3.3.)) is beneficial also for enhanced electrode contact.

Most remarkable is the persistent increase in efficiency, dominated by a rise in J_{SC} and FF, when the SiC-to-$PC_{60}BM$ ratio decreases, with both values being highest at a ratio of 20 wt.% to 80 wt.%. This ratio seems to allow the advantages of SiC to unfold and contain its morphological disadvantages. By proper coverage of the SiC particles by the fullerene derivative, SiC surface traps are deactivated, thus trap-assisted recombination, typical for hybrid organic-inorganic blends is reduced. Further, $PC_{60}BM$ forms bridges for the charge transfer between the SiC crystallites and between the SiC crystallites and the cathode. Therefore, choosing the proper ratio between the organic and inorganic acceptor material seems to be the crucial point for the formation of a ternary blend with improved device performance.

3.2.4 Photophysics and Photoresponse

To get further insight in the photophysical properties of the devices, their spectral response was recorded. Thereby the monochromatic light intensities were considerably lower than under simulated solar illumination. The absolute EQE spectra are depicted in figure 3.8. on

the left, where for each active layer composition a representative device was chosen. For *b1* (100 wt.% SiC) the shape of the EQE spectrum is hardly visible and efficiency stays fairly low, below 5%, because of the charge transfer/transport problems discussed in section 3.2.3. Replacement of 20 wt.% of SiC acceptor by $PC_{60}BM$ for *b2* already massively improves the EQE, due to the better transport properties, as already mentioned in the previous section. This leads to an EQE of 25%, with the maximum located at a wavelength of 430 nm. The peak of *b3* with 60 wt.% SiC is shifted to lower energies and exhibits a maximum of 45% at 480 nm. For *b4* with 40 wt.% SiC the EQE even reaches a value of 50% at a wavelength of 495 nm. The highest values, close to 55%, were measured for both, *b5* with 20 wt.% SiC and *b6* without SiC, and are located at 490 nm. As EQE is proportional to the J_{SC} at a particular wavelength, it is affected by the same factors as the previously discussed current density, namely the optical absorption, exciton dissociation at donor/acceptor heterojunction sites and transfer of the charge carriers. Therefore, the trend of the EQE maxima of the respective samples reflects well the trend in photocurrent of the solar IV curves.

The curves were normalized (figure 3.8. on the right) in order to facilitate comparison of the shapes of the EQE spectra of the devices and therefore be able to distinguish spectral contributions to the photocurrent originating from SiC or from P3HT. The spectral response of reference device *b6* shows a spectral profile which is typical for P3HT:$PC_{60}BM$ devices.[147] It consists of a large, broad peak ranging from 380 to 680 nm exhibiting a maximum at around 500 nm and a subtle shoulder at 610 nm.

This profile basically reflects its absorption spectrum as can be seen in figure 3.9, showing the normalized absorbance spectra of respective active layer films with compositions *b1* to *b6* on quartz. The EQE of *b1* shows the signature contribution of P3HT[148] as well, but some additional contribution can also be observed ranging from 500 nm down to the shorter wavelength range. This feature probably appears due to absorption originating from SiC. As SiC is a wide band gap semiconductor with an indirect bandgap, the absorption onset is in the visible range (539 nm for SiC:N) but the main contribution to the absorption appears in the UV range and a contribution to the absorption would be low in intensity compared to the one of P3HT.[149,150] An alternative explanation could be that this is a measurement artefact, caused by the low signal intensity and calibration issues. The shape of the *b2* EQE spectrum shows a dip around 500 nm (which is also visible for *b1*) which is an indication for self-absorption, caused by SiC agglomerations covered by the organic material. These islands, with a thickness of about 900 nm, have a massively enhanced layer thickness in comparison

to the rest of the film (see figure 3.2., left). This enhanced thickness hinders charge carries generated in these areas of the active layer from reaching the electrodes. This contribution is not visible in the absorption spectra (see figure 3.9., left) as it is perfectly superimposed by the absorption of P3HT and probably quite low in intensity. If the contribution that was found at the low wavelength part of the spectrum originates from SiC, then no remarkable contributions to the photocurrent would appear due to the low absorption of the inorganic material. When further replacing SiC by $PC_{60}BM$ (*b3*), the EQE peak still looks flattened. This originates from the remains of the m-shaped deterioration which is best visible in *b2*. This feature becomes much less pronounced with increasing $PC_{60}BM$ content. Sample *b4* does not show remains of this distinctive feature anymore and instead exhibits a shape more similar to the reference device, as does *b5*, which is nearly identical to the control sample *b6*.

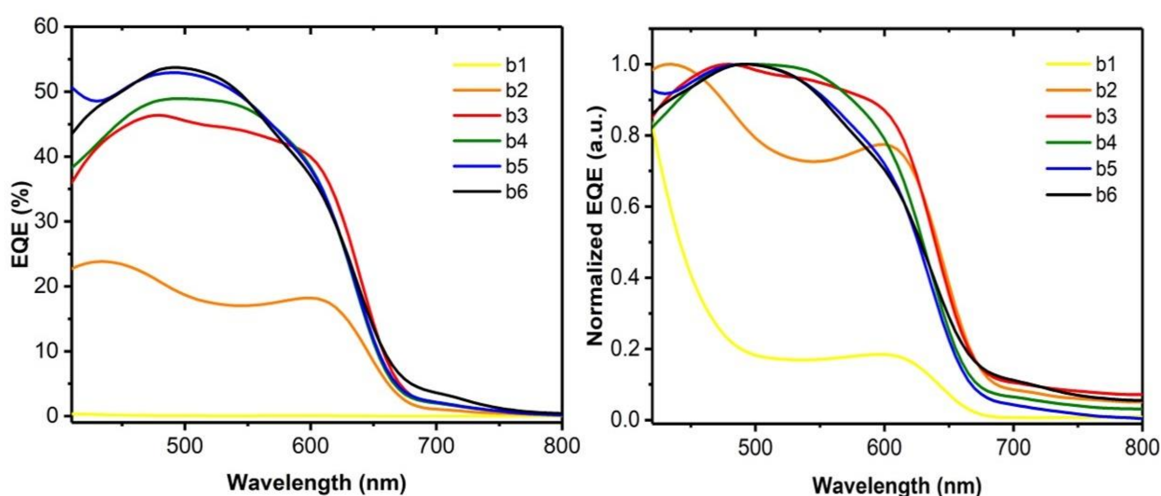

Figure 3.8.: EQE curves as recorded (left) and normalized (right) of devices *b1* to *b6*.

The impact of the SiC content on the photophysics of $P3HT{:}PC_{60}BM{:}SiC$ blends was investigated by UV-vis absorbance and photoluminescence measurements. The normalized absorbance and PL spectra are shown in figure 3.9. on the left and on the right, respectively. The absorbance-spectrum of the reference sample *b6* shows the typical broad absorption feature between 400 and 650 nm known for this combination of materials. The most prominent peak located at 504 nm originates from the π-π absorption and the shoulders at about 550 nm and 600 nm originate from the vibrionic absorption in P3HT.[148] The contribution of $PC_{60}BM$ is not visible as it is located in the ultraviolet range between 300 and 350 nm.[148] Regarding samples *b5* to *b1,* with increasing content of SiC (and therefore decreasing content of $PC_{60}BM$) in the blends, the main peak which is located at 504 nm for

the reference sample, continuously shifts to the red wavelength range. For the blend with 100% SiC (*b1*) this feature is located at 522 nm, leading to a total shift of 18 nm. The wavelength where the maxima for the different blend compositions appear are summarized in table 3.3. What is also noticeable is the relative rise in intensity of the shoulders at around 550 nm and 600 nm with increasing SiC content, which tend to become more pronounced and gain in relative intensity compared to the main peak. Like the main peak, these two features also shift to higher wavelengths with increasing amount of SiC in the blends. This continuous modification and red shift of the spectra with decreasing content of $PC_{60}BM$ can be attributed to the improvement of the polymers conjugation length and ordered structure of the P3HT molecules in the films, suggesting that the polymer does not interact with the SiC crystallites without the presence of $PC_{60}BM$. This observation of the improvement of the inter-chain interaction of P3HT is also consistent with previous reports, showing that $PC_{60}BM$ has a disturbing influence on the ordering in P3HT chains, which gets worse with increasing $PC_{60}BM$ content.[151]

Measurements of the PL were carried out to investigate the efficiency of exciton dissociation in the blends. All of the samples were excited at a wavelength of 512 nm, at the maximum of the P3HT absorption. The PL spectra of all samples show a very similar asymmetric line shape, which consists of the typical emission features of P3HT, the *0-0* emission appearing as a shoulder at about 650 nm and the *0-1* emission at about 720 nm, which is the prominent main peak.[152] The intensity ratio of 0-0 and 0-1 peak shows no significant change with changing SiC:$PC_{60}BM$ ratio. The organic binary sample *b6* shows a blue shift- compared to the blends containing SiC which reflects the trend of the absorption measurements, revealing that $PC_{60}BM$ disturbs the ordering of the conjugated polymer.

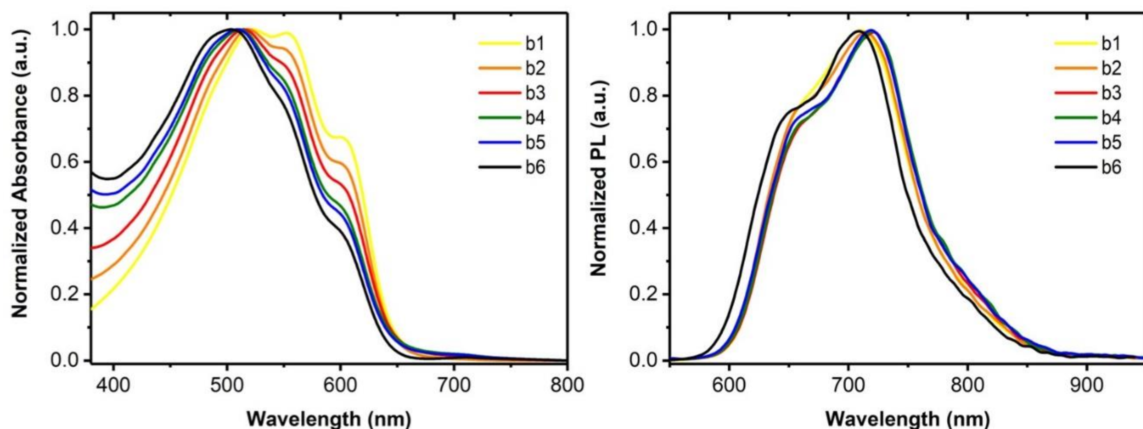

Figure 3.9.: Normalized absorbance (left) and PL spectra (right) of film samples of *b1* to *b6* on quartz.

For the background-corrected absolute photoluminescence quantum yield measurements, the samples were excited at the respective wavelength of their maximum in absorption. The according values can be found in table 3.3. As a previous report shows, the QY derived from a pristine P3HT film has a value of 4.35%.[153] By blending the P3HT in a 1:1 ratio with SiC (*b1*) this value is strikingly lowered by quenching to 1.05%, showing that the created excitons are able to reach the donor acceptor interface before recombination takes place. The exchange of only 20 wt.% SiC by $PC_{60}BM$ (*b2*) further lowers this value significantly to 0.26%. This is a confirmation of the previous assumption that binary SiC and P3HT films exhibit problems with the wettability and interact poorly with each other in the absence of $PC_{60}BM$. For further exchange of SiC by $PC_{60}BM$ the QY becomes gradually lower with decreasing SiC acceptor fraction to 0.22% (*b3*), 0.21% (*b4*) 0.19% (*b5*) and the lowest value of 0.17% for the organic binary thin film *b6*. This can be explained by the increased efficiency of the exciton dissociation as a higher $PC_{60}BM$ content results in a larger donor acceptor interface area. The QY calculations reveal that the quenching in *b1* is efficient compared to sole P3HT, but the exciton diffusion is still limited in the absence of $PC_{60}BM$ in the thin films. This can be attributed to defects at the surface of the SiC crystallites which trap the created charge-transfer-states and lead to recombination of the charge carriers emitting at a wavelength in the infrared range.[153] This also matches the results of the comparably low photocurrent output (see figure 3.7).

Table 3.3.: Summary of the obtained quantum yields and respective excitation wavelength λ_{ex} for the blend films with changing acceptor composition.

Name	λ_{ex} (nm)	Quantum Yield (%)
b1	522	1.05
b2	519	0.26
b3	514	0.22
b4	511	0.21
b5	509	0.19
b6	504	0.17

The large difference in emission intensity is even visible with the naked eye, as can be seen in figure 3.10, showing a photograph of the sample *b1* (100 wt.% SiC) and *b2* (80 wt.% SiC) placed under UV light. The red glow of sample *b1* originates from the emission from P3HT.[154] For *b2* in contrast, emission is too weak to be visible, showing its improved quenching in the presence of $PC_{60}BM$ in the blends. The luminous blue parts show the two-component resin used for encapsulation of the devices.

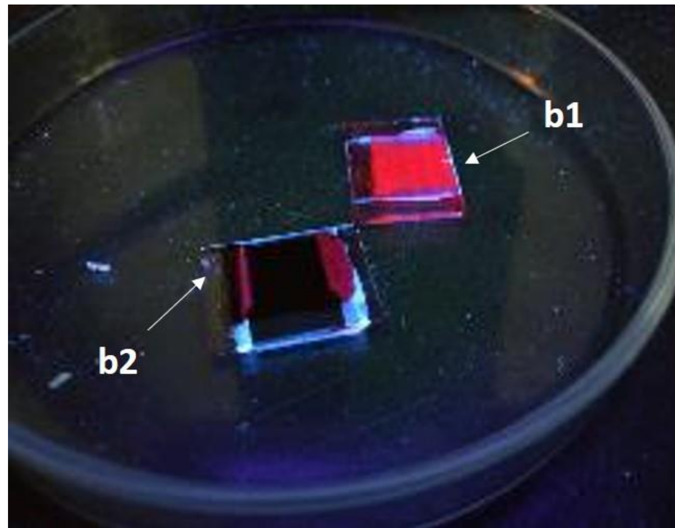

Figure 3.10.: Photograph of the devices *b1* and *b2* illuminated by an UV-lamp.

3.2.5 Spatially-Resolved Device Characteristics

One of the central points when determining the performance of a hybrid device is the morphology as it influences the exciton dissociation, charge carrier mobility and both geminate and non-geminate recombination. Therefore, survey maps of the spatial distribution of the photocurrent were obtained by LBIC scanning with a wavelength of 532 nm (spot size ~ 2µm, step size 25 µm) on the total active device area of 4.0 x 1.5 mm, detecting inhomogeneities in the sub-mm range. The colour scales for the maps showing the relative photocurrent J_{rel} are linear and can be compared with each other, as they are normalized to the highest overall current value of all samples that was obtained from sample *b5*. The obtained photocurrent maps are illustrated in figure 3.11.

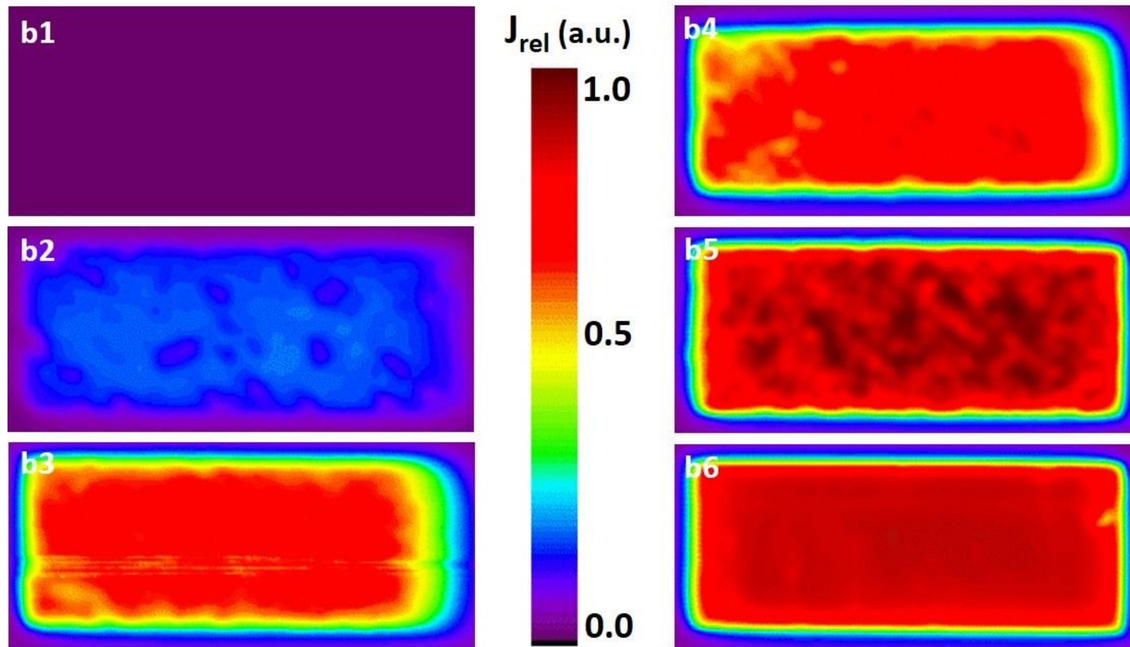

Figure 3.11.: Spatially resolved photocurrent maps of devices with blend compositions *b1* to *b6*, normalized to the highest obtained LBIC current of all 6 types, gained from *b5*.

For the sample *b1*(no $PC_{60}BM$) a negligibly small photocurrent was detected, which is represented by a homogenous violet area. The device *b2* already shows a low photocurrent, which is fairly low with about 20% of the maximum possible output. Here, local areas of higher and lower photocurrent generation can be distinguished by lighter and darker blue areas. For *b3* the values exceed the 50% of the maximum output and exhibit a quite even current generation in the central parts of the device active area. In the outer regions the current decreases. (Note: The stripe-like pattern in the lower third of the map are scanning artefacts). The sample *b4* shows a further increased photocurrent output of about 70 – 80% in major parts of the device and local spots with a significantly lower current of around 50% due to inhomogeneities in the active layer caused by agglomerations of SiC. Also, a significant decrease in photocurrent can be found in the regions close to the edges of the active area, apparent by the yellow and green frames. Still, the photocurrent generation is efficient over the majority of the device active area. The sample *b5* exhibits the highest photocurrent, even though the current generation is not uniform across the whole device area. This can be seen by the dark red patches with an output of 100% located all over the active area, which are surrounded by regions exhibiting merely 80% of the maximum performance. The hot spots of the highest photocurrent output, which must be most efficient in exciton generation, dissociation and charge transport, are likely to originate from a good

$PC_{60}BM$ coverage of SiC crystals of desirable size and properly blended with P3HT. The reference sample *b6* presents very homogeneous photocurrent generation of about 90% across the entire active device area (except for a small device defect on the outer right edge, probably contamination of the substrate). Where the border area of the devices *b2* to *b4* show a gradually decreasing performance, this effect does not appear for *b5* and *b6*.

3.2.6 Transient Photocurrent

For the purpose of better understanding of the underlying charge transport dynamics of these ternary blend devices, transient photocurrent measurements were performed. This method allows to gain information about the trapping and detrapping of charge carriers and characterize the charge carrier dynamics by monitoring the current response to a 300 µs square pulse of light. To prevent influence of the pulse frequency on the current, background illumination was avoided. Figure 3.12. compares the transient photocurrent data of selected devices for *b2* to *b6* at different applied bias voltages. The curves are normalized to the steady-state photocurrent at 200 µs. For the devices *b1* it was not possible to record signals with reliable information.

The samples *b2* to *b4* exhibit positive overshoots shortly after switching on and negative overshoots after switching off the light pulse. These differences in the rise dynamics, appearing shortly after switching on the light are present from an applied bias voltage of 0.3 V – 0.6 V and they are most prominent when approaching the V_{OC} (see table 3.2. for averaged values). With decrease of the bias, they gradually become less pronounced till they disappear below 0.3 V. Where for *b2* switching on the light causes a drastic overshoot exceeding 200% of the steady-state photocurrent at 0.6 V, these initial spikes are much smaller for *b3* and *b4*. As there are no deteriorations inflection points in the I-V characteristics, these features are not caused by a change in the working principle of the device. Instead, the overshoots can be attributed to trapped charges in the active layer. The slower dynamics appear as the trapped charge carriers need a certain detrapping time to reach the equilibrium, which is usually in the range of µs to ms.[155] This is a significant indication of the pile-up of charge carriers leading to trap mediated recombination in the devices.[156]

The negative overshoots that occur in *b2* to *b4* after switching off the light pulse are, however, an odd feature. They appear for different voltages close to the V_{OC} for the different active layer compositions. A strong overshoot of more than 100% of the steady state photocurrent is only observed for *b2* at 0.6 V. At 0.5 V, just below the V_{OC}, only a slight

feature remains visible. For *b3* and *b4* the negative overshoot is clearly smaller and only appears at 0.6 V. These negative spikes indicate charge carriers entering the device instead of leaving it slowly, which causes this current in the reverse direction. This behaviour can be explained by the fast extraction of holes in the polymer phase, where the negative charges are still trapped in the SiC. This leads to an unbalanced internal field. To readjust the field, holes are injected back into the device to neutralize the trapped electrons, allowing the device to settle back to the equilibrium.[157]

Except for the aforementioned overshoots at certain bias voltages, only little changes are observed in the rise and fall dynamics of these three devices when further changing the applied bias.

The less SiC is incorporated in the blend as far as down to 20 wt.%, the smaller the overshoots get and therefore the better the charge extraction seems to work. For the device *b5* as well as the binary reference *b6* no overshooting behaviour is visible anymore. Both devices show a balanced charge transport with no indication of blocked or delayed charges.[131]

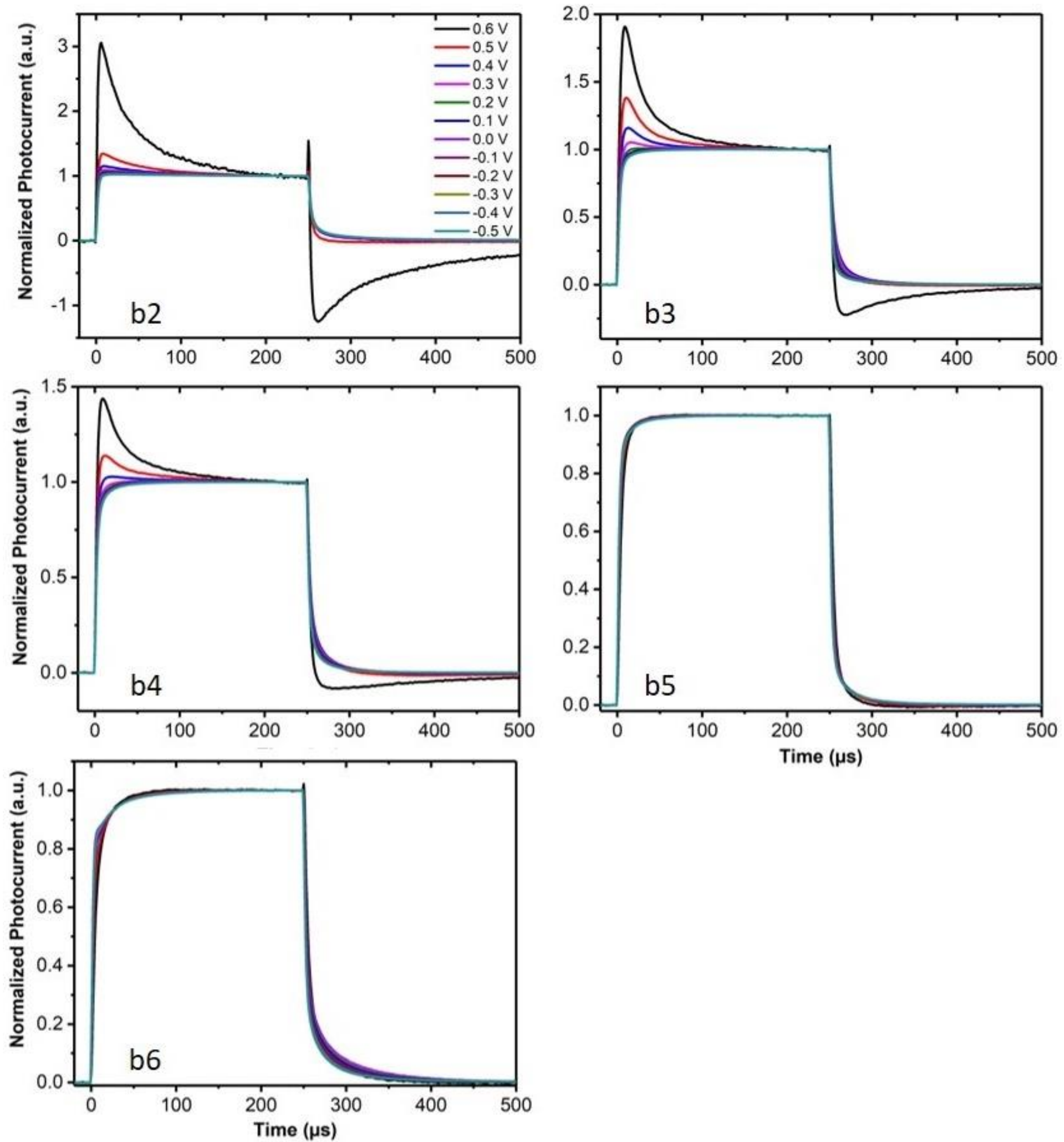

Figure 3.12.: Transient photocurrent curves of the devices *b2 – b6*, normalized to the steady state photocurrent at 200 µs, recorded at different applied bias voltages.

3.2.7 Conclusions

Investigation of the cross-sections of the active layer via elemental maps extracted from EELS spectra revealed that SiC tends to form agglomerates, where the inorganic acceptor material (SiC) is almost completely covered by the organic one ($PC_{60}BM$). The I-V measurements which were conducted on P3HT:$PC_{60}BM$ solar cells with incorporating nitrogen-doped SiC nanocrystals as co-acceptor into the active layer revealed a clear

improvement of the device performance compared to the binary organic blends if a $PC_{60}BM$:SiC ratio of 4:1 was chosen. This improvement is mainly dominated by a rise in the short circuit current density. The spectral response reveals a contribution of SiC to the photocurrent which is only very small if at all present. This matches the lack of absorption features from SiC, by super-imposition by the stronger absorption features originating from P3HT. For high SiC acceptor fraction (100 wt.% and 80 wt.%) self-absorption effects are visible. The shift of the absorption spectra to the higher wavelengths with increasing SiC content supports the assumption that SiC and P3HT interact poorly with each other. PL measurements and QY calculations show that quenching of the P3HT emission is insufficient when no $PC_{60}BM$ is present in the active layer due to the presence of trap states on the SiC surface. The exciton dissociation is improved with increasing $PC_{60}BM$ content. The LBIC technique gives additional valuable information about the functioning of these ternary hybrid cells through mapping and confirms the results of the IV measurements. Devices with a $PC_{60}BM$ ratio of 4:1 (*b5*) show photocurrent hot spots originating from a good intermix of $PC_{60}BM$ covered SiC crystallites with P3HT. The LBIC measurements reflect well the trend of J_{SC} observed from the I-V measurements. The response of the photocurrent to pulsed illumination at different applied bias voltages shows the presence of charge carrier traps for high SiC concentrations in the thin films, which seems to be overcome at a balanced $PC_{60}BM$:SiC ratio of again 4:1.

The present results suggest a clear relation between the $PC_{60}BM$:SiC ratio and the PCE. Moreover, the results from the measurements of the plasmon loss peaks and the according EELS elemental maps indicate a coverage of the SiC nanocrystals by a $PC_{60}BM$ phase, which obviously improves not only the blend and organic/inorganic interface formation, but also seems to deactivate the surface defects of the SiC crystals. In consequence, it supports more efficient charge transfer at the organic/SiC interface, better charge transport between SiC particles and reduces trap-assisted recombination at the SiC interface.

3.3 Gallium Doping of 3C-SiC and Application in Hybrid Solar Cells

3.3.1 Introduction

Till now only n-doped bulk material of 3C-SiC is available. This is probably the reason why N as the most common donor impurity has been extensively studied while comparably little is known about acceptor impurities.[119] Ga is besides, B and Al, one of the most important acceptor impurities in SiC. It substitutes just as Al on the Si position in the crystal lattice. In contrast to the more commonly used acceptor impurity Al, Ga has a lower solubility and a higher ionization energy.[36] The lower solubility of Ga and also the low diffusion constants make it more difficult to use as dopant than Al and B as it is difficult to reach sufficient doping concentrations at reasonable temperatures. Also, some growth techniques like the Lely method do not allow the incorporation of a sufficient amount of Ga impurities.[158] In 1976 Vodakov et al. presented one of the first reports of Ga atoms incorporated as impurities in the crystal lattice of 6H-SiC. They carried out doping in the vapour phase by diffusion and epitaxial growth.[159] The early papers about Ga impurities incorporated in the SiC crystal lattice of different polytypes, including 3C, are mainly focussing on investigation on the emission behaviour as Ga atoms form a luminous centre.[38,160] Also EPR investigations were reported, but only on hexagonal polytypes doped with Ga.[161,162] Until today, no reports of Ga-doped SiC fabricated via sol-gel processing as well as investigations of morphology and surface termination were found in literature. This chapter focuses on gaining more insight into the properties of Ga-doped 3C-SiC.

The first part of this chapter investigates the impact Ga-doping has on defects as well as on the structure and the surface termination. For this purpose, SiC powder samples were synthesized via a sol-gel based carbothermal reduction route (described in chapter 2.1.1.) with four different Ga concentrations. The nomenclature of the powder samples and the according nominal doping concentrations are summarized in table 3.4. The nominal doping concentration describes the amount of Ga atoms that were added in the wet chemical stage of the sol-gel process in comparison to Si atoms. It should be noted that the real doping concentration remains unknown. To find out if there is a correlation between the amount of incorporated impurity atoms and the defect density in the material EPR spectra were recorded.

Optical microscopy and SEM were used to compare the outer appearance of the differently doped crystallites. Morphological characterisations were performed via XRD. In order to gain knowledge about the surface composition XPS core level spectra were recorded.

Table 3.4.: Nomenclature and nominal doping concentrations of the 4 different Ga-doped powder samples.

Sample Name	Nominal Doping Concentration (%)
Ga-1	5.000
Ga-2	2.500
Ga-3	1.250
Ga-4	0.514

The second part of this chapter is dedicated to hybrid solar cells. The devices were fabricated with three differently doped SiC powders used as co-acceptor material: SiC:Al, SiC:N and SiC:Ga. Each of them has a nominal doping concentration of 5%. Two different concentrations (40 wt.% and 13 wt.%) of Al-, Ga- or N-doped SiC crystallites were dispersed in an organic matrix consisting of the conjugated polymer P3HT and the fullerene derivative $PC_{60}BM$. As reference binary organic devices were fabricated to see how the solar cell key parameters and photophysical behaviour changes when using SiC with different dopants and in different concentrations as co-acceptor. The compositions of the active layers and sample names can be found in table 3.5. As for the SiC no sedimentation for size selection was done previous to device fabrication, a buffer layer consisting of solely P3HT was deposited between the hole transportation layer and the active layer. This polymer layer with a thickness of 30 nm was applied to prevent short circuits, which occur when cathode and anode get in contact with each other. These short circuits might be caused by large SiC particles which exceed the active layer thickness. These devices were characterized electrically (dark and light I-V characteristics and LBIC) and photophysical measurements (UV-vis absorption, photoluminescence and external quantum efficiency) were performed on 6 ternary hybrid composition blends and compared with a binary organic reference.

Table 3.5.: Summary of the sample names for different device conditions and according dopants and blend compositions.

Sample Name	Dopant	wt.% SiC	P3HT:PC_{60}BM:SiC
Ref	-	0	1:1:0.00
Al-0.4	Al	40	1:1:0.40
Al-0.13	Al	13	1:1:0.13
Ga-0.4	Ga	40	1:1:0.40
Ga-0.13	Ga	13	1:1:0.13
N-0.4	N	40	1:1:0.40
N-0.13	N	13	1:1:0.13

3.3.2 Characterisation of Ga-doped 3C-SiC

3.3.2.1 EPR Investigation of Gallium Impurities in 3C-SiC

For investigation of defect structures at the atomic level, electron paramagnetic resonance is commonly the method of choice. EPR X-band spectra recorded at 77 K from the 4 samples synthesized with different Ga concentrations (see table 3.4.) are illustrated in figure 3.13. The inset in the upper right corner shows the measured intensity of the EPR signal for the different doping concentrations. In the spectra recorded from all four samples a structureless symmetric resonance at a g-factor of 2.0034 ± 0.0003 was found. The rapid growth of the EPR intensity with increasing concentration of added Ga atoms in the samples indicates the initiation of Ga-associated defects. What is notable from the inset, is the slightly lower intensity for *Ga-3* (1.25% doping) than for *Ga-4* (0.514% doping). This could be a result of problems during sample preparation. The quantitative defect concentrations were evaluated for *Ga-1*, *Ga-2* and *Ga-3* using a DPPH standard and show values of 3.505 ± 0.785 $\cdot 10^{18}/cm^3$, 1.315 ± 0.293 $\cdot 10^{18}/cm^3$ and 0.221 ± 0.050 $\cdot 10^{18}/cm^3$, respectively. The order of magnitude of these values correlates well with usual doping concentrations in SiC. The signal itself could indicate both, the presence of intrinsic or extrinsic defects, where the defect concentration clearly correlates with the initial doping concentration. Intrinsic defects

(e.g. vacancies in the Si or C sublattice) can be present in semiconductors due to not optimized growth conditions or by incorporation of impurity atoms that cause distortions in the crystal lattice. They can also be introduced on purpose e.g. when irradiating the sample with particle radiation. According to literature reports several intrinsic centres observed in the cubic polytype of SiC show a g-factor which is close to the free electron g = 2.0023.[163,164] Si vacancies in 3C-SiC have been found at g = 2.0028 and C vacancies at 2.0064 (both measured at 4K). Extrinsic defects are incorporated impurity atoms that form paramagnetic centres in the crystal lattice. Besides B and Al, Ga is one of the most important acceptor impurities in SiC. It can create deep as well as shallow levels.

Since to the present no reports of EPR studies on Ga impurities in 3C-SiC are available, the obtained g-factor will be discussed on the example of 6H-SiC, where some similarities, at least in terms of rough dimensions of the g-factors, might be likely. For shallow Ga acceptors, g-factors of 2.27 and 2.21 were reported, which correspond to its position on the hexagonal or the cubic site, respectively. At temperatures of 4.5 K deep Ga centres in 6H-SiC at g = 2.16 to 2.19 were reported. The g-factors are reported to shift to higher magnetic fields and the g-factors to according lower values with increasing temperature. Also, for temperatures >6K the hyperfine structure usually disappears.

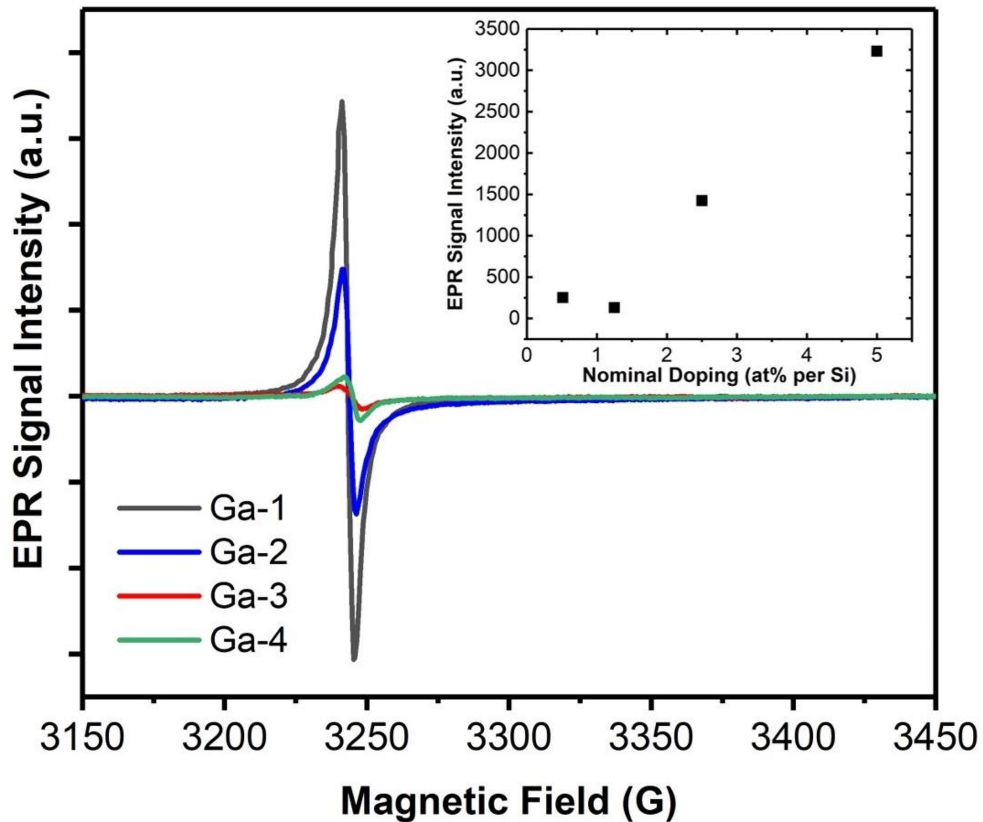

Figure 3.13.: X-band EPR spectra of 4 SiC samples with different Ga-doping concentrations recorded at 77K. The inset in the upper right corner shows the EPR intensity measured for 5.0, 2.5, 1.25 and 0.514 at% Ga per Si.

As the presented EPR spectra are recorded at T = 77 K, hyperfine structures were unlikely to occur. Based on the reported g-factors in 6H-SiC, no clear statement on the origin of the resonance detected at g = 2.0034 can be made. It could originate from intrinsic defects caused by crystal lattice distortions due to the presence of Ga atoms or from true paramagnetic Ga centres themselves. However, regarding the value of the g-factor it seems likely that the signal originates from intrinsic defects.[35,119]

3.3.2.2 Analysis of the Structure and Surface Composition of Ga-doped SiC Micro-crystals

Optical Microscopy

To have a closer look on the outer appearance of the powder samples in terms of colouring and to see whether foreign species can be found or not, optical microscopy images were recorded. Figure 3.14. (a – g) shows the images of the four samples *Ga-1* (highest doping concentration) to *Ga-4* (lowest doping concentration). Overview images of the four powder

samples have been recorded in dark field mode with a magnification of 50 times (a - d). Detailed images, with a magnification 200 times, are shown for *Ga-2* (e), *Ga-3* (f) and *Ga-4* (g). *Ga-1* is not displayed in a higher magnification as no additional information could be retrieved. The blurring which is visible in some of the images is an effect of depth of field and originates from the height differences which hinder focusing across the whole area. The green crystallites are SiC where the light spots show crystal facets that reflect the light which hits the powder samples from the side. Unreacted precursor residuals can be recognized as large black particles as they do not reflect the light. The latter were mainly found on the bottom of the graphite crucible, where the pure SiC powder grew in the top regions. When comparing the overview images, one can see that the crystallites are larger in extension for high doping concentrations (image a and b) than for lower ones (c and d). Furthermore, the colouring changes with the doping concentration. Where the samples with 5% and 2.5% doping appear in green, the colour gets lighter and turns more yellowish when the doping concentration gets lower. This is typically observed for doped 3C-SiC. For the absence of dopants in the crystal lattice the material appears in yellow due to a weak absorption in the blue wavelength range. The colour shifts from yellow to green with increasing doping concentration, because of the intraband absorption of free carries, which takes place preferentially in the red wavelength range of the spectrum.[35]

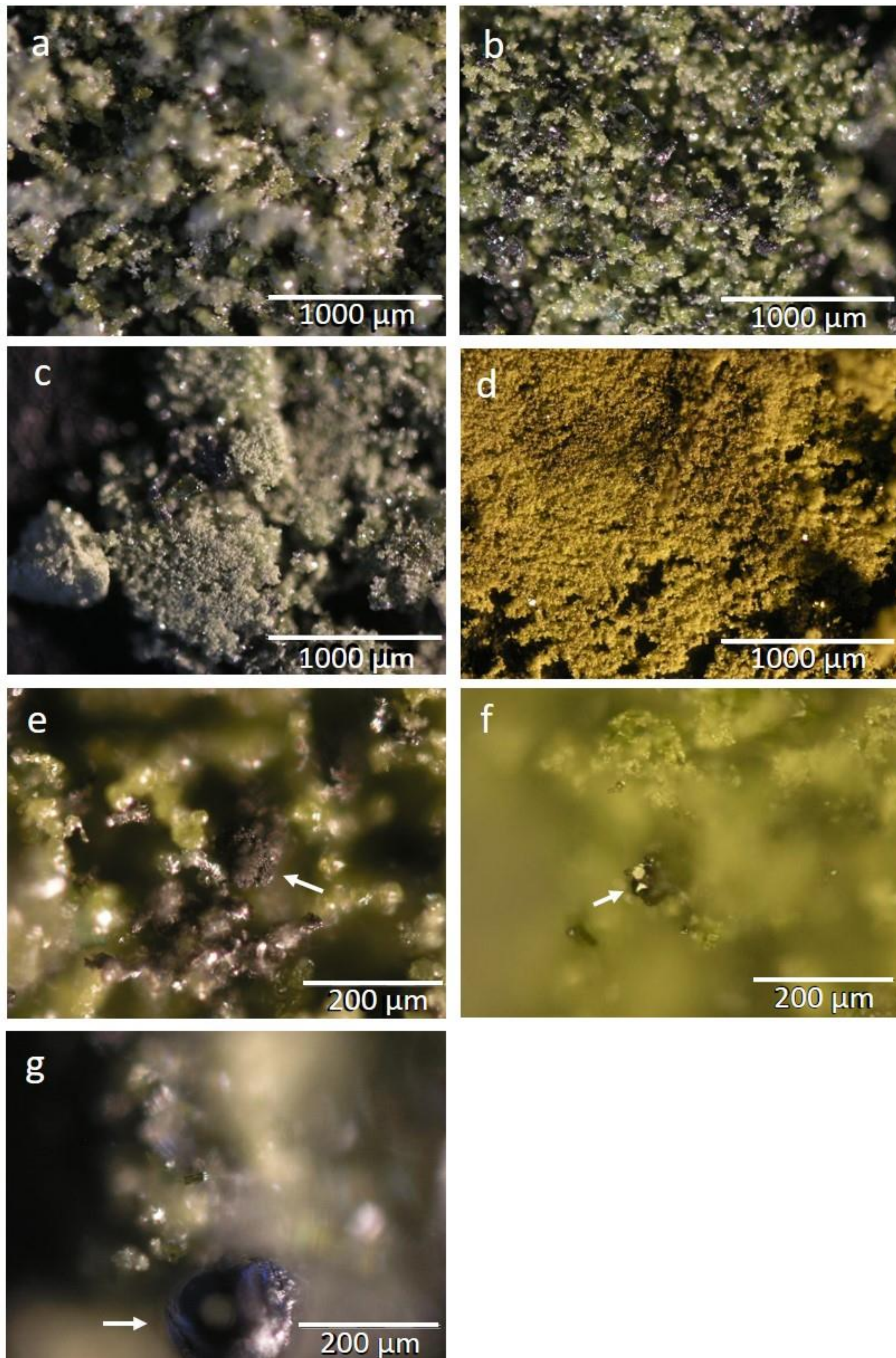

Figure 3.14.: Optical microscopy images of *Ga-1* (a), *Ga-2* (b and e), *Ga-3* (c and f) and *Ga-4* (d and g) recorded with different magnifications.

This change in absorption behaviour matches the results of the EPR analysis well, as the colour changes of the SiC samples match with the gradual signal increase with increasing doping concentration. When looking at the images taken with higher magnification, some more interesting details can be observed. Image e (*Ga-2*) shows a more detailed view of the amorphous precursor residuals, indicated by a white arrow. Image f and g are recorded from sample *Ga-3* and *Ga-4*, respectively. Both images (f and g) show grey particles (indicated by a white arrow) which reflect the incident light. The dome shaped particle in image f seems to be grown on top of a SiC crystallite with a size of about 20 µm. The round-shaped particle in image e has a much larger diameter of close to 200 µm. Particles like that were observed in different sizes in *Ga-3* and *Ga-4*, but not in the samples *Ga-1* and *Ga-2*. The composition of these particles (round and dome shaped particles) cannot be deduced with optical microscopy, requiring further analysis.

SEM Imaging and EDX

A more detailed impression of the shape of the SiC crystallites and their size distribution was obtained by recording SEM micrographs. The images taken from the 4 different doped samples were recorded at an acceleration voltage of 10 kV and are compared in figure 3.15. The large images give an overview of the powder samples and the insets show images taken with a larger magnification to have a closer look at the size and shape of single crystallites. Figure 3.15. a depicts sample *Ga-1* (5% doping) and shows crystallites in the size of about 20 µm which seem to be partially grown together and exhibit the crystal habit of the cubic manifestation of SiC. The inset shows a crystallite in the typical truncated tetrahedron shape of 3C-SiC with an extent of a bit more than 10 µm surrounded by crystallites with a size of around 5 µm that have rounded edges. In image b sample *Ga-2* is shown. The crystallites appear in the shape of hexagonal platelets that are grown together and which are more sharp-edged than the ones of sample *Ga-1*. This observation also reflects in the image taken with larger magnification in the inset, where grown together crystallites can be seen, and it is not possible to tell where one particle begins and another one ends. Sample *Ga-3* clearly shows smaller sized SiC particles (~ 10 µm) than the previous two samples but with the same crystal habit. Only a few crystallites have larger sizes of about 20 µm. One of the latter ones can be seen in the inset. It appears as if SiC particles with an extent of less than 5 µm grew on top of the truncated tetrahedron shaped particle. This detailed image also shows that for this sample the smaller crystallites are less sharp-edged than in sample *Ga-2*. Sample *Ga-4*, with the lowest concentration of impurity atoms, shows an even smaller and more homogenous

distribution of crystallite sizes than *Ga-3*. As can be seen from the inset, the larger particles in this sample have a size of up to 10 µm. The smaller ones with sizes below 2 µm still exhibit the typical truncated tetrahedron shape.

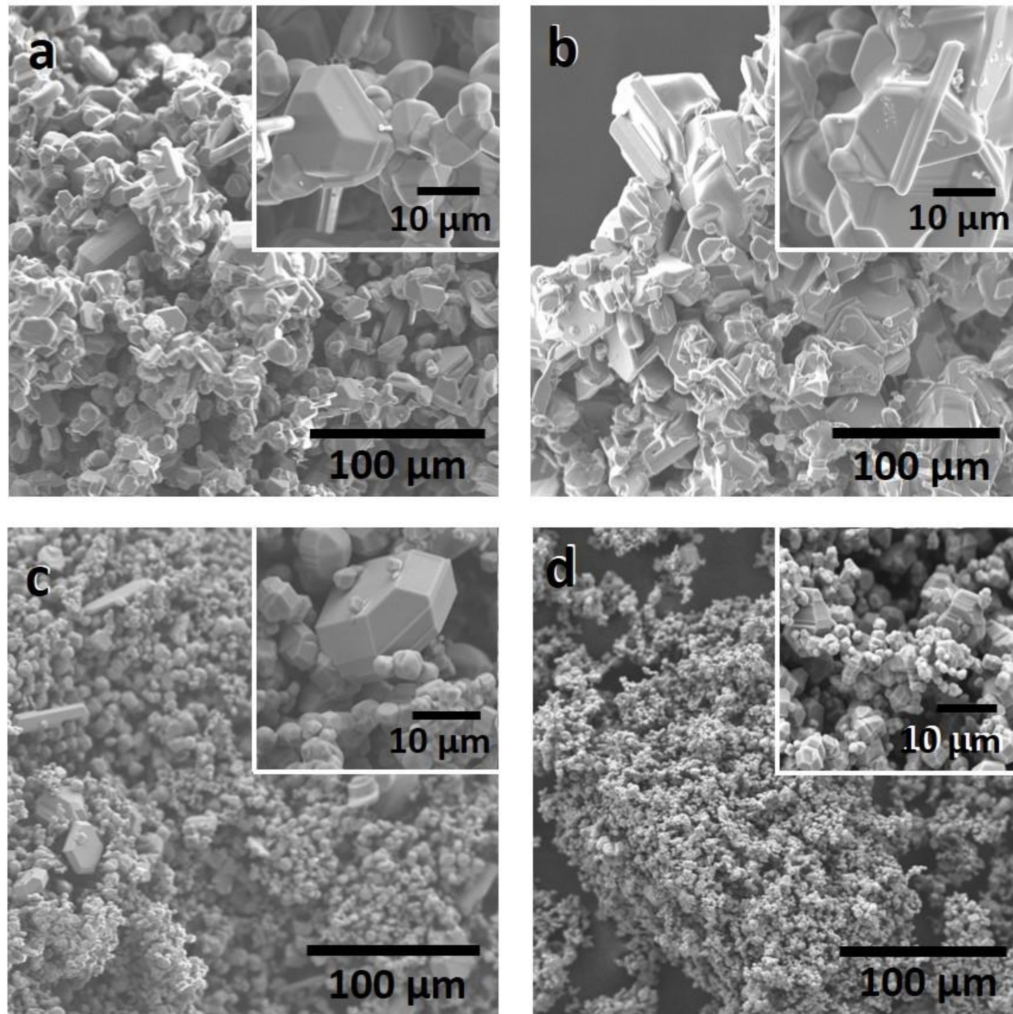

Figure 3.15.: SEM images of *Ga-1* (a), *Ga-2* (b), *Ga-3* (c) and *Ga-4* (d) taken at an acceleration voltage of 10 kV. The insets in the upper right corners show images taken with a larger magnification to obtain a more detailed view of the single grains.

Figure 3.16. on the left shows a SEM image of a round-shaped opaque particle from sample *Ga-4*. These particles were also found in light microscopy images (compare figure 3.14. f and g). It has an extent of about 300 µm and the surface appears very smooth, especially in contrast to the crystallites which reside on top of it. To investigate the elemental composition of the round-shaped particle and the crystallites on top of it, EDX spectra from the according areas labelled in the SEM micrograph were recorded and are shown in figure 3.16. on the right. For the area labelled with 1 the EDX spectrum shows a strong signal with more than

11000 counts at about 1.7 keV, which was identified to originate from Si. Another very weak signal, also belonging to Si, appears at about 3.5 keV. As no further peaks were detected in this spectrum, the material can definitely be identified as elemental Si. The spectrum recorded from the area labelled with number 2 clearly identifies the presence of C, which confirms that the small crystallites are SiC. In this spectrum the two same Si peaks as in area 1 were found, where the main peak belonging to Si shows with about 6300 counts a clearly weaker signal in comparison with the Si signal recorded from area 1. Here also two other elements were identified. The peak with 300 counts located at about 0.3 keV originates from C and a rather small trace of oxygen was found due to a very weak signal arising between 0.5 and 0.6 keV. The strong Si peak in comparison to C peak originates from the underlying Si droplet acting as a background signal.[165]

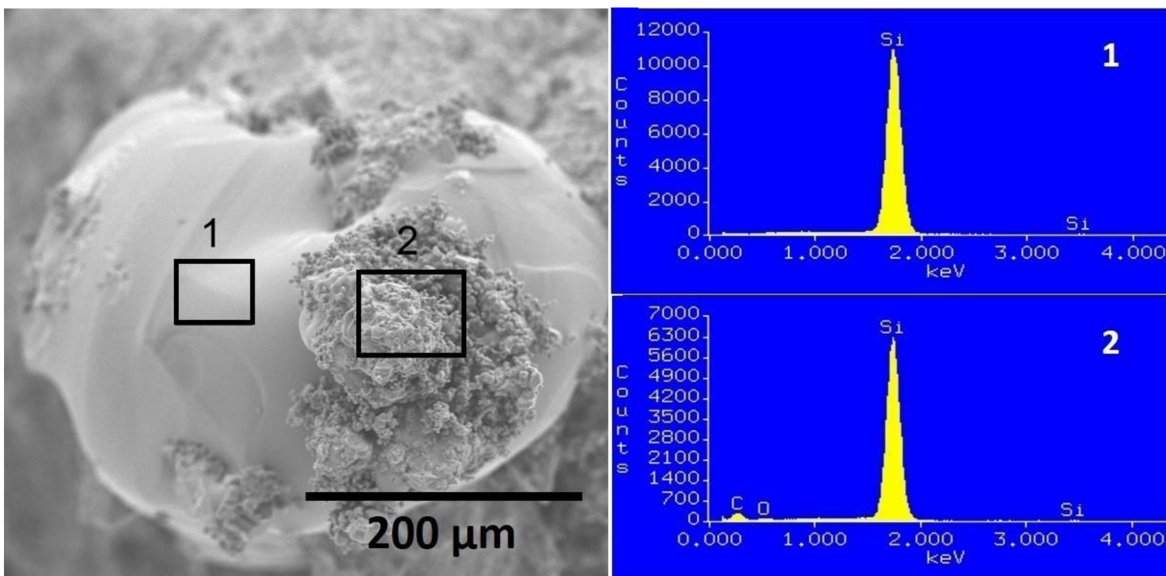

Figure 3.16.: SEM image of a drop shaped particle of sample *Ga-4* (left) and EDX spectra recorded from the areas labelled with 1 and 2 (right).

X-ray Powder Diffraction

Powder XRD spectra were recorded in order to identify which polytypes of SiC and possible other components which might have grown or fallen out during synthesis are present in the four different doped SiC-Ga samples, as well as to see if there is a correlation to the doping concentration. The patterns of all samples are displayed in an angular range from 25° to 80° as this allows clear identification of the present components.

The patterns recorded from the samples doped with 5% (*Ga-1*) and with 2.5% (*Ga-2*) are shown in figure 3.17. on the left and on the right, respectively. Both XRD spectra draw a very similar picture as the same peaks were found in both. The five most prominent peaks located at 35.6°, 41.3°, 59.8°, 71.7° and 75.3° can be assigned to 3C-SiC (JCPDS 74-2307). The corresponding d-spacings were calculated and the following values were obtained: d_{111} = 2.52 Å, d_{200} = 2.18 Å, d_{220} = 1.55 Å, d_{311} = 1.32 Å and d_{222} = 1.35 Å. The d-spacings refer to the crystal orientations (111), (200), (220), (311) and (222). Besides these peaks, two satellites around the 3C (111) peak located at 33.9° and 38.0° with calculated lattice spacings of d_{101} = 2.64 Å and d_{103} = 2.37 Å were found. They correspond to the (101) and (103) lattice planes of 6H-SiC (JCPDS 72-0018). The lattices spacings for both polytypes are in good agreement with values reported in literature.[166] Further, multiple minor peaks mainly belonging to the polytype 6H were identified. Also, very few peaks, which are comparably low in intensity, can be indexed to the hexagonal polytype 4H (JCPDS 22-1317). The investigation of the diffraction patterns confirms the presence of multiple SiC polytypes in these two samples, where it is not possible to make a statement about the exact fraction of each identified polytype. No foreign species like SiO_2 or Si were detected.

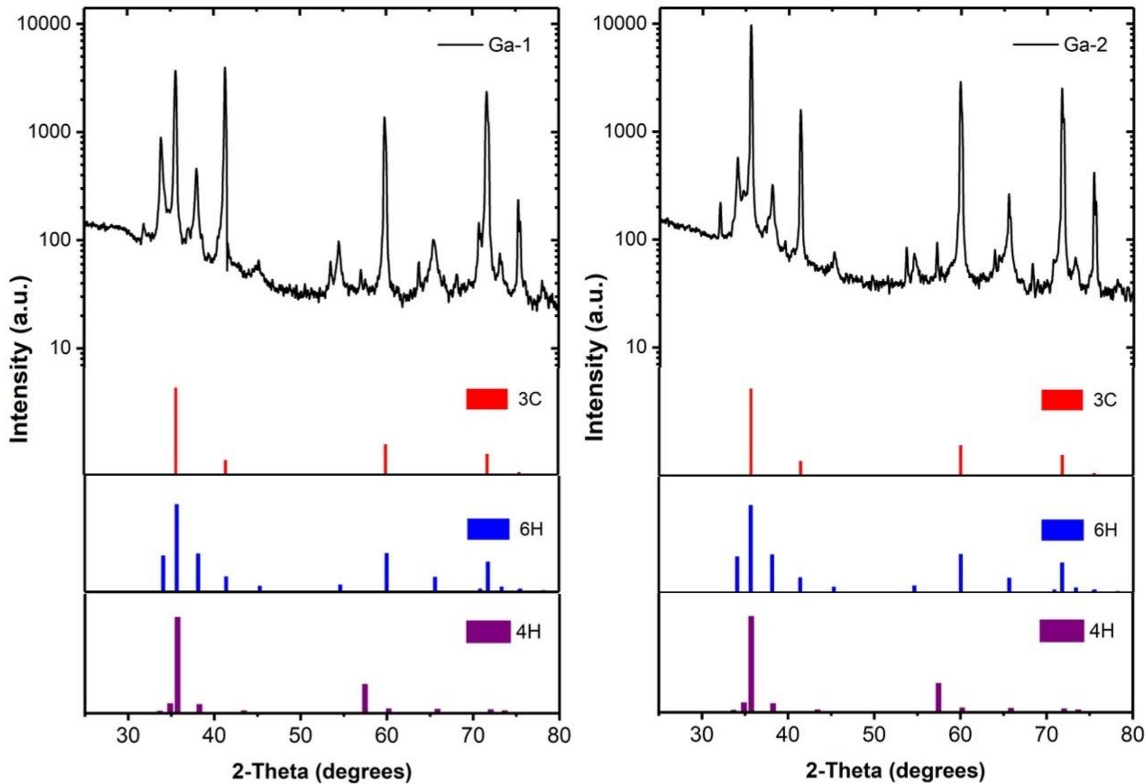

Figure 3.17.: X-Ray powder diffraction patterns recorded from the samples *Ga-1* (left) and *Ga-2* (right) shown with the according reference patterns of the identified SiC polytypes 3C (red), 6H (blue) and 4H (purple).

The XRD patterns recorded from the samples *Ga-3* and *Ga-4* are illustrated in figure 3.18. on the left and on the right, respectively. However, both of them show a different powder composition than *Ga-1* and *Ga-2*. Here the five most prominent peaks can be assigned to the cubic polytype of SiC (JCPDS 74-2307), where the (111) peak is surrounded by two satellites originating from 6H-SiC. Further minor peaks are also related to the latter polytype (JCPDS 72-0018). Interestingly, the peaks that do not belong to the polytypes 3C or 6H do not match with the diffraction pattern of 4H-SiC. These peaks are located at 28.4°, 47.3°and 56.1° and were identified as the fcc configuration of elemental Si (JCPDS 27-1402). The according d-spacings were calculated according to Braggs law and the following values were determined: d_{111} = 3.14 Å, d_{220} = 1.92 Å and d_{311} = 1.46 Å. The three peaks belong to the (111), (220) and (311) crystal plane, respectively. No traces of other polytypes besides 3C and 6H or foreign species besides Si were found in these two samples.

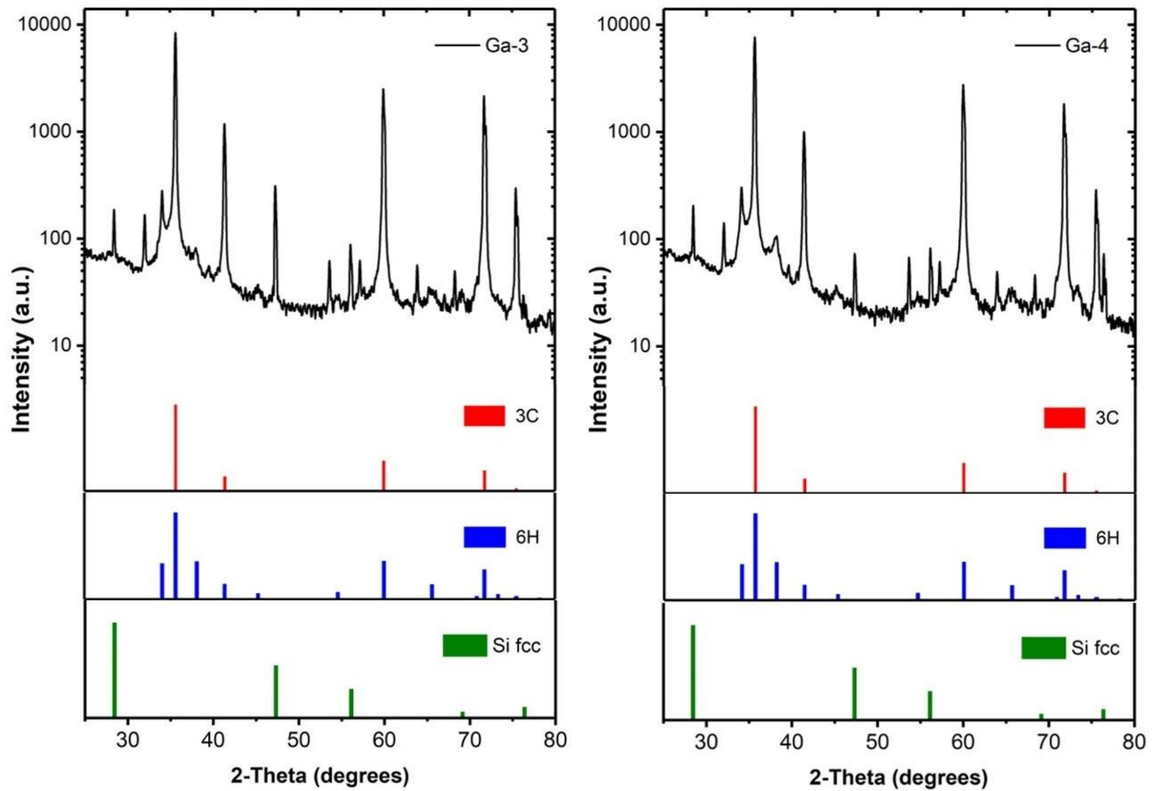

Figure 3.18.: X-Ray powder diffraction patterns recorded from the samples *Ga-3* (left) and *Ga-4* (right) and are shown with the according reference patterns of the identified species 3C-SiC (red), 6H-SiC (blue) and Si in fcc configuration (green).

When comparing the powder patterns recorded from the four samples with different doping concentrations it is notable that the 3C (200) has the same intensity as the (111) peak for sample *Ga-1*, which does not match the prediction from the reference pattern. For the three samples with lower Ga concentration the (200) peak is clearly lower in intensity but still not as low as would be expected from the reference pattern. The (222) peak is distinctively higher for all four samples as would be expected from the reference pattern. The 6H satellite peaks are most pronounced for *Ga-1* and become gradually lower in intensity with lower doping concentration. For *Ga-3* and *Ga-4* the intensity of the (101) are comparable, where the (103) peak is less pronounced for *Ga-3* in comparison with *Ga-4*. The minor peaks that were assigned to 6H-SiC are generally higher in intensity for higher doping concentrations. The peaks origination from elemental Si match the predictions, except for the (220) peaks which is distinctively higher for sample *Ga-3*. The additional peaks observed in the patterns of all four samples located at about 31.9°, 53.6° and 63.9° originate from the Cu K-β line of the incident X-ray radiation. It was possible to identify all peaks according to the database.

XPS Surface Analysis

In order to determine the chemical composition of the surfaces and see whether there is a correlation between the surface termination of the four samples to the concentration of impurity atoms incorporated into the crystal lattice or not, XPS measurements were acquired. The background corrected Si 2p and C 1s core level spectra were recorded for all four samples and are shown in figure 3.19. on the left and the right, respectively to allow the identification of different Si and C species.

The features of the Si 2p spectra were deconvoluted into four peaks for all different doping concentrations. The most prominent peaks arising in all of these spectra, located at binding energies 100.7 eV (*Ga-1*), 100.8 eV (*Ga-2*), 100.5 eV (*Ga-3*) and 100.4 eV (*Ga-4*) can be assigned to Si-C bonds of SiC.[167–171] The dominance of these peaks show that the samples primarily consist of Si-C bonds. The peaks arising at binding energies between 101.1 eV and 101.5 eV show the second most high intensity in each of the Si 2p core level spectra and were identified as O-Si-C bonds.[167,172,173]

For all samples there is a tail/shoulder visible towards higher binding energies, which originates from two underlying peaks, one located at energies between 101.9 eV and 102.3 eV and another one between 102.3 eV and 103.8 eV. Both were identified as Si-O bonds according to Alfonsetti et al., who were investigating SiO_x thin films in their different oxidation states. The Si 2p core level peaks are shifting nearly linearly from the lower binding energy side of the spectrum to the higher binding energy side with increasing O/Si content. The lowest intermediate oxide state SiO_x with $x = 1.05$ is located at 101.9 eV the fully oxidized SiO_2 can be found at 103.8 eV.[174] For the two samples with high doping concentration (*Ga-1* and *Ga-2*) the peaks originating from partially oxidized Si are fairly low in intensity. The samples with lower Ga concentration (*Ga-3* and *Ga-4*) exhibit more pronounced features indicating that more of the partially and fully oxidized species are present on the surface.

A comparison of the C 1s core level spectra of the four powder samples is shown in figure 3.19. on the right. Each of the spectra is a superposition of four peaks originating from various different bond types.

The peak located at the lower binding energy side of all spectra arising at 283 eV (*Ga-1* and *Ga-2*), 282.6 eV (*Ga-3*) and 282.7 eV (*Ga-4*) were identified as C-Si bonds of SiC.[171,175,176] The most prominent peak is located at the same binding energy of 284.7 eV in all spectra

and can be assigned to C-C bonds, revealing a strong presence of graphitic carbon on the surfaces.[177] However, for *Ga-4* the relative intensity of the C-Si peak compared to the C-C peak is clearly the highest where it is rather low for *Ga-2* and *Ga-3*. The presence of oxygen related contributions in the form of C-O bonds were found at binding energies of 285.5 eV (*Ga-1*), 285.6 eV (*Ga-2*) 286 eV (*Ga-3*) and 285.8 eV (*Ga-4*).[171,178–180] The peaks at high binding energies, which are quite low in intensity for all samples, are located at 288.8 eV (*Ga-1*, *Ga-2* and *Ga-4*) and at 288.6 eV (*Ga-3*) and correspond to carbon species that have a total of three bonds to oxygen atoms (O-C=O). They occur as predicted in literature ~ 4 eV shifted from the parent carbon peak. One representative for this species would be carboxylate groups.[180]

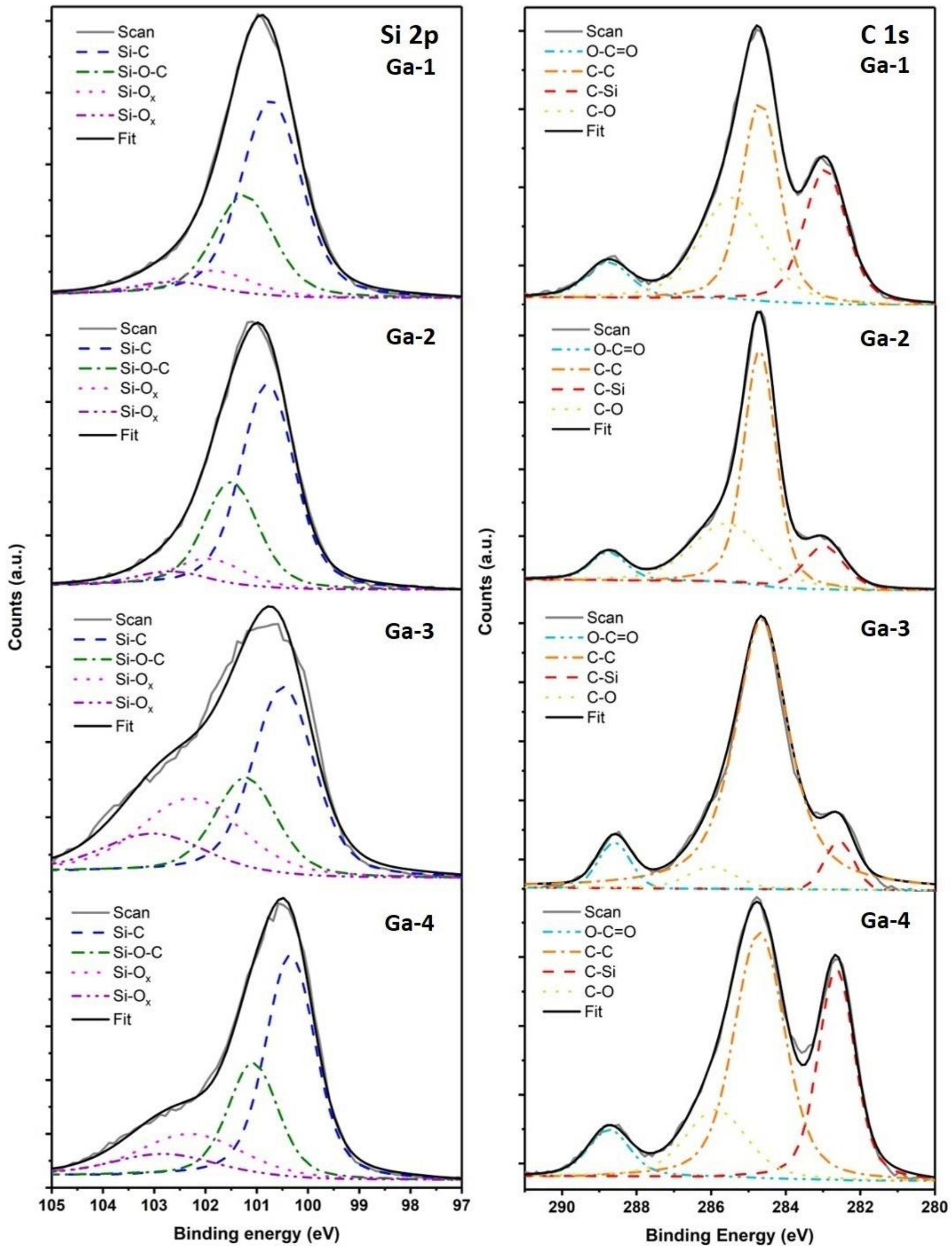

Figure 3.19.: XPS Si 2p (left) and C 1s core level spectra (solid lines) deconvoluted in the single components (broken lines) for the four SiC:Ga powder samples with different doping concentrations.

3.3.2.3 Discussion of Ga-doped SiC Powder Samples

EPR measurements reveal a structureless signal at g = 2.0034. The EPR intensity correlates with the nominal doping of the samples, which confirms the rise in defect concentration with higher doping concentrations. The defects are most likely of intrinsic nature caused by lattice distortions caused by the presence of Ga atoms in the crystal lattice. An indication for different defect concentrations in the four samples was also found by optical microscopy. The colour of the powder samples changes from green for high doping concentration to a greenish yellow for lower doping concentrations. This shows the presence of more defects in the samples with higher doping concentrations which matches the EPR results well. Also, opaque drop and dome shaped particles were found in *Ga-3* and *Ga-4*. The latter were also detected in SEM images and EDX spectra revealed that they consist of Si. Detailed imaging of the samples showed that higher doping concentration leads to the formation of more facetted particles with a larger average grain size. XRD measurements revealed that the powder samples with high (*Ga-1* and *Ga-2*) and low (*Ga-3* and *Ga-4*) doping concentrations have a different composition. *Ga-1* and *Ga-2* consist solely of SiC, merely of 3C and 6H-SiC with additional small amounts of the polytype 4H. In *Ga-3* and *Ga-4* besides 3C and 6H-SiC a foreign species was found: Si in the fcc configuration. The presence of multiple polytypes in the Ga-doped SiC powder raises an interesting new question, whether the Ga-induced defects are located in the cubic phase, in a hexagonal one or maybe in both. This would require further investigation. Also, the comparison of the powder patterns suggest that higher doping concentrations lead to slightly more hexagonality, as the 6H peaks are more pronounced and also the polytype 4H is present in the samples with high doping concentrations. The XRD results, where a signal originating from elemental Si was only found for *Ga-3* and *Ga-4*, agrees with the observations from optical microscopy and the EDX analysis from SEM very well. This is because these round and dome-shaped particles (see figure 3.14. f and g and figure 3.16.), which were identified as Si by EDX measurements, were only found in the samples *Ga-3* and *Ga-4*, but not in the powders with higher doping concentrations. The determination of the surface termination via XPS shows that O-Si-C species are present. Also, partially and fully oxidised Si oxide species, which commonly appear for SiC, as well as graphitic carbon and a fairly weak signal arising from carbonate were found. The fully and partially oxidised Si-O compounds as well as the graphitic carbon were not detected via XRD, which is not surprising for two reasons. Firstly, XRD measurements have a detection limit of ~1wt.%, where no peak above noise can be detected

if a compound is present at concentrations below this level.[181] The second reason is that these compounds are most likely present in an amorphous state, which restricts the detection via XRD measurements.[171]

3.3.3 Hybrid Solar Cells Fabricated with Al-, Ga- and N-doped SiC as Co-Acceptor

3.3.3.1 Characteristics of Solar Cell Devices

Energy Level Diagram

A schematic diagram of the energy levels and charge transport processes of the ternary component solar cells is shown in figure 3.20.[36,38,93,94,182]

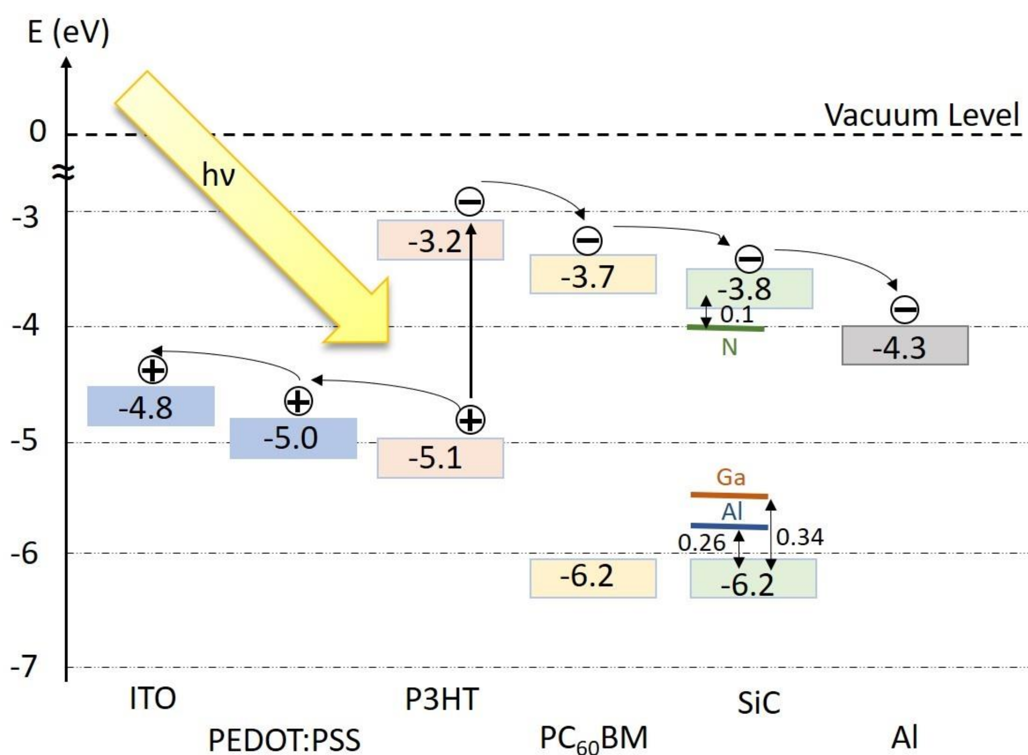

Figure 3.20.: Schematic energy level diagram of the materials used for ternary component hybrid solar cells.

The work function of the hole collecting anode (ITO), the hole transportation layer (PEDOT:PSS), the electron collecting cathode (Al) as well as the HOMO and LUMO level of the organic donor (P3HT) and the organic acceptor ($PC_{60}BM$) and the valence and conduction band energies of the inorganic co-acceptor (SiC, doped with Al, Ga or N) are

shown. The excitons are created in the conjugated polymer upon absorption of the incident light (hν). The holes (indicated by +) move towards the transparent ITO electrode by passing the hole transportation layer. The electrodes (indicated by -) are collected at the Al electrode where they move by passing through the organic, the inorganic or both of the acceptor materials.

Dark I-V Characteristics

In order to investigate the diode behaviour of the solar cells, I-V curves in the dark were recorded. Figure 3.21. shows the characteristics from devices fabricated with 7 different compositions of the active layer (for details see table 3.5.). To make different effects like leakage currents or the charge carrier mobilities of the according devices better visible, the acquired curves were plotted in a semi-logarithmic scale. In reverse bias (V < 0V) at -1 V the binary reference sample *Ref* exhibits a current density of $6.6 \cdot 10^{-4}$ mA/cm^2, which is significantly lower than for all the ternary blend devices. The three devices with 40 wt.% of SiC incorporated in the active layer show current densities of 4.3, 3.0 and 5.5 mA/cm^2 for SiC:Al, SiC:Ga and SiC:N, respectively. The devices with lower SiC concentration have values of 1.2, 1.1 and 0.8 mA/cm^2 for SiC:Al, SiC:Ga and SiC:N and therewith at -1 V a lower current density than the devices with a high SiC concentration. This indicates the presence of leakage currents in devices containing SiC, that appear to not depend on the doping species but on the amount of inorganic material present in the active layer. Between voltages of -0.2 and +0.2 V symmetric ohmic behaviour is found for all different blend compositions. In the intermediate voltage region (V > 0.2 V) the reference sample exhibits the steepest slope. All ternary devices are fairly flat in comparison to the reference. The built-in voltage V_{bi}, which is determined by the difference of the work function of hole- and electron-collecting electrode, separates the intermediate voltage region from the space charge limited current region.[183] In the latter region (V > 1V) the devices are hole dominated because of the higher injection barrier for electrons injected from the cathode (Al) to the LUMO/ conduction band level of the acceptor materials than for holes injected from the anode (ITO) via the PEDOT:PSS to the HOMO of the donor material. There are no significant differences between the slopes of all devices, leading to the assumption that the mobility of the majority charge carrier mobilities (holes) are comparable for all of them. This observation is conclusive, as the hole mobility is dominated by the organic components, but not by the inorganic SiC.[184]

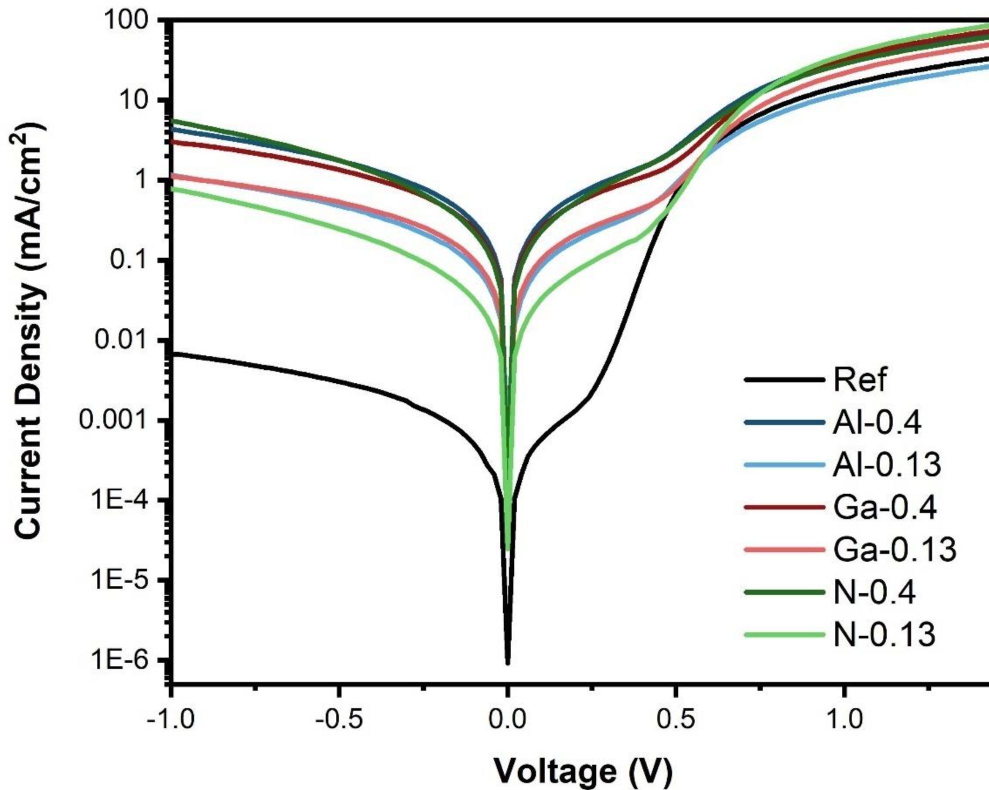

Figure 3.21.: Semi-logarithmic plots of the I-V characteristics of a representative device of the organic binary reference and the 6 ternary hybrid devices recorded in the dark.

Light I-V Characteristics

For investigation of the effect of the two weight ratios of three different co-acceptors on the photovoltaic properties, I-V curves were recorded. In figure 3.22. characteristics recorded under AMG1.5 conditions derived from the solar cells with 7 different active layer compositions are depicted.

The organic binary device *Ref* (black) shows the highest V_{OC} of 0.56 V and best rectangularity (resulting in a high FF) of the I-V characteristics. The J_{SC} of ternary-component hybrid devices with high and low concentrations of Ga-doped (dark and light red) and N-doped SiC (dark and light green) is comparable to the one of *Ref,* exhibiting values of about -4 mA/cm^2.

It can be seen that the best values for the J_{SC} with nearly -5 mA/cm^2 are reached by *Al-0.4* (dark blue) and *Al-0.13* (light blue). The situation is the other way around for high and low concentrations of Al-doped SiC, where the V_{OC} of the *Ga-0.4* and *N-0.4* is clearly lower than for *Ga-0.13* and *N-0.13*. An increasing content of SiC leads to a poorer FF for

solar cells fabricated with SiC:Ga and SiC:N as co-acceptor which appears not to be the case for SiC:Al.

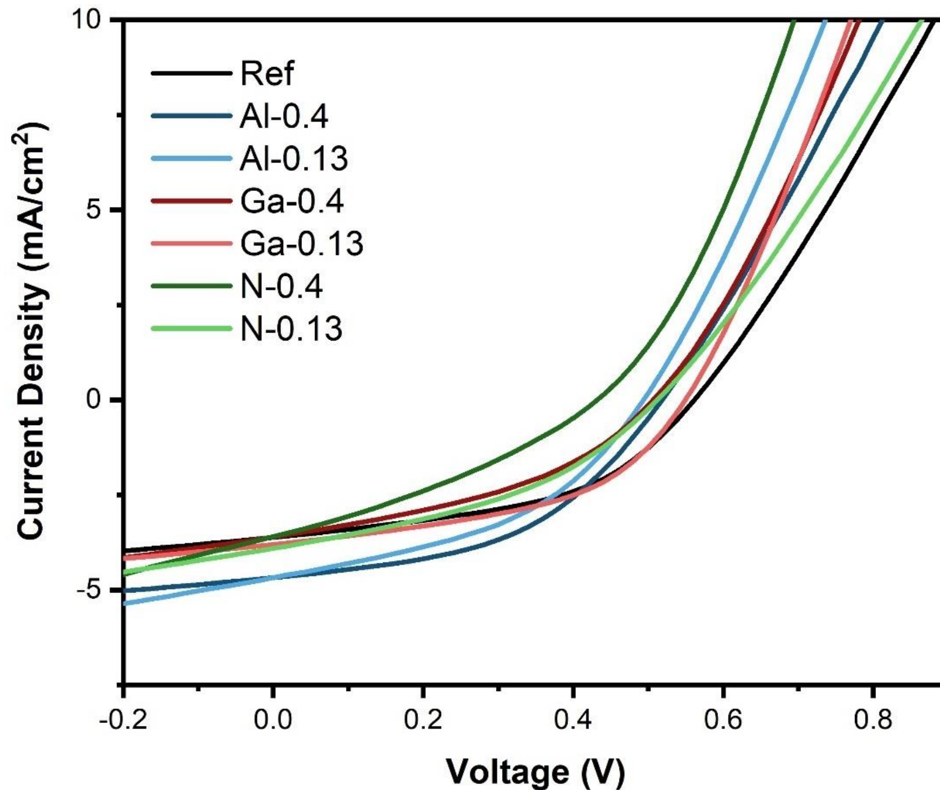

Figure 3.22.: Photocurrent characteristics recorded under AM1.5G illumination from the organic reference and the 6 different hybrid devices. For each active layer condition, a representative device was chosen.

A comparison of the key parameters characterizing solar cells, namely V_{OC} (black), J_{SC} (red), FF (blue) and PCE (green) derived from the devices with 7 different compositions of the active layer is shown in figure 3.23. in order to make changes of the latter better visible. The values were extracted or calculated from the corresponding I-V characteristics of at least 18 devices per condition and averaged over each different blend composition.

In the following the values extracted from the organic binary reference devices will be utilized to demonstrate the impact of the lower fraction (13 wt.%) of the three different co-acceptors on the key parameters. Further, the differences observed for high and low co-acceptor fraction for the devices fabricated with three differently doped SiC crystallites will be discussed.

The reference devices show a V_{OC} of 0.54 V, a J_{SC} -3.88 mA/cm^2 of, an FF of 41% and a PCE of 1.74%. The V_{OC} is with values of 0.49 V for *Al-0.13* and 0.52 V for *N-0.13* slightly

lowered in comparison with *Ref*, indicating the presence of loss mechanisms like charge carrier recombination. These minor losses probably occur due to the presence of trap states at the surface of the SiC crystallites.[185] Only *Ga-0.13* reaches the same value as obtained for *Ref*. *Al-0.13* and *N-0.13* exhibit J_{SC} values of -4.95 and -4.34 mA/cm^2, respectively, which is a clear enhancement of the generated photocurrent in comparison to *Ref*. However, *Ga-0.13* with -3.78 mA/cm^2 is slightly below *Ref*. The improvement of the J_{SC} can be attributed to the higher electron mobility of SiC in comparison to $PC_{60}BM$. When comparing the FF only small deviations from the value obtained can be found, *Al-0.13* has a value of 41%, *Ga-0.13* 42% and *N-0.13* 40%. As this value stays stable it seems likely that the charge transfer in these blends works comparable sufficient. This results in increased PCEs in comparison to *Ref* of 2.25% for *Al-0.13* and 1.8% for *N-0.13*. *Ga-0.13* with 1.74% reaches the same PCE as *Ref*.

When comparing high (40 wt.%) and low (13 wt.%) co-acceptor fractions it is most notable that low fractions show a clearly higher PCE than high fractions independent of the doping material used. *Al-0.4* reaches 2% and thereby exceeds the PCE of *Ref*. *Ga-0.4* and *N-0.4* with a PCE of 1.26% and 1.08%, respectively, remain clearly below. This originates from a reduction of the generated photocurrent and the open circuit voltage for higher acceptor fractions for all co-acceptor materials. As mentioned above on the SiC surface, like for many other inorganic materials, trap states are present. Due to more SiC in the active layer more traps are present, which explains the lowered V_{OC}. The observed lowering in J_{SC} leads to the assumption that higher co-acceptor fractions are not beneficial for the morphology. Agglomerations of SiC particles have a negative influence on the desired phase separation of donor phase as well as the acceptor phases. It leads to a hindering of the created excitons to reach the donor acceptor interface within their diffusion length (10 – 20 nm).[77] The FF is also distinctively increased for lower amount of Ga-doped and N-doped SiC but shows only a slightly higher value for *Al-0.4* in comparison to *Al-0.13*.

These results show that Al-doped SiC is the most suitable co-acceptor, as both high and low acceptor fraction lead to an increased PCE in comparison to *Ref,* which is dominated by a massive rise in J_{SC} and a subtle improvement of the FF. Interestingly, no correlation between n- and p-doped SiC was found.

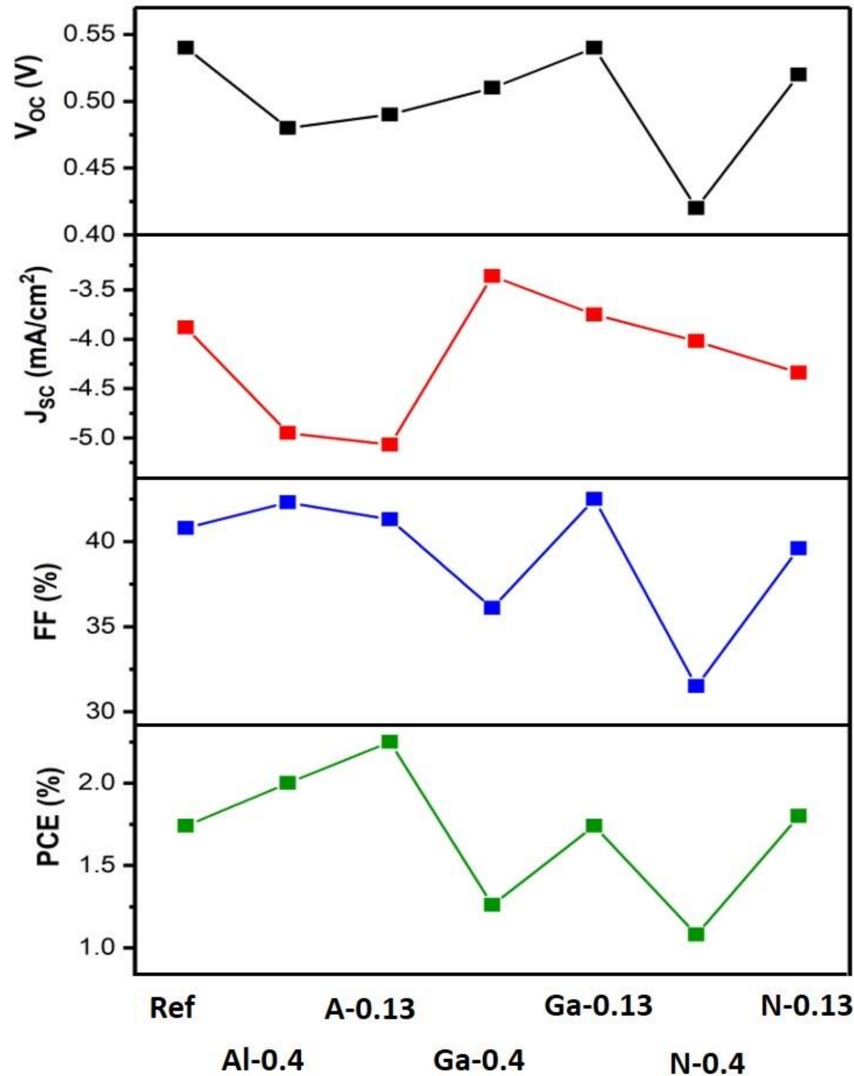

Figure 3.23.: Summary of the averaged key values V_{OC} (black), J_{SC} (red), FF (blue) and PCE (green) of the devices fabricated with 7 different active layer compositions.

Spatially Resolved Photocurrent Maps

To investigate local distribution of the photocurrent and see which impact the different dopants and especially the concentration of SiC as co-acceptor on the blend morphology has, LBIC measurements were performed. The scans were acquired using a focused laser diode with a wavelength of 532 nm. Spatial photocurrent maps were obtained by scanning across the whole device active area of 6 mm^2 with a step size of 25 µm. As SiC:Al and SiC:Ga have a similar surface termination, spatially resolved device characteristics of solar cells fabricated with high and low concentration of Al- and Ga-doped SiC as co-acceptor are illustrated in comparison with *Ref* in figure 3.24. The relative photocurrent J_{rel} is pictured by a colour scale ranging from black for no detectable photocurrent, to dark red for the highest

current output. The relative photocurrent is normalized to the highest value detected for each device.

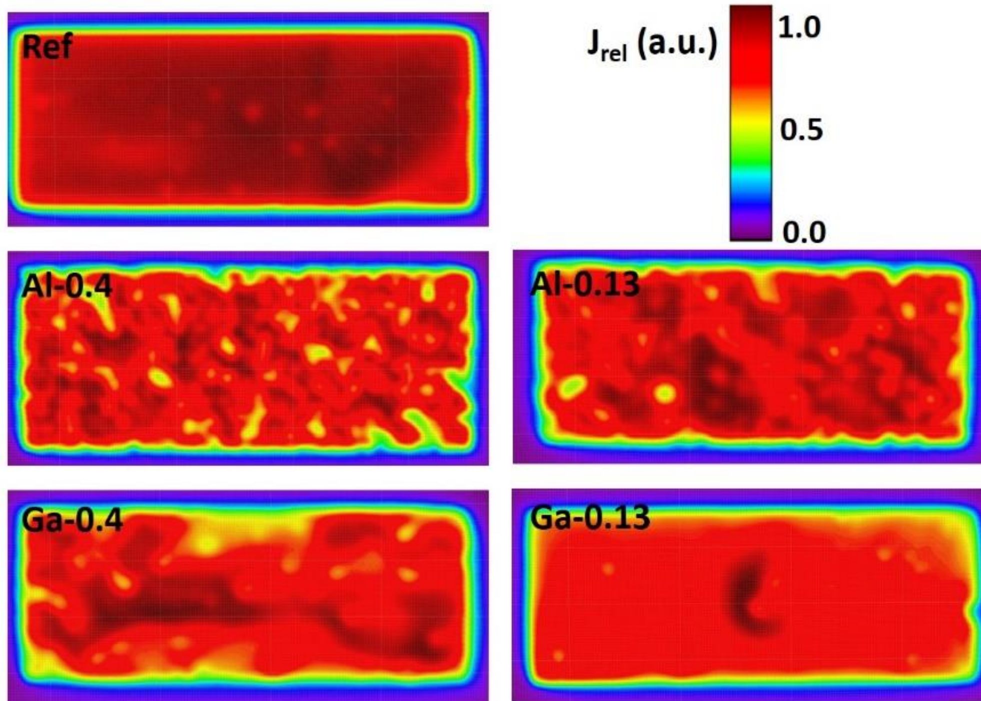

Figure 3.24.: Illustration of spatially resolved photocurrent maps of *Ref*, *Al-0.4*, *Al-0.13*, *Ga-0.4* and *Ga-0.13*.The current was normalized to the highest value obtained from each device.

The organic binary reference device (*Ref*) appears very smooth, in dark red over the majority of the device active area. Small dot shaped areas with 75% of the maximum photocurrent can be found randomly distributed all over the device which are probably originating from agglomerations of the hole transportation layer (PEDOT:PSS). The lower right corner also shows a lowered current outcome of about 60%. The picture drastically changes when having a look at the photocurrent maps recorded from the ternary hybrid devices. As expected, the morphology of the SiC has a large impact on the local photocurrent output. For *Al-0.4* the colour map appears very inhomogeneous, with local, small areas of high (100%, dark red) and medium (50%, yellow) photocurrent randomly distributed between areas of an output of about 70% (light red). At the edges and close to the borders also some areas with about 40% of the maximum photocurrent generated in this device were detected. *Al-0.13* appears a bit smoother, where still dark red photocurrent hot spots and yellow areas appear in-between light red, but the single parts of different photocurrent generation are becoming larger. Also, here at the border areas, regions with about 40% output were found.

The yellow and green areas are likely to originate from inhomogeneities in the active layer originating from agglomerations of SiC crystallites. The photocurrent map derived from *Ga-0.4* again consists of areas coloured in dark red, light red and yellow, but in comparison to *Al-0.4* the different areas are clearly larger in extend where in the borders of the device the performance shows a larger drop. *Ga-0.13* exhibits, however, a very smooth image with the majority of the device active area producing a J_{rel} of about 75%. In the middle just one hot spot (coloured in dark red) with 100% performance appears. Randomly distributed but fairly small yellow areas with lowered performance can also be observed.

3.3.3.2 Photophysics and Photoresponse

UV-vis Absorption

The impact that incorporation of Al-, Ga- and N-doped SiC has on the absorption properties of P3HT:PC_{60}BM thin films was investigated by UV-vis spectroscopy. The normalized spectra recorded in a wavelength range between 380 nm and 800 nm from the organic binary and the 6 different hybrid ternary thin films are shown in figure 3.25. All spectra exhibit a similar shape consisting of three vibronic features which is the signature shape of P3HT originating from the delocalized π-electrons: a main peak located at about 510 nm (0-2) and two shoulders at about 550 nm (0-1) and 600 nm (0-0).[186] For the reference sample the main peak is located at 512 nm. The absorption maxima of the thin films fabricated with low SiC concentrations are located at 512 nm for *Al-0.13* and at 510 nm for *N-0.13* and *Ga-0.13* and are at the same position or very close to *Ref*. In comparison the spectra recorded from films with 40 wt.% SiC show a shift to the higher wavelength range with values of 514 nm, 515 nm and 517 nm for *N-0.4*, *Ga-0.4* and *Al-0.4*, respectively. *Al-0.13* exhibits the same shape as *Ref* in the region around the shoulder at about 550 nm and has a slightly higher absorbance at the shoulder at around 600 nm. *Ga-0.13* and *N-0.13* in comparison have a lower absorbance at both shoulders. All three samples with the higher SiC concentrations are clearly more pronounced at the 0-0 and the 0-1 feature and also show broadening in this wavelength range. The absorbance exhibits the largest values for *Al-0.4* and *Ga-0.4*. The rise in relative intensity of the 0-0 peak for high SiC concentrations can be assigned to better polymer chain packing.[187] The peak broadening and the resulting enhanced absorbance in this wavelength region for samples with the higher co-acceptor load can be explained by the SiC crystallites acting as scattering centres in the active layer leading to the enhancement of the optical path length of the incident light.[188] However, the relative rise in intensity for the

0-0 and 0-1 feature as well as the peak broadening do not appear for incorporation of low quantities of SiC into the films. No clear trend for the absorbance concerning the dopants used was found

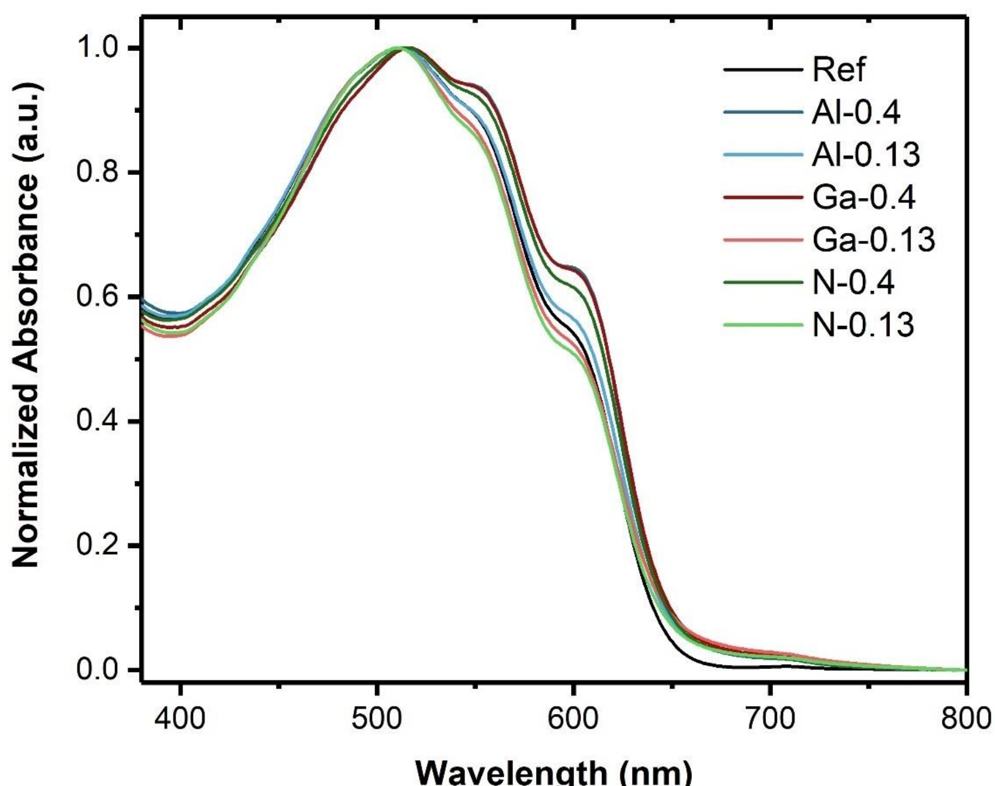

Figure 3.25: Normalized UV-vis spectra recorded from thin films with 7 different compositions.

This behaviour is not surprising for two reasons: Firstly, the absorption of SiC compared to the one of P3HT is rather low as it is an indirect bandgap semiconductor and therefore would be superimposed by the strong absorption originating from the conjugated polymer.[149] The other reason is that SiC has an absorption onset in the visible range starting at the wavelength corresponding to the bandgap (see figure 3.20.), which lies at 579 nm for SiC:Al, at 602 nm for SiC:Ga and at 539 nm at SiC:N, but most of the absorption, however, takes place in the ultraviolet wavelength range.[35,150]

Photoluminescence and Quantum Yield

For recording the PL all samples were excited at a wavelength of 512 nm. The normalized PL spectra are displayed in figure 3.26. in a wavelength range between 550 nm and 950 nm.

The spectra exhibit a shape that is very similar to each other with a main peak at about 720 nm (0-0 peak) and a shoulder at about 660 nm. While the shoulder shows the same intensities for *Ref*, *Al-0.13* and *N-0.13*, it shows higher intensities between 650 nm and 680 nm for both *Ga-0.4* and *Ga-0.13*. *Al-0.4* and *N-0.4* have an even more pronounced 0-1 feature not only in the latter wavelength region but also in the onset of the 0-0 and 0-1 peak.

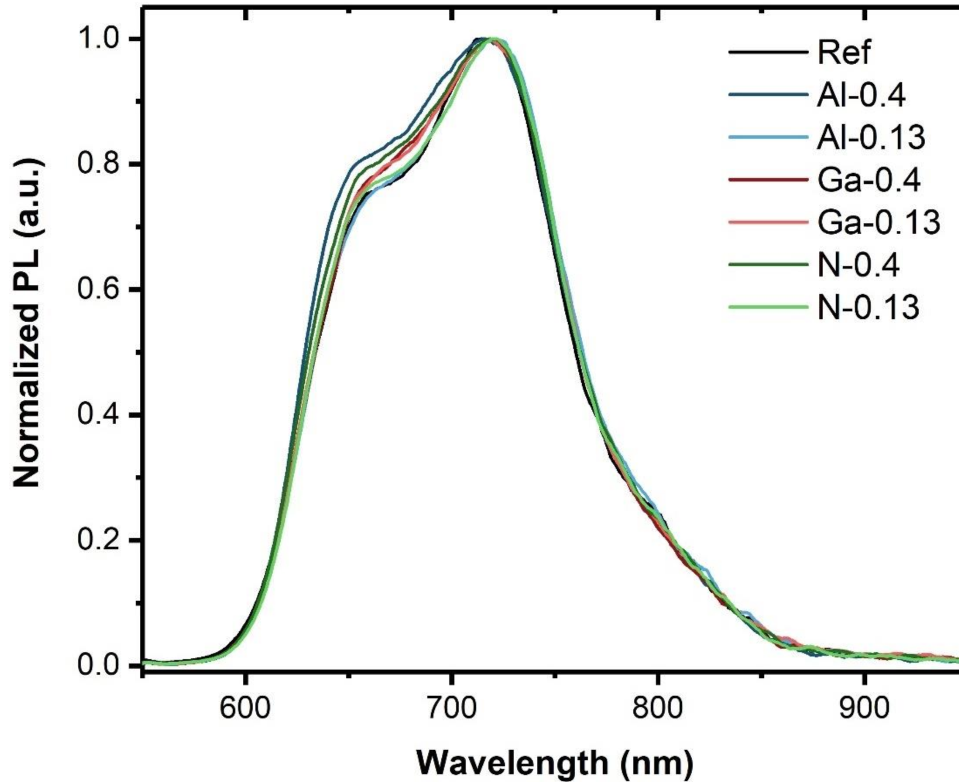

Figure 3.26: Normalized PL spectra recorded at an excitation wavelength of 512 nm.

The noise in the signal that appears for wavelengths between 650 nm and 700 nm and for wavelengths larger than 800 nm is an artefact of the measurement.

To investigate the impact on the emission QY of differently doped SiC added in high and low concentration to P3HT:$PC_{60}BM$ thin films, the samples were excited at their respective maximum in absorbance. The excitation wavelength and recorded QYs are summarized in table 3.6. For a P3HT only thin film a QY of 4.35% was reported previously.[153] As quenching is a measure for the exciton diffusion at the donor acceptor interface this value is desired to become lower when a suitable acceptor is blended with the conjugated polymer. Quenching works best when $PC_{60}BM$ is added in a 1:1 ratio, resulting in a QY of 0.17%. For *Al-0.13*, *Ga-0.13* and *N-0.13* the values reach 0.23%, 0.19% and 0.22%, respectively and are

therefore higher than for *Ref*. For the higher SiC concentration in the blends 0.28%, 0.20% and 0.22% are recorded from *Al-0.4*, *Ga-0.4* and *N-0.4*, respectively. This increase in QY with increasing SiC content can be explained by the partially large SiC crystallite size compared to the exciton diffusion length of about 20 nm, which does not allow all of the electron hole pairs to reach the donor acceptor interface before recombination takes place. When comparing the QYs according to the different dopants in SiC, it can be seen that Ga leads to the lowest values derived from ternary component blends. This is an indication for less surface traps in comparison to SiC:Al and SiC:N which results in less trap assisted recombination.

Table 3.6.: Summary of the quantum yields and respective excitation wavelengths.

Name	λ_{ex} (nm)	QY (%)
Ref	512	0.17
Al-0.4	517	0.28
Al-0.13	512	0.23
Ga-0.4	515	0.20
Ga-0.13	510	0.19
N-0.4	514	0.26
N-0.13	510	0.22

External Quantum Efficiency

As the EQE is the J_{SC} per wavelength it can give valuable information about the device physics. The recorded EQE curves, displayed in a wavelength range between 420 nm and 800 nm, are shown in figure 3.27. To allow better comparison the curves were normalized.

As can be seen from the EQE curve recorded from the reference sample a broad peak between 480 nm and 650 nm is visible, indicating the photocurrent produced by P3HT. When having a closer look at the shape, three not very pronounced vibronic absorption shoulders can be observed at about 512 nm, 550 nm and 600 nm, which can be ascribed to the conjugated polymer P3HT. The main peak at about 512 nm originates from the absorption of the main chain where the two other features appear due to interchain interaction of the ordered crystalline regions of the thin films.[189,190] This general shape was also found

for all ternary component devices with some deviations. Interestingly a peak narrowing of both Ga-doped devices compared to all other devices was found appearing most distinct for *Ga-0.13*. For both nitrogen-doped devices, the peaks are very similar and show a slight peak broadening compared to *Ref*. For the Al-doped solar cells the peak broadening becomes even more pronounced, leading to a flattened shape due to the peak at about 600 nm becoming nearly as strong as the main feature at about 512 nm. The increased peak broadening of the EQE appears most distinct for devices fabricated with SiC:Al and SiC:N as co-acceptor and match well with the increased photocurrent generation in comparison with *Ref*, as was also found from the averaged values obtained from the light I-V characteristics (compare figure 3.23.).

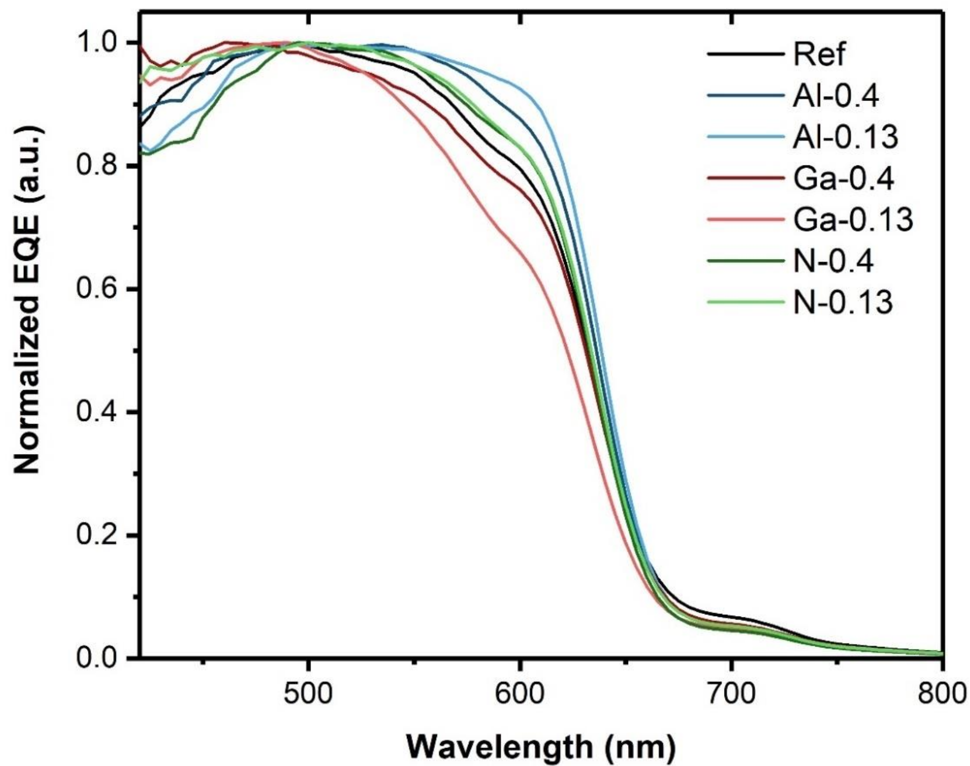

Figure 3.27: Illustration of the normalized EQE curves derived from the solar cells with 7 different active layer compositions.

The values of the EQEs for the different active layer compositions were extracted from the not normalized curves (not shown). The highest value appears for *Ref* with close to 60%.The values derived from devices with lower SiC concentrations are 55% for *Al-0.13* and 50% for *Ga-0.13* and *N-0.13*. For higher doping concentrations a further drop in EQE with 50% for *Al-0.4* and 45% for *Ga-0.13* and *N-0.13* was detected. The EQE appears to generally be enhanced for devices fabricated with Al-doped SiC compared to Ga and N which is consistent with the results of the I-V measurements as well (see section 3.3.3.1).

3.3.4 Conclusions

In the first part of this chapter an investigation of the morphology and surface termination of sol-gel derived Ga-doped SiC powder samples with 4 different doping concentrations (5%, 2.5%, 1.25% and 0.514%) is presented. EPR X-band spectra show a concentration dependent structureless signal at 2.0034 ± 0.0003. The EPR intensity and obtained defect densities correlate with the nominal doping concentration of the samples, which suggests that the defects are caused by the dopant species. However, the signal itself is likely to originate from lattice distortions caused by the Ga atoms. Optical microscopy and SEM images revealed that the crystallite sizes tend to become smaller with lower doping concentrations and also the colouring gets lighter. The observed colour change matches well the EPR results. In the samples *Ga-3* (1.25% doping) and *Ga-4* (0.514% doping) drop shaped grey particles were found, which were identified as elemental Si by EDX. Furthermore, XRD measurements showed that *Ga-1* (5% doping) and *Ga-2* (2.5%) doping consist mainly of the polytypes 3C and 6H with trace amounts of 4H. However, for *Ga-3* (2.5% doping) and *Ga-4* (0.514% doping) a different constitution of the powder samples was found. The major part also consists of 3C and 6H-SiC but no matches for the pattern of 4H were found. Instead, the fcc configuration of elemental Si was detected. Si 2p XPS core level spectra showed that the main contribution on the surface is independent of the nominal Ga doping concentrations of SiC. Also, Si-O-C compounds were found in all samples as well as minor quantities of intermediate oxide species Si-O_x. C 1s core level spectra showed a strong termination of the surface with graphitic carbon, and aside from the expected but rather small SiC contribution, minor peaks originating from C-O and O-C=O bonds.

A study on the impact on the solar cell performance and photophysics of the incorporation of high (40 wt.%) and low (13 wt.%) concentrations of Al-, Ga- and N-doped 3C-SiC powder (all with 5% doping concentration) into organic binary blend devices was conducted.

I-V measurements performed in the dark evidence the presence of leakage pathways for all ternary component devices. Illumination with a solar simulator (AM1.5G conditions) reveals that devices fabricated with SiC:Al as co-acceptor in high (40 wt.%) as well as low concentration (13 wt.%) have the best performance even exceeding the one of the organic binary devices acting as reference. Blending with Ga- and N-doped SiC leads for low concentrations to very similar PCEs compared to *Ref* and clearly lower ones for high

concentrations. In general, solar cells fabricated with low SiC concentrations exhibited better performances than high ones. Spatially resolved photocurrent maps show that the blend homogeneity suffers when SiC is incorporated into organic binary blends This is less pronounced for SiC:Ga as co-acceptor in comparison to SiC:Al. Measurements of the absorbance indicate a disturbance of the molecular order of P3HT for high SiC concentrations. No contributions of the SiC were detected, but peak broadening for ternary component blends with high SiC loads lead to the assumption that SiC particles act as scattering centres. Investigations of the QY showed sufficient quenching of all 7 active layer compositions in comparison to P3HT only films, with the lowest QY detected for *Ref*. The EQE exhibits with 60% the highest value for *Ref*, followed by 55% for *Al-0.13*. The EQEs tend to differ by 5% between high and low concentrations of the same doped SiC in the active layer.

As the use of SiC particles as inorganic co-acceptor in organic binary solar cells is a novel approach, no comparison of different result from the same materials used for device fabrication can be made. From the present results the increase in PCE can be attributed to the high electron mobility of the SiC which supports a higher J_{SC}. Another system where inorganic nanoparticles were incorporated into a P3HT:PCBM matrix which benefits from the good transport properties of the inorganic co-acceptor was reported by Lefrançois et al. In 2015 they published an article where they demonstrated an increased efficiency from 0.81% for P3HT:PC_{60}BM to 1.6% for the ternary component system using $CuInS_2$ nanocrystals with a size of 7.4 nm. The increased efficiency originated from an elevated J_{SC}, where no contribution of the inorganic co-acceptor to light harvesting in the visible wavelength range was found.[191] Kim et al. reported the improvement of the device efficiency by embedding Ag-nanowires in a P3HT:PC_{60}BM matrix. The use of nanowires resulted in an increased absorbance of light in the film due to scattering events and localized surface plasmon resonance.[192] These examples show that there are different classes of inorganic materials which are suitable for the use in organic inorganic hybrid solar cells, where their unique properties support a better overall efficiency.

4 General Conclusion and Outlook

4.1 General Conclusions

In the scope of this thesis, SiC was fabricated via a sol-gel based carbothermal reduction route where three different dopants, namely Al, Ga or N, were incorporated within the wet chemical stage of the process. The thesis has two main focuses, the first being the characterisation of the synthesized powder samples in terms of polytype composition, and further, bulk and surface properties. The methods applied for this purpose include optical and scanning electron microscopy. XRD and Rietveld refinement of the diffraction patterns as well as XPS and RAIRS. EPR measurements were carried out on Ga-doped SiC to evaluate the defect type and density.

The second focus is set on the novel approach of using SiC as co-acceptor in ternary component hybrid solar cells. The devices were based on the well-researched organic material combination P3HT:PC_{60}BM, as the energy levels of SiC is suiting to the ones of the organic donor and acceptor material. SiC crystallites doped with three different impurity atoms were incorporated in the organic matrix in different weight fractions. The solar cells were characterized in terms of device physics in the dark and under illumination (AM 1.5G). Further, morphological characterisations were carried out via LBIC measurements and the photophysics was investigated via UV-vis spectroscopy, photoluminescence measurements and determination of the EQE. Additionally, transient absorption measurements gave insights into the transport dynamics of the generated charge carriers.

In the first chapter (3.1) as-synthesized Al- and N-doped SiC powder samples (5% nominal doping) were characterized according to bulk and surface properties. This yielded interesting insights on the effect that the doping species has on the properties of the material. Rietveld refinement of the powder diffraction patterns revealed a dopant dependent phase composition. SiC:N consists of 93% of 3C-SiC and 7% 6H-SiC. The Al-doped SiC consists of 53% of the polytype 3C, 37% 6H and 10% 4H. The surface composition was revealed to be also dependent on the doping species. The N-doped sample shows SiO_2 layers on the surface which is a typical observation for SiC and a weak signal arising from defect carbon. The situation for SiC:Al looks very different. Here, Si-H bonds were found, graphitic carbon and small traces of aluminium carbonate. These differences most likely appear due to the fact that Al is much more reactive than N. Also, the formed carbonate (which is known to

be not stable in ambient environment) is likely to be present at the SiC-graphene interface and helps to stabilize the surface graphite.

The second experimental chapter (3.2) examines the replacement of the organic acceptor $PC_{60}BM$ in 20 wt.% steps by nitrogen-doped SiC in organic P3HT:$PC_{60}BM$ solar cells. The evolution of the devices characteristics was observed in comparison with binary organic reference devices.

TEM observations of a lamella extracted from a thin film indicated that $PC_{60}BM$ tends to cover the SiC crystallites. The trend of the crucial solar cell parameters (V_{OC}, J_{SC}, FF and PCE) derived from the averaged device characteristics recorded under AM1.5G conditions show that the use of solely SiC as acceptor material is not beneficial for the device performance. With increasing $PC_{60}BM$ content the values of the key parameters increased. A maximum of the charge carrier generation was found when using a $PC_{60}BM$:SiC weight ratio of 4:1. Solar cells fabricated with this acceptor ratio showed an improved PCE of 2.2% in comparison to the organic binary devices having a PCE of 1.6%. The rise in PCE is dominated by a rise in the J_{SC}. The lowered performance observed in devices with a not sufficient amount of $PC_{60}BM$ can be assigned to two reasons. First, trap states present at the surface of the SiC, which trap the created charge carriers and hinder dissociation at the donor acceptor interface. The second reason is the poor interaction of the conjugated polymer with the inorganic semiconductor which probably appears due to wetting problems. Also, no proper network of percolated pathways of the SiC to the hole collecting anode can be formed. A higher $PC_{60}BM$ ratio helps to overcome these problems as the inorganic crystallites are covered better by the organic co-acceptor material. This coating supports the deactivation of the surface traps and therefore makes charge carrier dissociation more efficient and it also improves the formation of the necessary percolation of donor and acceptor phase to allow the collection at the respective electrodes.

The last experimental chapter (3.3) deals with the characterisation of Ga-doped SiC with four different nominal doping concentrations (5%. 2.5%, 1.25% and 0.514%) and the use of SiC:Al, SiC:Ga or SiC:N in a high (40 wt.%) and a low weight fraction (13 wt.%) as co-acceptor in P3HT:$PC_{60}BM$ solar cells.

Measurements of the EPR X-band spectra showed a correlation between the nominal doping and the defect density in the SiC crystal lattice. The defects themselves are most likely of intrinsic nature. All samples consist mainly of the polytypes 3C and 6H, where the samples with higher doping densities additionally have minor quantities of 4H-SiC and samples with lower doping show small amounts of Si fcc. The species present on the SiC:Ga crystallites' surface (besides SiC) are partially oxidized Si-O species, O-Si-C bonds, graphitic carbon and minor quantities of C-O and O-C=O bonds, which do not depend on the doping concentration.

Characteristics obtained from solar cells, where SiC:Al, SiC:Ga or SiC:N were used as co-acceptor, showed that low weight fractions lead to a better device performance than high weight fractions, independent of the SiC dopant. This can be attributed to the tendency of SiC crystallites to agglomerate, which is not beneficial for the desired phase separation, where it is necessary to ensure that the generated charge carriers are able to reach the donor acceptor interface within their lifetime. According to the doping species, Al achieved the best PCE, followed by Ga and N. SiC:Al was the only co-acceptor where low as well as high fractions lead with 2.25% and 2%, respectively, to a higher PCE than the 1.74% measured from the organic binary reference devices. Absorption measurements derived from blends with the differently doped SiC crystallites showed no additional absorption features in comparison to spectra derived from the organic binary blends. What was detected for high fractions of the inorganic co-acceptor, is peak broadening which can be related to SiC crystallites acting as scattering centres in the thin film.

In general, it can be concluded that the termination of the surface as well as the polytype composition of SiC powder samples fabricated via sol-gel synthesis strongly depend on the impurity atoms used for doping. The impact seems to be related to the size of the impurity atoms and the crystal sites that they occupy: N resides on C sites and the samples consist majorly of 3C with traces of 6H. Al and Ga occupy Si sites where larger amounts of the hexagonal polytypes 6H and 4H were detected.

For the use of doped SiC crystallites in hybrid solar cells it can be summarized that the use of the inorganic material as co-acceptor is beneficial for the device performance. A crucial point for the device performance which was observed is a balanced weight ratio between the

organic and inorganic acceptor material, which allows the complete coverage of the inorganic SiC by the organic $PC_{60}BM$. This deactivates the traps present on the SiC surface and forms a percolation to the hole collecting anode. To benefit from the good charge transport properties of the SiC, size selection of the grown crystallites is required as otherwise the extension of the phases would not properly support the generated charge carrier to reach the donor acceptor interface before recombination takes place.

4.2 Outlook

For further research on the topic of ternary component hybrid solar cells with SiC as co-acceptor, it would be of high interest to try other polymers as donor material. In this work trap states on the crystallites and agglomeration of particles was observed. A path to improve this would be to study the effect of depositing ligands on the surface which would deactivate these traps and thereby improve device performance. Another interesting approach would be the down conversion of the crystallite size below the exciton Bohr radius as light harvesting would benefit from it due to the bandgap tuning based on the quantum confinement effect.

Therefore, further research could concentrate on size control during synthesis by adapting the growth conditions at the different steps of the sol-gel process as well as during the carbothermal reduction of the quartz glass or via template-assisted growth of the material.

It would also be of high interest to create ordered structures of SiC within the organic matrix to control phase separation and thereby ensure that the created excitons are able to reach the dissociation sites.

Another possible path would be to improve polaron formation by incorporation of metal impurities. It was reported in literature, that this can be highly beneficial for the device performance in terms of polaron formation. This indicates, that metal impurities in SiC would exhibit extraordinary properties from which solar cells can benefit.

5 ANNEX

5.1 List of Abbreviations and Acronyms

AE	Auger electrons
Al	Aluminium
α-SiC	SiC in a rhombohedral or hexagonal configuration
Å	Ångstöm
B	Boron
B4C	Boron carbide
BHJ	Bulk heterojunction
BSE	Backscattered electrons
β-SiC	SiC in the cubic configuration
C	Carbon
C_{60}	Buckminster fullerene
CdS	Cadmium sulfide
CdSe	Cadmium selenide
CdTe	Cadmium teluride
CIGS	Copper Indium gallium selenide
CVD	Chemical vapor deposition
CH_3	Methoxy group
C_2H_2	Acetylene
C_2H_5	Ethoxy group
EDX	Energy dispersive X-ray spectroscopy
EELS	Electron energy loss spectroscopy
EPR	Electron paramagnetic resonance
EQE	External quantum efficiency
ETL	Electron transport layer
FF	Fill factor
FIB	Focused ion beam
FTO	Fluorine doped tin oxide
Ga	Gallium
GaN	Gallium nitride
HfC	Hafnium carbide
HO	Hydroxyl group
HOMO	Highest occupied molecular orbital
HTL	Hole transport layer
IC	Internal conversion
ICBA	Indene-bisaduct
IPA	Isopropanol
IR	Infrared
ITO	Indium tin oxide

J_{SC}	Short circuit current density
LBIC	Light-beam induced current
LED	Light emitting diode
LiF	Lithium fluoride
LUMO	Lowest unoccupied molecular orbital
MoO_3	Molybdenum trioxide
mpp	Maximum power point
N	Nitrogen
OR	Alkoxy group
P	Phosphor
P3HT	Poly-3-hexylthiophene
PbS	Lead(II) sulfide
$PC_{60}BM$	[6,6]-phenyl-C61-butyric acid methyl ester
PCE	Power conversion efficiency
PCPDTBT	poly[2,6-(4,4-bis-(2-ethylhexyl)-4H-cyclopenta[2,1-b;3,4-b']dithiophene)-alt- 4,7-(2,1,3-benzothiadiazole)]
PEDOT:PSS	poly(3,4-ethylenedioxythiophene)-poly(styrenesulfonate)
PL	Photoluminescence
QY	Quantum yield
RAIRS	Reflection absorption infrared spectroscopy
ROH	Alcohol
SE	Secondary electrons
SEM	Scanning electron microscopy
Si	Silicon
SiC	Silicon carbide
SiH_2Cl_2	Dichlorosilane
SiOC	Oxycarbide
Si-O-Si	Siloxane
TEM	Transmission electron microscopy
TEOS	Tetraethoxysilane
TiC	Titanium carbide
TMOS	Tetramethoxysilane
V_{OC}	Open circuit voltage
VR	Vibrational relaxation
WC	Tungsten carbide
WDX	Wavelength dispersive X-ray spectroscopy
XRD	X-ray diffraction
ZrC	Zirconium carbide

5.2 List of Tables

Table 1.1.: Summary of the properties of the SiC polytypes 2H, 4H, 6H and 3C. 3

Table 1.2.: Summary of the most important physical and chemical properties of the SiC polytypes 4H, 6H and 3C. 6

Table 3.1.: Summary of the sample denotations and blend compositions. 67

Table 3.2: Summary of the averaged values of the key parameters obtained for the different active layer compositions. 74

Table 3.3.: Summary of the obtained quantum yields and respective excitation wavelength λ_{ex} for the blend films with changing acceptor composition. 81

Table 3.4.: Nomenclature and nominal doping concentrations of the 4 different Ga-doped powder samples. 88

Table 3.5.: Summary of the sample names for different device conditions and according dopants and blend compositions. 89

Table 3.6.: Summary of the quantum yields and respective excitation wavelengths. 114

5.3 List of Figures

Figure 1.1.: Illustration of the unit cells and stacking sequences of the three most common polytypes of SiC. 4

Figure 1.2.: Illustration of a Lely platelet (left) and a schematically depicted truncated tetrahedron (right). 5

Figure 1.3.: Energy level diagram of commonly used dopants in SiC-polytypes 3C (green), 4H (red) and 6H (blue). 9

Figure 1.4.: Illustration of the process of pore contraction by the formation of bridging bonds. 13

Figure 1.5.: Schematic diagram of the different steps of a sol-gel process and the different final products. 15

Figure 1.6.: Illustration of the progress and current solar cell efficiencies of various technologies. 18

Figure 1.7.: Illustration of the backbone of a conjugated polymer with alternating single and double bonds. 19

Figure 1.8.: Molecular structure of P3HT (left) and PCPDTBT (right). 20

Figure 1.9.: Molecular structure of the Buckminster fullerene (left) and two of its derivatives PC61BM (middle) and ICBA (right). 21

Figure 1.10.: Overview of the energy levels of commonly used organic and inorganic materials used in organic and hybrid photovoltaics. 22

Figure 1.11.: Schematic illustration of single layer devices (left), double layer devices (middle) and devices in the BHJ geometry (right). 24

Figure 1.12.: Schematic illustration of the basic steps for photoinduced charge carrier generation in an organic BHJ device. 26

Figure 1.13: Illustration of weakly bound Mott-Wannier excitons and tightly bound Frenkel excitons. 27

Figure 2.1: Schematic illustration of the different process steps involved in the sol-gel based carbothermal reduction synthesis of SiC. 31

Figure 2.2: Schematic illustration of the pixelated anode substrate (left) and photograph of a solar cell device (right). 32

Figure 2.3: Schematic illustration of bright field imaging (left) and dark field imaging (right). 34

Figure 2.4: Schematic depiction of the information depth and lateral extension of an electron beam with a sample and the origin of different signals (AE: Auger electrons, SE: Secondary electrons, BSE: back scattered electrons, X: X-ray radiation). 35

Figure 2.5 Illustration of the different kinds of scattering arising from a thin specimen. 37

Figure 2.6: Schematic illustration of the low-loss region (a) and the core-loss region (b) of a typical EELS spectrum. 38

Figure 2.7: Schematic depiction of an EPR experiment. 39

Figure 2.8: Illustration of Braggs law, where d is the distance between two adjacent net planes and θ the incident angle. 40

Figure 2.9: Schematic depiction of an X-ray diffractometer in Bragg Brentano geometry. 41

Figure 2.10: Schematic illustration of the emission of photoelectrons after excitation with X-rays. 42

Figure 2.11: Measurement of reflection absorption where α is the angle of incidence. 44

Figure 2.12: Illustration of typical I-V curves recorded in the dark and under ilumination, plotted linear (a) and semi-logarithmic (b). 46

Figure 2.13: Schematic illustration of two photocurrent responses to a square light pulse, the upper one without a transient photocurrent and the lower one with. 48

Figure 2.14: Schematic illustration of LBIC set-up and a resulting photocurrent map. 49

Figure 2.15: Schematic illustration of the Franck-Condon principle. 50

Figure 2.16: Schematic depiction of the processes behind PL on the basis of the Jablonski diagram. 52

Figure 3.1: SEM image of SiC nano-crystallites after sedimentation separation. 68

Figure 3.2.: HAADF STEM image (left) and elemental maps extracted from the EELS spectra of an exemplary region of a *b4* lamella (right). 69

Figure 3.3.: Elemental maps derived from plasmon loss peaks of the ternary blend, where black and blue shows SiC, green $PC_{60}BM$ and red to yellow P3HT. 70

Figure 3.4.: Optical microscopy images of the devices *b6* and *b5*. 71

Figure 3.5.: Semi-logarithmic plot of the I-V characteristics recorded without illumination for devices with decreasing SiC acceptor fraction, from 100 wt.% SiC (*b1*) to no SiC (*b6*). 72

Figure 3.6.: Light I-V characteristics of devices with decreasing SiC acceptor fraction from 100 wt.% (*b1*) to 0 wt.% (*b6*), recorded under AM 1.5G conditions. 73

Figure 3.7: Illustration of the evolution of solar cell key parameters with changing SiC content in the devices. 74

Figure 3.8.: EQE curves as recorded (left) and normalized (right) of devices *b1* to *b6*. 78

Figure 3.9.: Normalized absorbance (left) and PL spectra (right) of film samples of *b1* to *b6* on quartz. 80

Figure 3.10.: Photograph of the devices *b1* and *b2* illuminated by an UV-lamp. 81

Figure 3.11.: Spatially resolved photocurrent maps of devices with blend compositions *b1* to *b6*, normalized to the highest obtained LBIC current of all 6 types, gained from *b5*. 82

Figure 3.12.: Transient photocurrent curves of the devices *b2 – b6*, normalized to the steady state photocurrent at 200 µs, recorded at different applied bias voltages. 85

Figure 3.13.: X-band EPR spectra of 4 SiC samples with different Ga-doping concentrations recorded at 77K. The inset in the upper right corner shows the EPR intensity measured for 5.0, 2.5, 1.25 and 0.514 at% Ga per Si. 91

Figure 3.14.: Optical microscopy images of *Ga-1* (a), *Ga-2* (b and e), *Ga-3* (c and f) and *Ga-4* (d and g) recorded with different magnifications. 93

Figure 3.15.: SEM images of *Ga-1* (a), *Ga-2* (b), *Ga-3* (c) and *Ga-4* (d) taken at an acceleration voltage of 10 kV. The insets in the upper right corners show images taken with a larger magnification to obtain a more detailed view of the single grains. 95

Figure 3.16.: SEM image of a drop shaped particle of sample *Ga-4* (left) and EDX spectra recorded from the areas labelled with 1 and 2 (right). 96

Figure 3.17.: X-Ray powder diffraction patterns recorded from the samples *Ga-1* (left) and *Ga-2* (right) shown with the according reference patterns of the identified SiC polytypes 3C (red), 6H (blue) and 4H (purple). 98

Figure 3.18.: X-Ray powder diffraction patterns recorded from the samples *Ga-3* (left) and *Ga-4* (right) and are shown with the according reference patterns of the identified species 3C-SiC (red), 6H-SiC (blue) and Si in fcc configuration (green). 99

Figure 3.19.: XPS Si 2p (left) and C 1s core level spectra (solid lines) deconvoluted in the single components (broken lines) for the four SiC:Ga powder samples with different doping concentrations. 102

Figure 3.20.: Schematic energy level diagram of the materials used for ternary component hybrid solar cells. 104

Figure 3.21.: Semi-logarithmic plots of the I-V characteristics of a representative device of the organic binary reference and the 6 ternary hybrid devices recorded in the dark. 106

Figure 3.22.: Photocurrent characteristics recorded under AM1.5G illumination from the organic reference and the 6 different hybrid devices. For each active layer condition, a representative device was chosen. 107

Figure 3.23.: Summary of the averaged key values V_{OC} (black), J_{SC} (red), FF (blue) and PCE (green) of the devices fabricated with 7 different active layer compositions. 109

Figure 3.24.: Illustration of spatially resolved photocurrent maps of *Ref*, *Al-0.4*, *Al-0.13*, *Ga-0.4* and *Ga-0.13*.The current was normalized to the highest value obtained from each device.110

Figure 3.25: Normalized UV-vis spectra recorded from thin films with 7 different compositions. 122

Figure 3.26: Normalized PL spectra recorded at an excitation wavelength of 512 nm. 113

Figure 3.27: Illustration of the normalized EQE curves derived from the solar cells with 7 different active layer compositions. 115

6 REFERENCES

1. Berzelius, J. J. Untersuchungen über die Flussspathsäure und deren merkwürdigsten Verbindungen. *Ann. Phys. phys. Chem.* **77,** 169–230; 10.1002/andp.18240770603 (1824).
2. Agarwal, A. K. & Saddow, S. E. *Advances in silicon carbide processing and applications* (Artech House, Boston, 2004).
3. Acheson, E. G. Carborundum: Its history, manufacture and uses. *Journal of the Franklin Institute* **136,** 194–203; 10.1016/0016-0032(93)90311-H (1893).
4. Amari, S., Hoppe, P., Zinner, E. & Lewis, R. S. Interstellar SiC with unusual isotopic compositions - Grains from a supernova? *ApJ* **394,** L43; 10.1086/186468 (1992).
5. Schubert, E. F. *Light-Emitting Diodes (3rd Edition)* (2018).
6. Lely, J. A. *Ber. dtsch. Keram. Gesellschaft* **32,** 229 (1955).
7. Tairov, Y.M. & Tsvetkov, V. F. Investigation of growth processes of ingots of silicon carbide single crystals. *Journal of Crystal Growth* **43,** 209–212; 10.1016/0022-0248(78)90169-0 (1978).
8. Kuroda, N., Shibahara, K., Yoo, W. S., Nishino, S. & Matsunami, H. in Extended Abstracts of the 19th Conference of Solid State Devices and Materials. *Business Center for Academic Societies, Tokyo, Japan* **227** (1987).

9. Diaz-Rodriguez, P. & Landin, M. Biomorphic Ceramics for Drug Delivery in Bone Tissue Regeneration. *Current pharmaceutical design* **23,** 3507–3514; 10.2174/1381612823666170516145309 (2017).

10. Alexandru, M. *et al.* SiC Integrated Circuit Control Electronics for High-Temperature Operation. *IEEE Trans. Ind. Electron.* **62,** 3182–3191; 10.1109/TIE.2014.2379212 (2015).

11. TRIGUNAYAT, G. A survey of the phenomenon of polytypism in crystals. *Solid State Ionics* **48,** 3–70; 10.1016/0167-2738(91)90200-U (1991).

12. Cheung, R. *Silicon carbide micro electromechanical systems for harsh environments* (Imperial College Press, London, 2006).

13. Bechstedt, F. *et al.* Polytypism and Properties of Silicon Carbide. *phys. stat. sol. (b)* **202,** 35–62; 10.1002/1521-3951(199707)202:1<35::AID-PSSB35>3.0.CO;2-8 (1997).

14. Ching, W. Y., Xu, Y.-N., Rulis, P. & Ouyang, L. The electronic structure and spectroscopic properties of 3C, 2H, 4H, 6H, 15R and 21R polymorphs of SiC. *Materials Science and Engineering: A* **422,** 147–156; 10.1016/j.msea.2006.01.007 (2006).

15. Fan, J. & Chu, P. K. in *Silicon Carbide Nanostructures,* edited by J. Fan & P. K. Chu (Springer International Publishing, Cham, 2014), pp. 7–114.

16. Kimoto, T. & Cooper, J. A. *Fundamentals of silicon carbide technology. Growth, characterization, devices and applications* (Wiley IEEE; IEEE Xplore, Singapore, Piscataway, New Jersey, 2014).

17. Baumann, H. N. The Relationship of Alpha and Beta Silicon Carbide. *J. Electrochem. Soc.* **99,** 109; 10.1149/1.2779671 (1952).

18. Bechstedt, F. & Belabbes, A. Structure, energetics, and electronic states of III-V compound polytypes. *Journal of physics. Condensed matter : an Institute of Physics journal* **25,** 273201; 10.1088/0953-8984/25/27/273201 (2013).

19. Friedrichs, P., Kimoto, T., Ley, L. & Pensl, G. *Silicon carbide. Volume 1: Growth, defects, and novel applications* (Wiley-VCH, Weinheim, 2010).

20. Walker, D. E. Y. Microstructural studies of fluidized-bed β-silicon carbide. *J Appl Crystallogr* **9,** 470–475; 10.1107/S0021889876011941 (1976).

21. Lee, H. S. *et al.* Hybrid polishing mechanism of single crystal SiC using mixed abrasive slurry (MAS). *CIRP Annals* **59,** 333–336; 10.1016/j.cirp.2010.03.114 (2010).

22. Brennan, J. J. & Prewo, K. M. Silicon carbide fibre reinforced glass-ceramic matrix composites exhibiting high strength and toughness. *J Mater Sci* **17,** 2371–2383; 10.1007/BF00543747 (1982).

23. Rosso, M. *et al.* Covalent attachment of organic monolayers to silicon carbide surfaces. *Langmuir : the ACS journal of surfaces and colloids* **24,** 4007–4012; 10.1021/la704002y (2008).

24. Thomé, T., Capelle, M., Thomé, L., Prenant, T. & Néret, M. Thermal oxidation of sintered silicon carbide used for diesel particulate filter walls. *Journal of Ceramic Science and Technology* **3,** 89–94 (2012).

25. Gupta, G. S., Vasanth Kumar, P., Rudolph, V. R. & Gupta, M. Heat-transfer model for the acheson process. *Metall and Mat Trans A* **32,** 1301–1308; 10.1007/s11661-001-0220-9 (2001).

26. Choyke, W. J., Matsunami, H. & Pensl, G. (eds.). *Silicon carbide. Recent major advances ; with 82 tables* (Springer Berlin, Berlin, 2013).

27. Kanaya, M., Takahashi, J., Fujiwara, Y. & Moritani, A. Controlled sublimation growth of single crystalline 4H-SiC and 6H-SiC and identification of polytypes by x-ray diffraction. *Appl. Phys. Lett.* **58,** 56–58; 10.1063/1.104443 (1991).

28. Barrett, D. L., Seidensticker, R. G., Gaida, W., Hopkins, R. H. & Choyke, W. J. SiC boule growth by sublimation vapor transport. *Journal of Crystal Growth* **109,** 17–23; 10.1016/0022-0248(91)90152-U (1991).

29. Ellison, A. *et al.* High temperature CVD growth of SiC. *Materials Science and Engineering: B* **61-62,** 113–120; 10.1016/S0921-5107(98)00482-6 (1999).

30. Kordina, O. *et al.* Growth of SiC by "Hot-Wall" CVD and HTCVD. *phys. stat. sol. (b)* **202,** 321–334; 10.1002/1521-3951(199707)202:1<321::AID-PSSB321>3.0.CO;2-H (1997).

31. Yoon, J.-Y. *et al.* Enhancement in the rate of the top seeded solution growth of SiC crystals via a roughening of the graphite surface. *Jpn. J. Appl. Phys.* **56,** 65501; 10.7567/JJAP.56.065501 (2017).

32. Elwell, D. Crystal Growth from High Temperature Solutions. *J. Electrochem. Soc.* **123,** 319C; 10.1149/1.2133092 (1976).

33. Daikoku, H. *et al.* Top-Seeded Solution Growth of 4H-SiC Bulk Crystal Using Si-Cr Based Melt. *MSF* **717-720,** 61–64; 10.4028/www.scientific.net/MSF.717-720.61 (2012).

34. Lu, K. Porous and high surface area silicon oxycarbide-based materials—A review. *Materials Science and Engineering: R: Reports* **97,** 23–49; 10.1016/j.mser.2015.09.001 (2015).

35. Harris, G. L. (ed.). *Properties of silicon carbide* (INSPEC the Inst. of Electrical Engineers, London, 1995).

36. Lebedev, A. A. Deep level centers in silicon carbide: A review. *Semiconductors* **33,** 107–130; 10.1134/1.1187657 (1999).

37. Kuwabara, H. & Yamada, S. Free-to-bound transition in β-SiC doped with boron. *phys. stat. sol. (a)* **30,** 739–746; 10.1002/pssa.2210300234 (1975).

38. Kuwabara, H., Yamanaka, K. & Yamada, S. Donor-acceptor pair emission from β-sic doped with gallium. *phys. stat. sol. (a)* **37,** K157-K161; 10.1002/pssa.2210370256 (1976).

39. Ikeda, M., Matsunami, H. & Tanaka, T. Site effect on the impurity levels in 4H , 6H , and 15R SiC. *Phys. Rev. B* **22,** 2842–2854; 10.1103/PhysRevB.22.2842 (1980).

40. Evwaraye, A. O., Smith, S. R., Mitchel, W. C. & Hobgood, H. M. Boron acceptor levels in 6H-SiC bulk samples. *Appl. Phys. Lett.* **71,** 1186–1188; 10.1063/1.119620 (1997).

41. Troffer, T. *et al.* Doping of SiC by Implantation of Boron and Aluminum. *phys. stat. sol. (a)* **162,** 277–298; 10.1002/1521-396X(199707)162:1<277::AID-PSSA277>3.0.CO;2-C (1997).

42. Ebelman, J. J. in *Annales de chimie et de physique* (1846), p. 331.

43. Graham, T. XXXV.—On the properties of silicic acid and other analogous colloidal substances. *Journal of the Chemical Society* **17,** 318–327 (1864).

44. W. Geffcken, E. B. *Deutsches Reichspatent 736 411 ,*

45. ROY, R. Aids in Hydrothermal Experimentation: II, Methods of Making Mixtures for Both "Dry" and "Wet" Phase Equilibrium Studies. *J American Ceramic Society* **39,** 145–146; 10.1111/j.1151-2916.1956.tb14180.x (1956).

46. Bach, H. & Schroeder, H. Kristallstruktur und optische eigenschaften von dünnen organogenen titanoxyd-schichten auf glasunterlagen. *Thin Solid Films* **1,** 255–276; 10.1016/0040-6090(68)90045-X (1968).

47. Dislich, H. Glassy and crystalline systems from gels: Chemical basis and technical application. *Journal of Non-Crystalline Solids* **57,** 371–388; 10.1016/0022-3093(83)90425-8 (1983).

48. Dislich, H. Sol-Gel 1984 → 2004 (?). *Journal of Non-Crystalline Solids* **73,** 599–612; 10.1016/0022-3093(85)90379-5 (1985).

49. Dislich, H. Neue Wege zu Mehrkomponentenoxidgläsern. *Angew. Chem.* **83,** 428–435; 10.1002/ange.19710831203 (1971).

50. Hench, L. L. & West, J. K. The sol-gel process. *Chem. Rev.* **90,** 33–72; 10.1021/cr00099a003 (1990).

51. Brinker, C. J. & Scherer, G. W. *Sol-gel science. The physics and chemistry of sol-gel processing* (Acad. Press, Boston, 2010).

52. Owens, G. J. *et al.* Sol–gel based materials for biomedical applications. *Progress in Materials Science* **77,** 1–79; 10.1016/j.pmatsci.2015.12.001 (2016).

53. Rasaki, S. A., Zhang, B., Anbalgam, K., Thomas, T. & Yang, M. Synthesis and application of nano-structured metal nitrides and carbides: A review. *Progress in Solid State Chemistry* **50,** 1–15; 10.1016/j.progsolidstchem.2018.05.001 (2018).

54. Wang, X. *et al.* Graphene/titanium carbide composites prepared by sol–gel infiltration and spark plasma sintering. *Ceramics International* **42,** 122–131; 10.1016/j.ceramint.2015.08.017 (2016).

55. Li, F., Huang, X. & Zhang, G.-J. in *Recent Applications in Sol-Gel Synthesis,* edited by U. Chandra (InTech2017).

56. Hadian, A. M. & Bigdeloo, J. A. The Effect of Time, Temperature and Composition on Boron Carbide Synthesis by Sol-gel Method. *J. of Materi Eng and Perform* **17,** 44–49; 10.1007/s11665-007-9125-0 (2008).

57. Guglielmi, M., Kickelbick, G. & Martucci, A. (eds.). *Sol-Gel Nanocomposites* (Springer New York, New York, NY, s.l., 2014).

58. Rambo, C. R., Cao, J., Rusina, O. & Sieber, H. Manufacturing of biomorphic (Si, Ti, Zr)-carbide ceramics by sol–gel processing. *Carbon* **43,** 1174–1183; 10.1016/j.carbon.2004.12.009 (2005).

59. Raman, V., Parashar, V. K., Dhakate, S., Bahl, O. P. & Dhawan, U. Synthesis of Silicon Carbide through the Sol-Gel Process from Rayon Fibers. *J American Ceramic Society* **83,** 952–954; 10.1111/j.1151-2916.2000.tb01302.x (2000).

60. Najafi, A., Golestani-Fard, F. & Rezaie, H. R. Improvement of SiC nanopowder synthesis by sol–gel method via TEOS/resin phenolic precursors. *J Sol-Gel Sci Technol* **75,** 255–263; 10.1007/s10971-015-3695-3 (2015).

61. Prentiss, M. *Energy revolution. The physics and the promise of efficient technology* (the Belknap press of Harvard University Press, Cambridge, Massachusetts, London, England, 2015).

62. *CO2 Emissions from Fuel Combustion 2010* (OECD, 2010).

63. Dincer, I. Renewable energy and sustainable development: a crucial review. *Renewable and Sustainable Energy Reviews* **4,** 157–175; 10.1016/S1364-0321(99)00011-8 (2000).

64. Jaccard, M. K. *Sustainable fossil fuels. The unusual suspect in the quest for clean and enduring energy* (Cambridge Univ. Press, Cambridge, 2006).

65. Ellabban, O., Abu-Rub, H. & Blaabjerg, F. Renewable energy resources: Current status, future prospects and their enabling technology. *Renewable and Sustainable Energy Reviews* **39,** 748–764; 10.1016/j.rser.2014.07.113 (2014).

66. Dresselhaus, M. S. & Thomas, I. L. Alternative energy technologies. *Nature* **414,** 332–337; 10.1038/35104599 (2001).

67. NREL. Research Cell Record Efficiency Chart. Available at https://www.nrel.gov/pv/assets/pdfs/pv-efficiencies-07-17-2018.pdf (2018).

68. Yoshikawa, K. *et al.* Silicon heterojunction solar cell with interdigitated back contacts for a photoconversion efficiency over 26%. *Nat. Energy* **2,** 17032; 10.1038/nenergy.2017.32 (2017).

69. Shah, A. Photovoltaic Technology: The Case for Thin-Film Solar Cells. *Science* **285,** 692–698; 10.1126/science.285.5428.692 (1999).

70. Hosoya, M. *et al.* Module Development for Organic Thin-Film Photovoltaics. 3 pages / 28th European Photovoltaic Solar Energy Conference and Exhibition; 2236-2238; 10.4229/28THEUPVSEC2013-3DO.8.6 (2013).

71. Dimroth, F. *et al.* Four-Junction Wafer-Bonded Concentrator Solar Cells. *IEEE J. Photovoltaics* **6,** 343–349; 10.1109/JPHOTOV.2015.2501729 (2016).

72. Balint, R., Cassidy, N. J. & Cartmell, S. H. Conductive polymers: towards a smart biomaterial for tissue engineering. *Acta biomaterialia* **10,** 2341–2353; 10.1016/j.actbio.2014.02.015 (2014).

73. Salaneck, W. R., Friend, R. H. & Brédas, J. L. Electronic structure of conjugated polymers: consequences of electron–lattice coupling. *Physics Reports* **319,** 231–251; 10.1016/S0370-1573(99)00052-6 (1999).

74. Strobl, G. R. *The physics of polymers. Concepts for understanding their structures and behavior.* 3rd ed. (Springer, Berlin, Heidelberg, 2007).

75. Yu, G., Gao, J., Hummelen, J. C., Wudl, F. & Heeger, A. J. Polymer Photovoltaic Cells: Enhanced Efficiencies via a Network of Internal Donor-Acceptor Heterojunctions. *Science* **270,** 1789–1791; 10.1126/science.270.5243.1789 (1995).

76. BUNDGAARD, E. & KREBS, F. Low band gap polymers for organic photovoltaics. *Solar Energy Materials and Solar Cells* **91,** 954–985; 10.1016/j.solmat.2007.01.015 (2007).

77. Günes, S., Neugebauer, H. & Sariciftci, N. S. Conjugated polymer-based organic solar cells. *Chem. Rev.* **107,** 1324–1338; 10.1021/cr050149z (2007).

78. Peet, J. *et al.* Efficiency enhancement in low-bandgap polymer solar cells by processing with alkane dithiols. *Nature materials* **6,** 497–500; 10.1038/nmat1928 (2007).

79. Bao, X. *et al.* Annealing-free P3HT:PCBM-based organic solar cells via two halohydrocarbons additives with similar boiling points. *Materials Science and Engineering: B* **180,** 7–11; 10.1016/j.mseb.2013.10.009 (2014).

80. Kroto, H. W., Heath, J. R., O'Brien, S. C., Curl, R. F. & Smalley, R. E. C60: Buckminsterfullerene. *Nature* **318,** 162–163; 10.1038/318162a0 (1985).

81. Valeur, B. & Berberan-Santos, M. N. *Molecular Fluorescence* (Wiley-VCH Verlag GmbH & Co. KGaA, Weinheim, Germany, 2012).

82. Li, C.-Z., Yip, H.-L. & Jen, A. K.-Y. Functional fullerenes for organic photovoltaics. *J. Mater. Chem.* **22,** 4161; 10.1039/c2jm15126j (2012).

83. Yadav, B. C. & Kumar, R. Structure, properties and applications of fullerenes. *International Journal of Nanotechnology and Applications* **2,** 15–24 (2008).

84. Dang, M. T., Hirsch, L. & Wantz, G. P3HT:PCBM, Best Seller in Polymer Photovoltaic Research. *Adv. Mater.* **23,** 3597–3602; 10.1002/adma.201100792 (2011).

85. Chen, C.-C. *et al.* An efficient triple-junction polymer solar cell having a power conversion efficiency exceeding 11%. *Advanced materials (Deerfield Beach, Fla.)* **26,** 5670–5677; 10.1002/adma.201402072 (2014).

86. Huang, J.-H. *et al.* The investigation of donor-acceptor compatibility in bulk-heterojunction polymer systems. *Appl. Phys. Lett.* **103,** 43304; 10.1063/1.4816056 (2013).

87. Wright, M. & Uddin, A. Organic—inorganic hybrid solar cells: A comparative review. *Solar Energy Materials and Solar Cells* **107,** 87–111; 10.1016/j.solmat.2012.07.006 (2012).

88. Konopka, A. *et al.* Paramagnetic signature of microcrystalline silicon carbide. *IOP Conf. Ser.: Mater. Sci. Eng.* **15,** 12013; 10.1088/1757-899X/15/1/012013 (2010).

89. Goh, C., Scully, S. R. & McGehee, M. D. Effects of molecular interface modification in hybrid organic-inorganic photovoltaic cells. *Journal of Applied Physics* **101,** 114503; 10.1063/1.2737977 (2007).

90. Alivisatos, A. P. Semiconductor Clusters, Nanocrystals, and Quantum Dots. *Science* **271,** 933–937; 10.1126/science.271.5251.933 (1996).

91. Kittel, C. *Introduction to solid state physics.* 8th ed. (Wiley, Hoboken, NJ, 2005).

92. Arici, E. *et al.* Hybrid solar cells based on inorganic nanoclusters and conjugated polymers. *Thin Solid Films* **451-452,** 612–618; 10.1016/j.tsf.2003.11.026 (2004).

93. Chu, C.-W., Shrotriya, V., Li, G. & Yang, Y. Tuning acceptor energy level for efficient charge collection in copper-phthalocyanine-based organic solar cells. *Appl. Phys. Lett.* **88,** 153504; 10.1063/1.2194207 (2006).

94. Kim, J. Y. *et al.* Efficient tandem polymer solar cells fabricated by all-solution processing. *Science* **317,** 222–225; 10.1126/science.1141711 (2007).

95. Helander, M. G., Greiner, M. T., Wang, Z. B., Tang, W. M. & Lu, Z. H. Work function of fluorine doped tin oxide. *Journal of Vacuum Science & Technology A: Vacuum, Surfaces, and Films* **29,** 11019; 10.1116/1.3525641 (2011).

96. Zhang, G. *et al.* Remarkable enhancement of photovoltaic performance of ZnO/CdTe core–shell nanorod array solar cells through interface passivation with a TiO 2 layer. *RSC Adv.* **5,** 71883–71889; 10.1039/C5RA14204K (2015).

97. Luo, S. *et al.* Improved charge separation and transport efficiency in panchromatic-sensitized solar cells with co-sensitization of PbS/CdS/ZnS quantum dots and dye molecules. *RSC Adv.* **6,** 21156–21164; 10.1039/C5RA27514H (2016).

98. Brabec, C. J., Sariciftci, N. S. & Hummelen, J. C. Plastic Solar Cells. *Adv. Funct. Mater.* **11,** 15–26; 10.1002/1616-3028(200102)11:1<15::AID-ADFM15>3.0.CO;2-A (2001).

99. Lee, M. M., Teuscher, J., Miyasaka, T., Murakami, T. N. & Snaith, H. J. Efficient hybrid solar cells based on meso-superstructured organometal halide perovskites. *Science* **338,** 643–647; 10.1126/science.1228604 (2012).

100. Shaheen, S. E. *et al.* 2.5% efficient organic plastic solar cells. *Appl. Phys. Lett.* **78,** 841–843; 10.1063/1.1345834 (2001).

101. Halls, J. J. M. *et al.* Efficient photodiodes from interpenetrating polymer networks. *Nature* **376,** 498–500; 10.1038/376498a0 (1995).

102. Brabec, C. J., Shaheen, S. E., Winder, C., Sariciftci, N. S. & Denk, P. Effect of LiF/metal electrodes on the performance of plastic solar cells. *Appl. Phys. Lett.* **80,** 1288–1290; 10.1063/1.1446988 (2002).

103. Glatthaar, M. *et al.* Organic solar cells using inverted layer sequence. *Thin Solid Films* **491,** 298–300; 10.1016/j.tsf.2005.06.006 (2005).

104. Li, G., Chu, C.-W., Shrotriya, V., Huang, J. & Yang, Y. Efficient inverted polymer solar cells. *Appl. Phys. Lett.* **88,** 253503; 10.1063/1.2212270 (2006).

105. Huynh, W. U., Dittmer, J. J. & Alivisatos, A. P. Hybrid nanorod-polymer solar cells. *Science* **295,** 2425–2427; 10.1126/science.1069156 (2002).

106. Günes, S. & Sariciftci, N. S. Hybrid solar cells. *Inorganica Chimica Acta* **361,** 581–588; 10.1016/j.ica.2007.06.042 (2008).

107. Moliton, A. & Nunzi, J.-M. How to model the behaviour of organic photovoltaic cells. *Polym. Int.* **55,** 583–600; 10.1002/pi.2038 (2006).

108. Ibach, H. & Lüth, H. *Festkörperphysik. Einführung in die Grundlagen ; mit 18 Tafeln und 104 Übungen.* 7th ed. (Springer, Berlin, 2009).

109. Liang, W. Y. Excitons. *Physics Education* **5,** 226 (1970).

110. Pope, M. & Swenberg, C. E. *Electronic processes in organic crystals and polymers* (Oxford University Press New York, 1999).

111. Clarke, T. M., Ballantyne, A. M., Nelson, J., Bradley, D. D. C. & Durrant, J. R. Free Energy Control of Charge Photogeneration in Polythiophene/Fullerene Solar Cells: The Influence of Thermal Annealing on P3HT/PCBM Blends. *Adv. Funct. Mater.* **18,** 4029–4035; 10.1002/adfm.200800727 (2008).

112. Device Schematic and a completed device. Available at https://www.ossila.com/products/oled-ito-substrates (2018).

113. Kilian, U. & Weber, C. (eds.). *Lexikon der Physik Bd. 2* (Spektrum Akademischer Verlag GmbH, Heidelberg, Neckar, 2003).

114. Hawkes, P. W., Lotsch, H. K. V. & Reimer, L. *Scanning Electron Microscopy* (Springer Berlin Heidelberg, Berlin, Heidelberg, 1998).

115. Goldstein, J. I. *et al. Scanning Electron Microscopy and X-ray Microanalysis* (Springer US, Boston, MA, 2003).

116. Williams, D. B. & Carter, C. B. *Transmission Electron Microscopy. A Textbook for Materials Science.* 2nd ed. (Springer US, Boston, MA, 2009).

117. Egerton, R. F. & Malac, M. EELS in the TEM. *Journal of Electron Spectroscopy and Related Phenomena* **143,** 43–50; 10.1016/j.elspec.2003.12.009 (2005).

118. Gerson, F. J. A. Weil, J. R. Bolton J. E. Wertz. Electron paramagnetic resonance: Elementary theory and applications. Wiley-interscience, New York (1994). xxi 568 pages, £66.00/$91.95. ISBN 0-471-57234-9. *Magn. Reson. Chem.* **33,** 80; 10.1002/mrc.1260330114 (1995).

119. Baranov, P. G., Bardeleben, H. J. von, Jelezko, F. & Wrachtrup, J. *Magnetic Resonance of Semiconductors and Their Nanostructures* (Springer Vienna, Vienna, 2017).

120. Lavina, B., Dera, P. & Downs, R. T. Modern X-ray Diffraction Methods in Mineralogy and Geosciences. *Reviews in Mineralogy and Geochemistry* **78,** 1–31; 10.2138/rmg.2014.78.1 (2014).

121. Scott A. Speakman. Basics of X-Ray Powder Diffraction. Available at http://www.fis.unical.it/files/fl178/61731BasicsofXRayPowderDiffraction.pdf.

122. Mittemeijer, E. J. & Welzel, U. *Modern Diffraction Methods* (Wiley-VCH Verlag GmbH & Co. KGaA, Weinheim, Germany, 2012).

123. Baer, D. R. & Thevuthasan, S. in *Handbook of Deposition Technologies for Films and Coatings* (Elsevier2010), pp. 749–864.

124. Gauglitz, G. & Vo-Dinh, T. *Handbook of spectroscopy* (Wiley-VCH, Weinheim, 2005).

125. Deibel, C. & Dyakonov, V. Polymer–fullerene bulk heterojunction solar cells. *Rep. Prog. Phys.* **73,** 96401; 10.1088/0034-4885/73/9/096401 (2010).

126. Moulé, A. J., Chang, L., Thambidurai, C., Vidu, R. & Stroeve, P. Hybrid solar cells: basic principles and the role of ligands. *J. Mater. Chem.* **22,** 2351–2368; 10.1039/c1jm14829j (2012).

127. Mihailetchi, V. D., Blom, P. W. M., Hummelen, J. C. & Rispens, M. T. Cathode dependence of the open-circuit voltage of polymer:fullerene bulk heterojunction solar cells. *Journal of Applied Physics* **94,** 6849–6854; 10.1063/1.1620683 (2003).

128. Ohmori, M. *et al.* Annealing effect in bulk heterojunction organic solar cells utilizing liquid crystalline phthalocyanine. *Jpn. J. Appl. Phys.* **53,** 05FZ02; 10.7567/JJAP.53.05FZ02 (2014).

129. Shrotriya, V. *et al.* Accurate Measurement and Characterization of Organic Solar Cells. *Adv. Funct. Mater.* **16,** 2016–2023; 10.1002/adfm.200600489 (2006).

130. Hu, L. *et al.* Organic optoelectronic interfaces with anomalous transient photocurrent. *J. Mater. Chem. C* **3,** 5122–5135; 10.1039/C5TC00414D (2015).

131. Li, Z. & McNeill, C. R. Transient photocurrent measurements of PCDTBT:PC 70 BM and PCPDTBT:PC 70 BM Solar Cells: Evidence for charge trapping in efficient polymer/fullerene blends. *Journal of Applied Physics* **109,** 74513; 10.1063/1.3573394 (2011).

132. Li, Z., Lakhwani, G., Greenham, N. C. & McNeill, C. R. Voltage-dependent photocurrent transients of PTB7:PC 70 BM solar cells: Experiment and numerical simulation. *Journal of Applied Physics* **114,** 34502; 10.1063/1.4813612 (2013).

133. Krebs, F. C., Søndergaard, R. & Jørgensen, M. Printed metal back electrodes for R2R fabricated polymer solar cells studied using the LBIC technique. *Solar Energy Materials and Solar Cells* **95,** 1348–1353; 10.1016/j.solmat.2010.11.007 (2011).

134. Kilian, U. & Weber, C. (eds.). *Lexikon der Physik Bd. 5* (Spektrum Akademischer Verlag GmbH, Heidelberg, Neckar, 2003).

135. Kilian, U. & Weber, C. (eds.). *Lexikon der Physik Bd. 3* (Spektrum Akademischer Verlag GmbH, Heidelberg, Neckar, 2003).

136. Strobl, G. R. *The Physics of Polymers. Concepts for Understanding Their Structures and Behavior* (Springer, Berlin, Heidelberg, 1997).

137. Shionoya, S. in *Luminescence of Solids,* edited by D. R. Vij (Springer US, Boston, MA, 1998), pp. 95–133.

138. Shinde, K. N., Dhoble, S. J., Swart, H. C. & Park, K. in *Phosphate Phosphors for Solid-State Lighting,* edited by K. N. Shinde, S.J. Dhoble, H.C. Swart & K. Park (Springer Berlin Heidelberg, Berlin, Heidelberg, 2012), pp. 41–59.

139. Laverdant, J. *et al.* Experimental Determination of the Fluorescence Quantum Yield of Semiconductor Nanocrystals. *Materials (Basel, Switzerland)* **4,** 1182–1193; 10.3390/ma4071182 (2011).

140. KIM, Y. *et al. in Materials for Sustainable Energy,* edited by V. Dusastre (Co-Published with Macmillan Publishers Ltd, UK2010), pp. 63–69.

141. Padinger, F., Rittberger, R. S. & Sariciftci, N. S. Effects of Postproduction Treatment on Plastic Solar Cells. *Adv. Funct. Mater.* **13,** 85–88; 10.1002/adfm.200390011 (2003).

142. Li, G. *et al. in Materials for Sustainable Energy,* edited by V. Dusastre (Co-Published with Macmillan Publishers Ltd, UK2010), pp. 80–84.

143. Bhatnagar, M. & Baliga, B. J. Comparison of 6H-SiC, 3C-SiC, and Si for power devices. *IEEE Trans. Electron Devices* **40,** 645–655; 10.1109/16.199372 (1993).

144. Hauff, E. von, Dyakonov, V. & Parisi, J. Study of field effect mobility in PCBM films and P3HT:PCBM blends. *Solar Energy Materials and Solar Cells* **87,** 149–156; 10.1016/j.solmat.2004.06.014 (2005).

145. Greulich-Weber, S. & Friedel, B. Bottom-Up Routes to Porous Silicon Carbide. *MSF* **615-617,** 637–640; 10.4028/www.scientific.net/MSF.615-617.637 (2009).

146. Troshin, P. A. *et al.* Material Solubility-Photovoltaic Performance Relationship in the Design of Novel Fullerene Derivatives for Bulk Heterojunction Solar Cells. *Adv. Funct. Mater.* **19,** 779–788; 10.1002/adfm.200801189 (2009).

147. Chen, D., Nakahara, A., Wei, D., Nordlund, D. & Russell, T. P. P3HT/PCBM bulk heterojunction organic photovoltaics: correlating efficiency and morphology. *Nano letters* **11,** 561–567; 10.1021/nl103482n (2011).

148. Müllerová, J., Kaiser, M., Nádaždy, V., Šiffalovič, P. & Majková, E. Optical absorption study of P3HT:PCBM blend photo-oxidation for bulk heterojunction solar cells. *Solar Energy* **134,** 294–301; 10.1016/j.solener.2016.05.009 (2016).

149. Tae Song, J. *et al.* Improved visible light driven photoelectrochemical properties of 3C-SiC semiconductor with Pt nanoparticles for hydrogen generation. *Appl. Phys. Lett.* **103,** 213901; 10.1063/1.4832333 (2013).

150. Li, Y., Chen, C., Li, J.-T., Yang, Y. & Lin, Z.-M. Surface charges and optical characteristic of colloidal cubic SiC nanocrystals. *Nanoscale research letters* **6,** 454; 10.1186/1556-276X-6-454 (2011).

151. Chirvase, D., Parisi, J., Hummelen, J. C. & Dyakonov, V. Influence of nanomorphology on the photovoltaic action of polymer–fullerene composites. *Nanotechnology* **15,** 1317–1323; 10.1088/0957-4484/15/9/035 (2004).

152. Janssen, G. *et al.* Optimization of morphology of P3HT/PCBM films for organic solar cells: effects of thermal treatments and spin coating solvents. *Eur. Phys. J. Appl. Phys.* **37,** 287–290; 10.1051/epjap:2007002 (2007).

153. Kettner, O., Finlayson, C. E. & Friedel, B. The Potential of P3HT:3C-SiC Composite Structures for Hybrid Photovoltaics. *Nanosci Nanotechnol Lett* **7,** 56–61; 10.1166/nnl.2015.1928 (2015).

154. KIM, Y. & Bradley, D. D.C. Bright red emission from single layer polymer light-emitting devices based on blends of regioregular P3HT and F8BT. *Current Applied Physics* **5,** 222–226; 10.1016/j.cap.2003.11.090 (2005).

155. Tress, W., Corvers, S., Leo, K. & Riede, M. Investigation of Driving Forces for Charge Extraction in Organic Solar Cells: Transient Photocurrent Measurements on Solar Cells Showing S-Shaped Current-Voltage Characteristics. *Adv. Energy Mater.* **3,** 873–880; 10.1002/aenm.201200931 (2013).

156. Gao, F. *et al.* Trap-induced losses in hybrid photovoltaics. *ACS nano* **8,** 3213–3221; 10.1021/nn501185h (2014).

157. Li, Z., Gao, F., Greenham, N. C. & McNeill, C. R. Comparison of the Operation of Polymer/Fullerene, Polymer/Polymer, and Polymer/Nanocrystal Solar Cells: A Transient Photocurrent and Photovoltage Study. *Adv. Funct. Mater.* **21,** 1419–1431; 10.1002/adfm.201002154 (2011).

158. Henkel, T. *et al.* Scandium And Gallium Implantation Doping Of Silicon Carbide. *MRS Proc.* **512,** 153; 10.1557/PROC-512-163 (1998).

159. Vodakov, Y. A. *et al.* Silicon carbide doped with gallium. *phys. stat. sol. (a)* **35,** 37–42; 10.1002/pssa.2210350103 (1976).

160. Suzuki, A. Photoluminescence Due to Al, Ga, and B Acceptors in 4H-, 6H-, and 3C-SiC Grown from a Si Melt. *J. Electrochem. Soc.* **124,** 241; 10.1149/1.2133274 (1977).

161. Baranov, P. G., Ilyin, I. V. & Mokhov, E. N. Electron paramagnetic resonance of the group-III deep acceptor impurities in SiC. *Solid State Communications* **100,** 371–376; 10.1016/0038-1098(96)00425-5 (1996).

162. Ammerlaan, C. A. J. & Pajot, B. (eds.). *7th International Conference on Shallow-Level Centers in Semiconductors, Amsterdam, the Netherlands, 17-19 July 1996* (WORLD SCIENTIFIC, Singapore, 1997).

163. Itoh, H. *et al.* Intrinsic Defects in Cubic Silicon Carbide. *phys. stat. sol. (a)* **162,** 173–198; 10.1002/1521-396X(199707)162:1<173::AID-PSSA173>3.0.CO;2-W (1997).

164. Greulich-Weber, S. EPR and ENDOR Investigations of Shallow Impurities in SiC Polytypes. *phys. stat. sol. (a)* **162,** 95–151; 10.1002/1521-396X(199707)162:1<95::AID-PSSA95>3.0.CO;2-X (1997).

165. Latha, H.K.E., Udayakumar, A. & Prasad, V. S. Microstructure and electrical properties of nitrogen doped 3C–SiC thin films deposited using methyltrichlorosilane. *Materials Science in Semiconductor Processing* **29,** 117–123; 10.1016/j.mssp.2013.12.017 (2015).

166. Shaffer, P. T. B. A review of the structure of silicon carbide. *Acta Crystallogr B Struct Sci* **25,** 477–488; 10.1107/S0567740869002457 (1969).

167. Hijikata, Y., Yaguchi, H., Yoshikawa, M. & Yoshida, S. Composition analysis of SiO2/SiC interfaces by electron spectroscopic measurements using slope-shaped oxide films. *Applied Surface Science* **184,** 161–166; 10.1016/S0169-4332(01)00491-3 (2001).

168. Parrill, T.M. & Chung, Y.W. Surface analysis of cubic silicon carbide (001). *Surface Science* **243,** 96–112; 10.1016/0039-6028(91)90348-V (1991).

169. Pawbake, A. *et al.* Growth of boron doped hydrogenated nanocrystalline cubic silicon carbide (3C-SiC) films by Hot Wire-CVD. *Materials Research Bulletin* **76,** 205–215; 10.1016/j.materresbull.2015.12.012 (2016).

170. Mizokawa, Y., Geib, K. M. & Wilmsen, C. W. Characterization of β-SiC surfaces and the Au/SiC interface. *Journal of Vacuum Science & Technology A: Vacuum, Surfaces, and Films* **4,** 1696–1700; 10.1116/1.573958 (1986).

171. Shimoda, K., Park, J.-S., Hinoki, T. & Kohyama, A. Influence of surface structure of SiC nano-sized powder analyzed by X-ray photoelectron spectroscopy on basic powder characteristics. *Applied Surface Science* **253,** 9450–9456; 10.1016/j.apsusc.2007.06.023 (2007).

172. Önneby, C. & Pantano, C. G. Silicon oxycarbide formation on SiC surfaces and at the SiC/SiO2 interface. *Journal of Vacuum Science & Technology A: Vacuum, Surfaces, and Films* **15,** 1597–1602; 10.1116/1.580951 (1997).

173. Gallis, S. *et al.* Photoluminescence in erbium doped amorphous silicon oxycarbide thin films. *Appl. Phys. Lett.* **87,** 91901; 10.1063/1.2032600 (2005).

174. Alfonsetti, R., Lozzi, L., Passacantando, M., Picozzi, P. & Santucci, S. XPS studies on SiOx thin films. *Applied Surface Science* **70-71,** 222–225; 10.1016/0169-4332(93)90431-A (1993).

175. Contarini, S., Howlett, S. P., Rizzo, C. & Angelis, B. A. de. XPS study on the dispersion of carbon additives in silicon carbide powders. *Applied Surface Science* **51,** 177–183; 10.1016/0169-4332(91)90400-E (1991).

176. Binner, J. & Zhang, Y. Characterization of silicon carbide and silicon powders by XPS and zeta potential measurement. *Journal of Materials Science Letters* **20,** 123–126; 10.1023/A:1006734100499 (2001).

177. Xie, Y. & Sherwood, P. M. A. Ultrahigh Purity Graphite Electrode by Core Level and Valence Band XPS. *Surface Science Spectra* **1,** 367–372; 10.1116/1.1247634 (1992).

178. Dong, Y. *et al.* Carbon-Based Dots Co-doped with Nitrogen and Sulfur for High Quantum Yield and Excitation-Independent Emission. *Angew. Chem.* **125,** 7954–7958; 10.1002/ange.201301114 (2013).

179. Rupprechter, G., Kaichev, V. V., Unterhalt, H., Morkel, M. & Bukhtiyarov, V. I. CO dissociation and CO hydrogenation on smooth and ion-bombarded Pd(111): SFG and XPS spectroscopy at mbar pressures. *Applied Surface Science* **235,** 26–31; 10.1016/j.apsusc.2004.05.120 (2004).

180. Kelemen, S. R. & Freund, H. XPS characterization of glassy-carbon surfaces oxidized by O2, CO2, and HNO3. *Energy Fuels* **2,** 111–118; 10.1021/ef00008a001 (1988).

181. Madsen, I. C., Scarlett, N. V. Y., Cranswick, L. M. D. & Lwin, T. Outcomes of the International Union of Crystallography Commission on Powder Diffraction Round Robin on Quantitative Phase Analysis: samples 1 a to 1 h. *J Appl Crystallogr* **34,** 409–426; 10.1107/S0021889801007476 (2001).

182. Li, Z. *et al.* A low-work-function, high-conductivity PEDOT:PSS electrode for organic solar cells with a simple structure. *Synthetic Metals* **210,** 363–366; 10.1016/j.synthmet.2015.11.006 (2015).

183. Wetzelaer, G. A. H., Kuik, M., Lenes, M. & Blom, P. W. M. Origin of the dark-current ideality factor in polymer:fullerene bulk heterojunction solar cells. *Appl. Phys. Lett.* **99,** 153506; 10.1063/1.3651752 (2011).

184. Friedel, B., McNeill, C. R. & Greenham, N. C. Influence of Alkyl Side-Chain Length on the Performance of Poly(3-alkylthiophene)/Polyfluorene All-Polymer Solar Cells. *Chem. Mater.* **22,** 3389–3398; 10.1021/cm100189t (2010).

185. Beljonne, D. & Cornil, J. (eds.). *Multiscale modelling of organic and hybrid photovoltaics* (Springer Berlin Heidelberg, Berlin, Heidelberg, 2014).

186. Manceau, M. *et al.* Effects of long-term UV–visible light irradiation in the absence of oxygen on P3HT and P3HT:PCBM blend. *Solar Energy Materials and Solar Cells* **94,** 1572–1577; 10.1016/j.solmat.2010.03.012 (2010).

187. Freitas, F. S., Souza e Silva, J. M. de, Cardoso, M. B. & Nogueira, A. F. Incorporation of nanocrystals with different dimensionalities in hybrid TiO 2 / P 3 HT solar cells. *J. Photon. Energy* **5,** 57407; 10.1117/1.JPE.5.057407 (2015).

188. Akimov, Y. A., Koh, W. S., Sian, S. Y. & Ren, S. Nanoparticle-enhanced thin film solar cells: Metallic or dielectric nanoparticles? *Appl. Phys. Lett.* **96,** 73111; 10.1063/1.3315942 (2010).

189. Sundberg, M., Inganäs, O., Stafström, S., Gustafsson, G. & Sjögren, B. Optical absorption of poly(3-alkylthiophenes) at low temperatures. *Solid State Communications* **71,** 435–439; 10.1016/0038-1098(89)90087-2 (1989).

190. Li, G. *et al.* High-efficiency solution processable polymer photovoltaic cells by self-organization of polymer blends. *Nature Mater* **4,** 864–868; 10.1038/nmat1500 (2005).

191. Lefrançois, A. *et al.* Enhanced charge separation in ternary P3HT/PCBM/CuInS2 nanocrystals hybrid solar cells. *Scientific reports* **5,** 7768; 10.1038/srep07768 (2015).

192. Kim, C.-H. *et al.* Silver nanowire embedded in P3HT:PCBM for high-efficiency hybrid photovoltaic device applications. *ACS nano* **5,** 3319–3325; 10.1021/nn200469d (2011).